Metallophthalocyanine-gold nanoparticle conjugates for Photodynamic Antimicrobial Chemotherapy

A thesis submitted in fulfilment of the requirements for the degree of

DOCTOR OF PHILOSOPHY

Of

Rhodes University

By

Thandekile Phakamisiwe Mthethwa

December 2014

Dedication

I wish to dedicate this thesis to my late brother

Sibusiso Bhekisisa Qhawe Mthethwa

"In our hearts you hold a special place no one else can fill''

ACKNOWLEDGEMENTS

*Work hard and become a leader; Be lazy and become a slave (**Proverbs 12:24**)*

First I must thank my supervisor, Distinguished Professor Tebello Nyokong for the opportunity of working with her and the international opportunities she afforded to me. Her commitment in supporting and shaping my ideas throughout this project is greatly appreciated. I would also like to thank her for her commitment in reading my thesis.

Thanks to Dr. Edith Antunes for sharing a lot of scientific ideas with me and for always ready to help. She taught me to have fun with my experiments.

I would like to also thank the following; Professor Martin Stillman and his group from The University of Western Ontario. For everything they taught me about protein synthesis and ESI-MS spectrometry. The late Proffessor Chen and his group from Fudan University, China, for teaching me cell work and confocal microscopy. Ahmed Eldud from the department of statistics, Rhodes University for helping with statistical analysis.

Special thanks to my loving family, for constant love and support especially at times when it was most needed. I would not have made it alone without each one of you. I am especially greatful to my mother for her amazing love and encouragement to persue my dreams.

Acknowledgements

Thanks to Rhodes University chemistry department for the opportunity to do my studies. Thanks must also be given to my friends for the good times.

I would like to thank the NRF innovation scholarship for funding my studies.

Lastly but not least I want to give praise to the Almighty God who made it all possible.

ABSTRACT

This thesis presents the synthesis of neutral and cationic metallophthalocyanines and their gold nanoparticles conjugates. The spectroscopic characterization of these compounds is presented herein. The studies presented in this work shows that the conjugation of gold nanoparticles influenced both photophysical and photochemical properties.

Gold nanoparticles were found to enhance the singlet oxygen quantum yield while lowering the fluorescence quantum yields. This work also looks at the effect of anisotropic gold nanoparticles such as nanorods and bipyramids on the photophysical behaviour of the metallophthalocyanines. The effect of the size of the gold nanorods was investigated herein. The results show that photophysical and photochemical properties can be influenced by both size and shape of the nanoparticles. Physical characterization about the loading of nanoparticles was also looked into. Parameters such as the surface area, the number of surface atoms, the number of atoms as well as the number of nanoparticles loaded on the surface of the phthalocyanines were studied. The self-assembled monolayers formed by phthalocyanines on gold surfaces were studied using the X-ray photoelectron spectroscopy (XPS).

The gold nanoparticles synthesized herein include both organic and water soluble, different capping agents (citrate, tetraammonium bromide (TAOBr) and cetrimethylammonium bromide (CTAB). The concentration of the gold

nanoparticles was measured on the inductively coupled plasma (ICP) and their size and shape were obtained from the transmission electron microscopy (TEM) images.

A cationic aluminium phthalocyanine and its conjugates were used for photoinactivation of bacteria and fungi. The results show significant reduction and higher activity in the presence of gold nanoparticles, especially nanorods.

A small chapter in this work presents an attempted work on the binding of metallothionein protein with protophorphyrin (IX). The pH and concentration dependent binding studies were investigated.

Table of Contents

LIST OF ABBREVIATIONS

A. A. = Ascorbic acid

Abs = Absorbance

AuNP = Gold nanoparticles

BPs = Bipyramids

C. albicans = *Candida albicans*

CT = Charge transfer

CTAB = Cetyltrimethylammonium bromide

DBU = 1,8-Diazabicyclo[5.4.0]undec-7-ene

DMAE = Dimethylaminoethanol

DMF = Dimethylformamide

DMSO = Dimethlsulfoxide

BPBF = Diphenylisobenzofuran

ε = Molar extinction coeffient

E. Coli = *Escherichia coli*

EDX = Energy dispersive X-ray

ESI-Mass = Electrospray ionization mass

F = Fluorescence

FePPIX = Iron protophorphyrin IX

FT-IR = Fourier transform-infrared

HOMO = Highest occupied molecular orbital

IC = Internal conversion

ICP OES = inductively coupled plasma with an optical Emission spectroscopy detector

In vitro = in an aqueous environment in a test tube

ISC = Intersystem crossing

LUMO = Lowest unoccupied molecular orbital

m/z = Mass to charge ratio

MCD = Magnetic circular dichroism

NIR = Near infra-red

MPc = Metallophthalocyanine

MT = Metallothionein

NMR = Nuclear magnetic resonance

NP = Nanoparticles

NRs = Nanorods

NR = Non-radiative

PACT = Photodynamic antimicrobial chemotherapy

Pc = Phthalocyanine

PDT = Photodynamic therapy

PL = Photoluminescence

PMT = Photomultiplier tube

P = Phosphorescence

PBS = Phosphate buffer solution

PS = Photosensitizer

PTT = Photothermal therapy

SPR = Surface plasmon resonance

TEM = Transmission electron microscopy

TCSPC = Time correlated single photon counting

TAOBr = Tetraoctyammonium bromide

TX 100 = Triton X 100

UV-Vis = Ultraviolet-visible

XRD = X-ray diffraction

XPS = X-ray photoelectron spectroscopy

VR = Vibrational relaxation

LIST OF SYMBOLS

ΔA = Change in absorbance

α = Non-peripheral position

β = Peripheral position

ε_s = Singlet state molar exctinction

ε_T = Triplet state molar exctinction

hv = Light

M = Concentration in molarity

^{1}MPc* = Metallophthalocyanines in the excited triplet state

^{1}MPc* = Metallophthalocyanines in the excited singlet state

n = Refractive indeces of solvent

N_A = Avogadro's number

S_0 = Ground singlet state

S_1 = Excited singlet state

SA = Surface area

Φ_F = fluorescence quantum yield

Φ_T = Triplet quantum yield

Φ_{Δ} = Singlet oxygen quantum yield

$^1O_2$ = Singlet oxygen

$^3O_2$ = Ground state oxygen

τ_0 = Radiative lifetime

τ_F = Fluorescence lifetime

τ_T = Triplet state lifetime

T_1 = First excited triplet state

µL = Microliter

λ = Wavelength

LIST OF FIGURES

LIST OF SCHEMES

LIST OF TABLES

Chapter 1
Introduction

This thesis combines phthalocyanine molecules with different shapes of gold nanoparticles. The effect of the nanoparticles on the photophysical properties and biological activity of phthalocyanines is explored.

1.1. Gold nanoparticles

Nanoparticles can be defined as particles with a size range between 1- 100 nm **[1]**. They have a high surface to volume ratio with a large fraction of their atoms being on the surface. The properties of the nano-scale materials are affected by their size and shape. Nanoparticles can be synthesized by either top-down or bottom up approaches **[2]**. The top-down approach is physical, and it is difficult to achieve monodispersed nanoparticles using this method. Whereas, the bottom-up approach is a chemical method and it is easy to control size and shape using this method **[2],** and is employed in this thesis.

Colloidal gold dates back to the 5th century B.C. where it was used as a colourant to ceramic and ruby glass **[3]**. The first colloidal sample of gold was discovered in 1857 by Machael Faraday who realized that its colour was due to the size of the gold particles **[4]**. In 1951, Turkevich *et al* **[5]** used the electron microscope to study the structural properties of gold nanoparticles. To date a large number studies have been undertaken in order to understand the optical and electronic properties of gold nanoparticles leading to wide range of applications **[6-8]**.

1.1.1. Optical properties

Gold nanoparticles exhibit colours that differ from the bulk. These colours are due to a strong absorption in the visible to near infrared known as surface plasmon resonance (SPR) **[9]**. The SPR is a result of the oscillating surface electrons in metal nanoparticles which is induced by the electric field (**Figure 1.1**). The SPR peak position and intensity depend on the particle size and shape. Increasing the size of the gold nanoparticles causes a red shift of the SPR band.

For example the optical behaviour of gold nanorods differ from nanospheres because the properties of the former are defined by both length and width. Gold nanorods usually show two absorption bands that are induced by the oscillation along the length (longitudinal peak) and along the width (transverse peak) of the rods (**Figure 1.2(B)**). The intensity of the longitudinal peak depends on the concentration and aspect ratio of the nanorods **[10]**. Spheres have one SPR peak, **Figure 1.2 (A)**.

The size of the nanorods is estimated using the ratio of the length/width which is known as the aspect ratio. The longitudinal peak of the nanorods can be tuned towards near infrared by increasing the aspect ratio whereas the transverse peak is relatively insensitive **[11]**. Synthesis of gold nanorods with controlled aspect ratio and absorption within the optical window is crucial for biological applications.

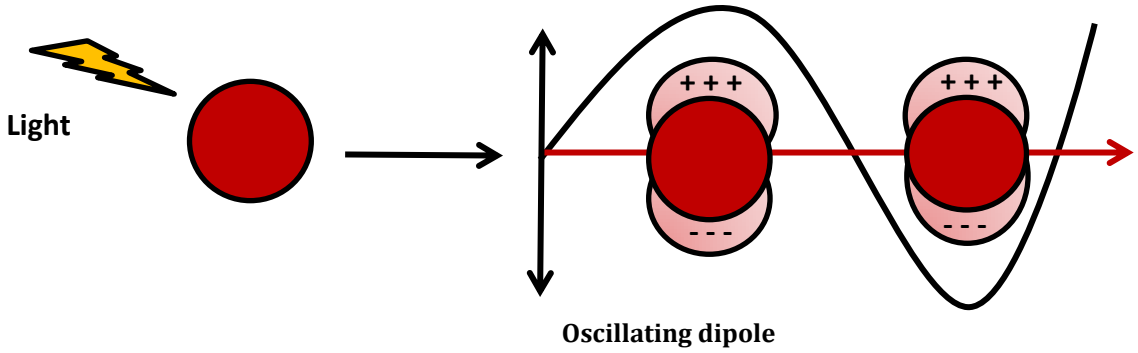

Figure 1.1: Oscillating dipoles induced by magnetic field.

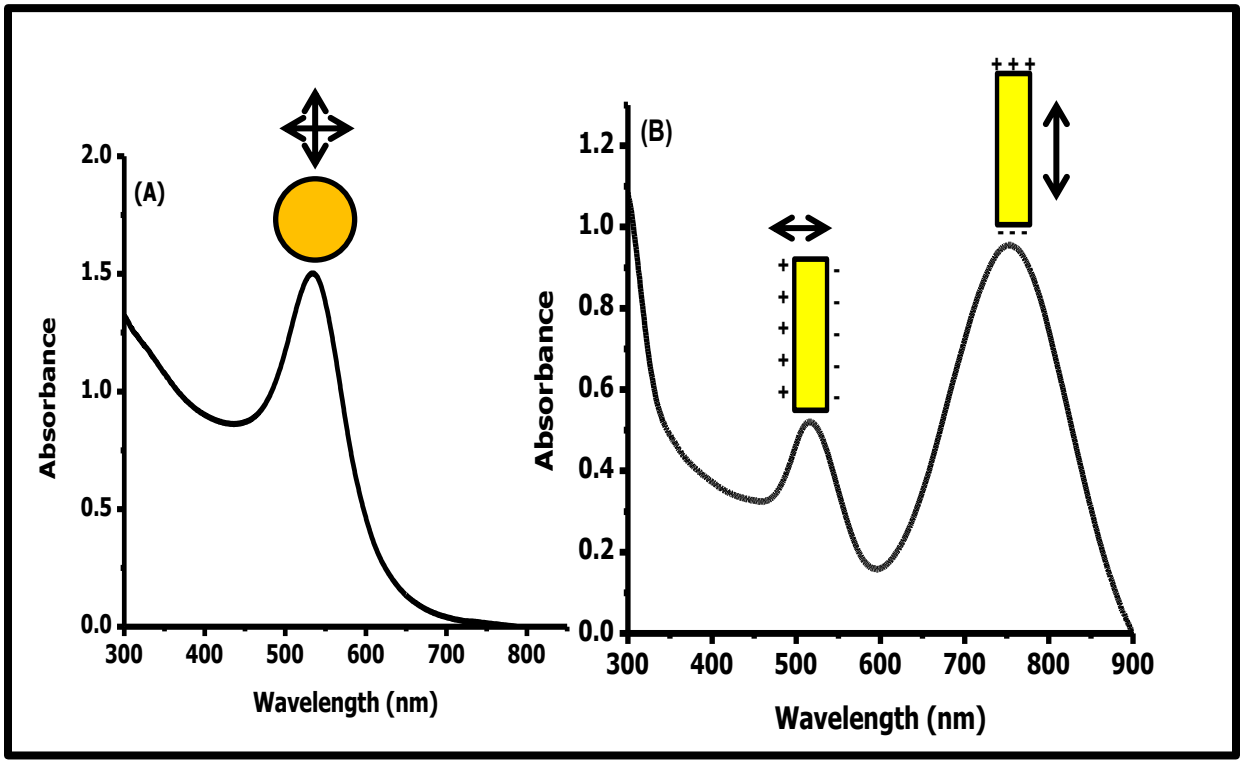

Figure1.2: Typical UV-Vis absorption of gold (A) nanospheres and (B) nanorods showing SPR bands.

In addition to gold nanorods, gold nanoparticles can be obtained in a variety of other shapes such as nanodisks **[12]**, nanoprisms **[13-15]**, nanocages **[16]** and nanostars **[17, 18]** by tuning the reaction conditions.

1.1.2. Synthesis and characterization

Spherical nanoparticles can simply be obtained through the reduction of the gold salt in the presence of a capping agent and a number of synthetic methods have been reported. The Turkevich method is the most popular method for synthesizing spherical gold nanoparticles **[5]**. In this method trisodium citrate is used as both capping agent and reducing agent. The Brust-Schiffrin method was introduced in 1994 for the synthesis of spherical gold nanoparticles in a two phase reaction **[19]**. The water-toluene two phase system is used in this method while using tetraoctylammonium bromide (TOABr) as a phase transfer agent and sodium borohydride ($NaBH_4$) as a reducing agent. The size of these nanoparticles can be tuned by modifying the reaction parameters such as the reactant concentration or reducing agent **[20]**.

The common method to synthesize gold nanorods and other non-spherical gold nanoparticles is a seed mediated method which was first reported in 1989 **[21]**.This is a two-step method in which the first step involves the synthesis of the gold seeds through reduction with $NaBH_4$. The second step is the growth step in which the desired nanoparticles are grown by reduction with ascorbic acid which reduces Au^{3+} to Au^{+}, and then the seed solution is added to complete the reduction of Au^{+} to Au^{0} (**Scheme 1.1**)**[22, 23]**.

There are three factors that play a role in the shape evolution of nanoparticles in a solution; (**i**) surface energy, (**ii**) the phase of the crystalline seed and (**iii**) temperature **[24]**. Selective surfactants can be used to stabilize certain surface energies in order to promote anisotropic growth **[25, 26]**. Cetyltrimethylammonium bromide, bromide (CTAB) is a commonly used surfactant; it can bind preferentially to the growing crystals thus acting as a shape directing surfactant **[27]**.

CTAB has been reported to bind on the {100} facets of the growing gold nanoparticles thus promoting growth on the {111} direction **[28, 29]**. The growth of these nanoparticles also involves other additives like silver nitrate which is hypothesized to preferentially get deposited to specific facets of the growing crystal thus, influencing the shape **[30]**.

The seeds also play a crucial role in shape control synthesis; a rod shape can be obtained from a single-crystalline seed whereas single-twinned seed can yield bipyramids **[31, 32]**. Gold nanoparticles synthesized by the seed mediated method are sensitive to the temperature of the reaction. It has been shown that temperature accelerates the reduction process in the growth of the metal nanoparticles favouring kinetically stable shapes such as prisms and spheres **[33]**.

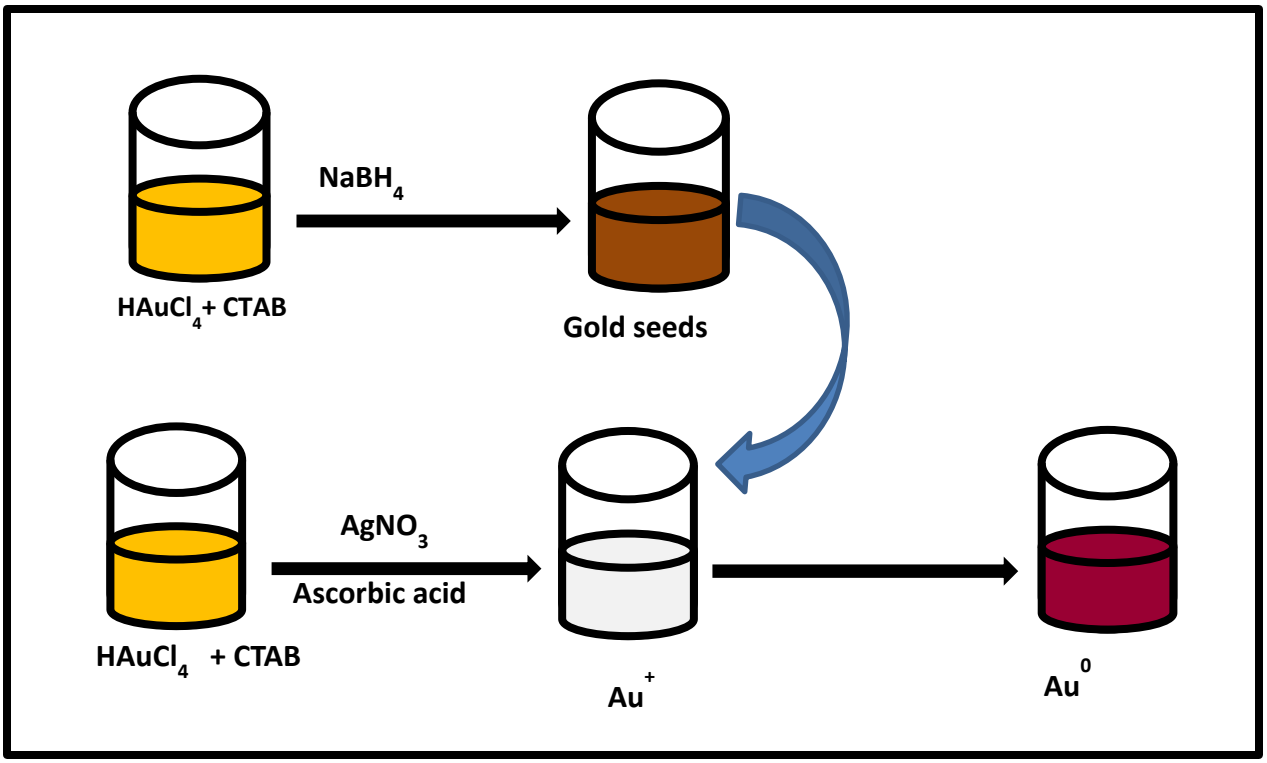

Scheme1.1: Schematic representation of the seed-mediated growth method **[22,23].**

UV-Visible spectroscopy is used for optical analysis of gold nanoparticles. Microscopic characterization such as scanning electron microscope (SEM), transmission electron microscope (TEM), and high resolution transmission electron microscope (HRTEM) are used to obtain information about the morphology and size distribution. X-ray diffraction (XRD) and selective area electron diffraction (SAED) are normally used to analyze the crystallographic structure.

1.2. Phthalocyanines

1.2.1. History and background

Phthalocyanines (Pcs) were first discovered by Braun and Tcherniac in 1907 **[34]** and characterization followed in the 1930's **[35-39]**. Nowadays phthalocyanines have attracted a lot of attention as second generation photosensitizers. Phthalocyanines are aromatic 18-π electron system compounds which are made up of four isoindole units joined together by nitrogen atoms (**Figure 1.3**). The structure can be substituted on the β or α positions to provide new properties such as solubility and biocompatibility **[40]**. Phthalocyanine complexes have been used in a variety of applications due to their chemical stability and interesting photophysical properties. Applications of phthalocyanines can be found in catalysts **[41]**, gas sensors **[42]**, in optical limiting applications **[43]** and in photodynamic therapy **[44]**.

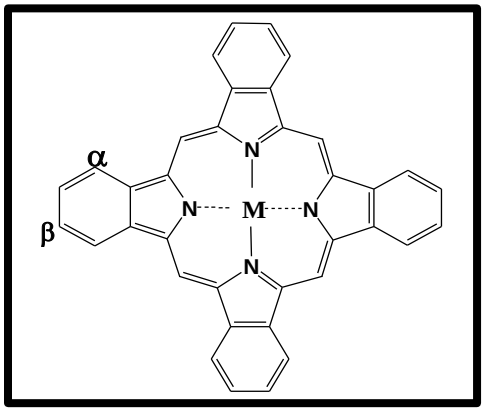

Figure 1.3: Typical structure of metallophthalocyanine showing α and β positions.

1.2.2. Electronic absorption spectra

The conjugated π aromatic system results in strong absorption bands (**B** and **Q** bands) in their UV-visible spectra (**Figure 1.4**) of phthalocyanines **[45]**. The B bands are due to π-π* transitions (**Figure 1.5**) **[46]** due to the transition from the a_{2u} and b_{2u} highest occupied molecular orbital (HOMO) orbitals to the e_g lowest unoccupied molecular orbital (LUMO). The two transitions of the B bands are due the superimposition of B_1 and B_2 bands and usually appear as a broad band **[47-50]**. The Q band is caused by a transition from the a_{1u} (HOMO) orbital to a degenerate e_g (LUMO) orbital. The Q-band is the most intense band in the visible region of the spectrum. Metallated phthalocyanines (MPcs) have a strong single Q-band, whereas in unmetallated Pcs, the Q-band is split as a result of the reduced symmetry (**Figure 1.4**) **[45]**. Metallated phthalocyanines have a D_{4h} symmetry whereas the free base analogues have a D_{2h} symmetry which results in a split of the Q band **[51]**. The phthalocyanine structure is able to accommodate a number of metals (~70) in its structural inner cavity **[52]**.

The large metals such as lead usually cause a red shift of the Q-band **[53]**. Other factors that cause a shift in the Q-band include the nature and position of the ring substituents and the sequential addition of fused rings that causes a deviation from planarity.

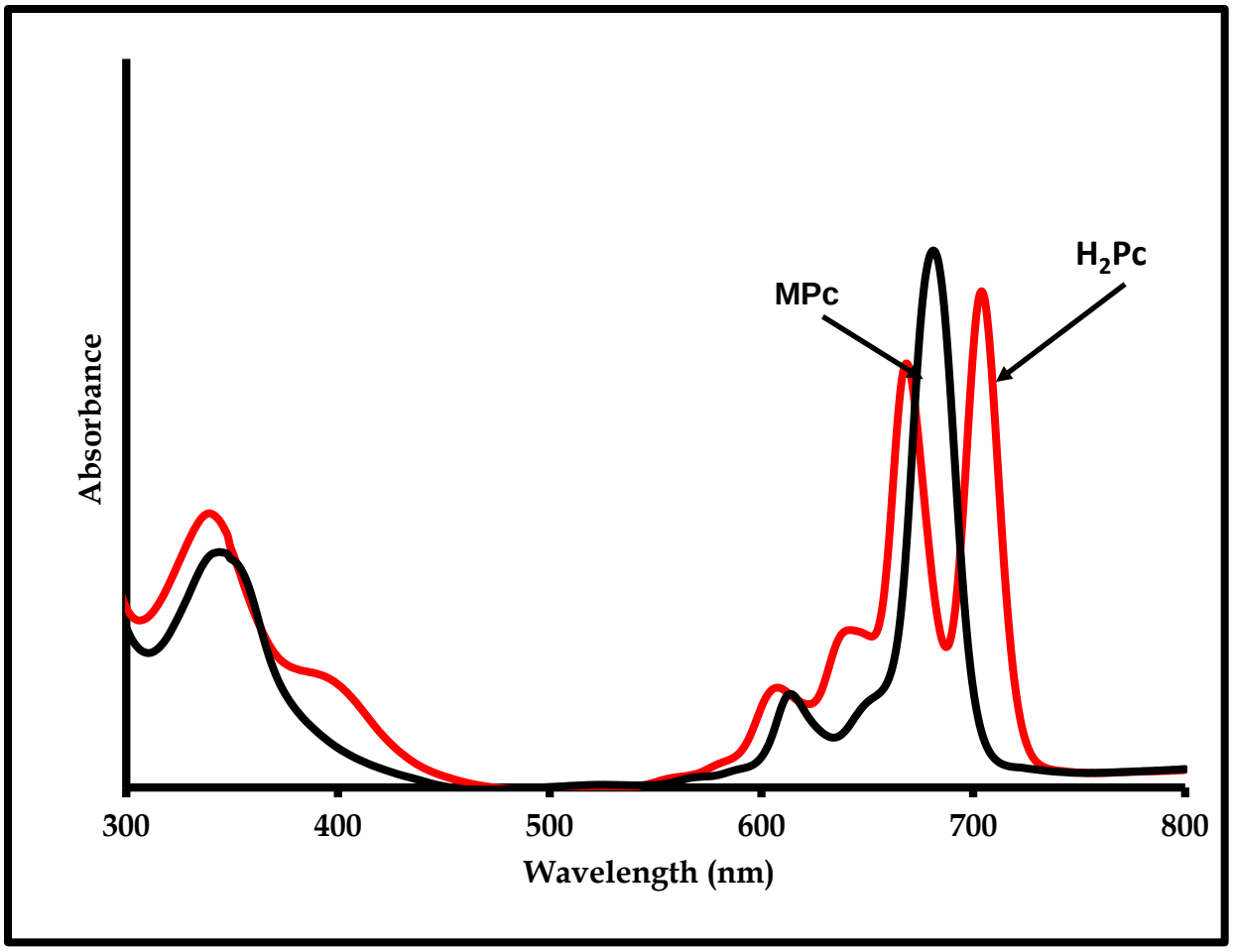

Figure 1.4: Ground state electronic absorption spectra of free base phthalocyanine and metallated phthalocyanine.

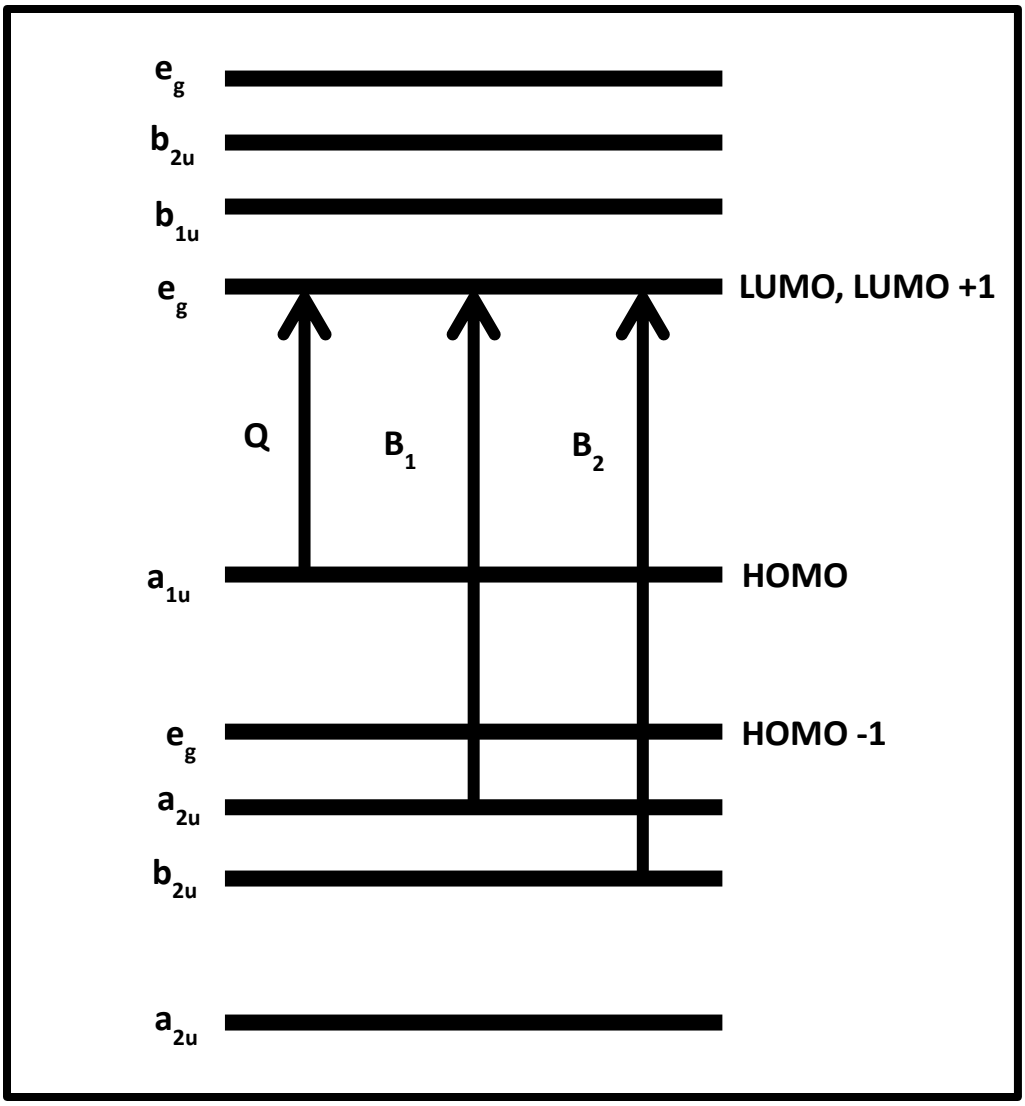

Figure 1.5: Electronic transitions showing origin of the **Q** and the **B** bands of the phthalocyanines **[45]**.

1.2.3. Aggregation

Aggregation is a result of the interactions between the π-systems of the phthalocyanine rings. There are two types of aggregates found in phthalocyanines: (**1**) H-aggregates, which cause a blue shift, and (**2**) J-aggregates, which cause a red shift **[54, 55]**. H-aggregates result when there is a parallel stacking of the monomer units; however the end to end stacking causes J-aggregates. The formation of such aggregates causes a split of the excited state energy level as in **Figure 1.6**.

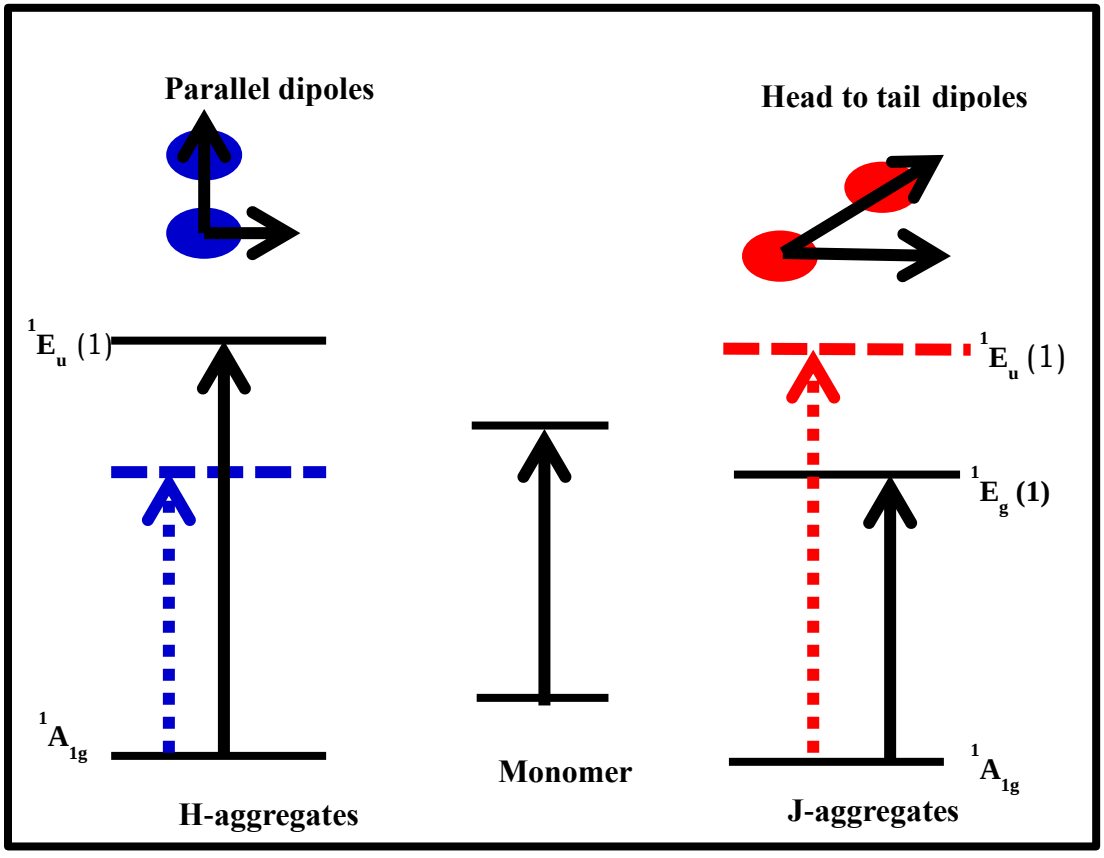

Figure 1.6: Schematic representation of electronic transitions for H-aggregates and J-aggregates based on molecular exciton theory.

Aggregation can be reduced by the presence of axial ligands or bulky substituents. MPcs have been reported to aggregate extensively in aqueous solvents. However, surfactants such as Triton-X and chremophore EL (CEL) can be employed to disaggregate MPcs (**Figure 1.7**) **[56]**.

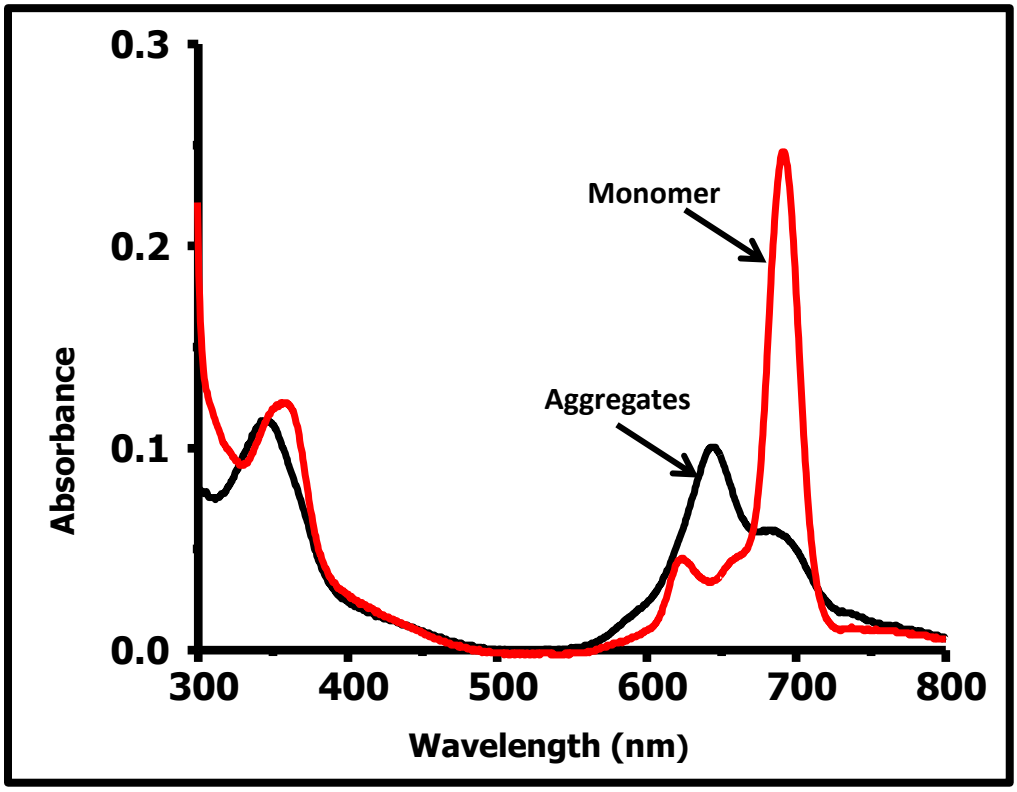

Figure 1.7: Absorption spectra of a typical aggregated phthalocyanine in water (black) and after the addition of Triton X 100 [**unpublished work**].

1.2.4. Phthalocyanine synthesis

Phthalocyanines can be synthesized from a range of precursors such as phthalonitriles, phthalic anhydride, phthalic acid, phthalimide,

o-dibromobenzene and *o*-cyanobenzamide (**Scheme 1.2**). The synthesis is generally a cyclotetramerization reaction of these precursors in the presence of a metal salt and a catalyst as shown in **Scheme 1.2 [57-60]**. Synthesis of metallated phthalocyanines from phthalonitriles involves heating to high temperatures using a high boiling point solvent in the presence of metal salt and a base such as 1,8-diazabicyclo [5.4.0]undec-7-ene (DBU). Substituted phthalocyanines can be prepared from substituted phthalonitriles. The nitro group on the **3** or **4** position of the nitrophthalonitrile is displaced through a nucleophilic reaction in the presence of potassium carbonate. This reaction was first reported by Keller *et al*. **[61]** in 1980. Introduction of substituents gives the phthalocyanine new required properties such as solubility. Water soluble phthalocyanines can be synthesized by substitution of the nitro groups with water soluble substituents. These phthalocyanines are more desirable for biological applications.

Low symmetry phthalocyanines can be obtained from the condensation of two different phthalonitriles **A** and **B** to form the structures with **AAAA, BBBB**, **ABAB, ABBA, ABBB and AAAB**.(**Scheme 1.3**) **[62,63]**. The AAAB type of structure can be obtained by adjusting the ratio of the precursors, followed by chromatographic separation. Symmetrical and unsymmetrical Pcs are reported in this work.

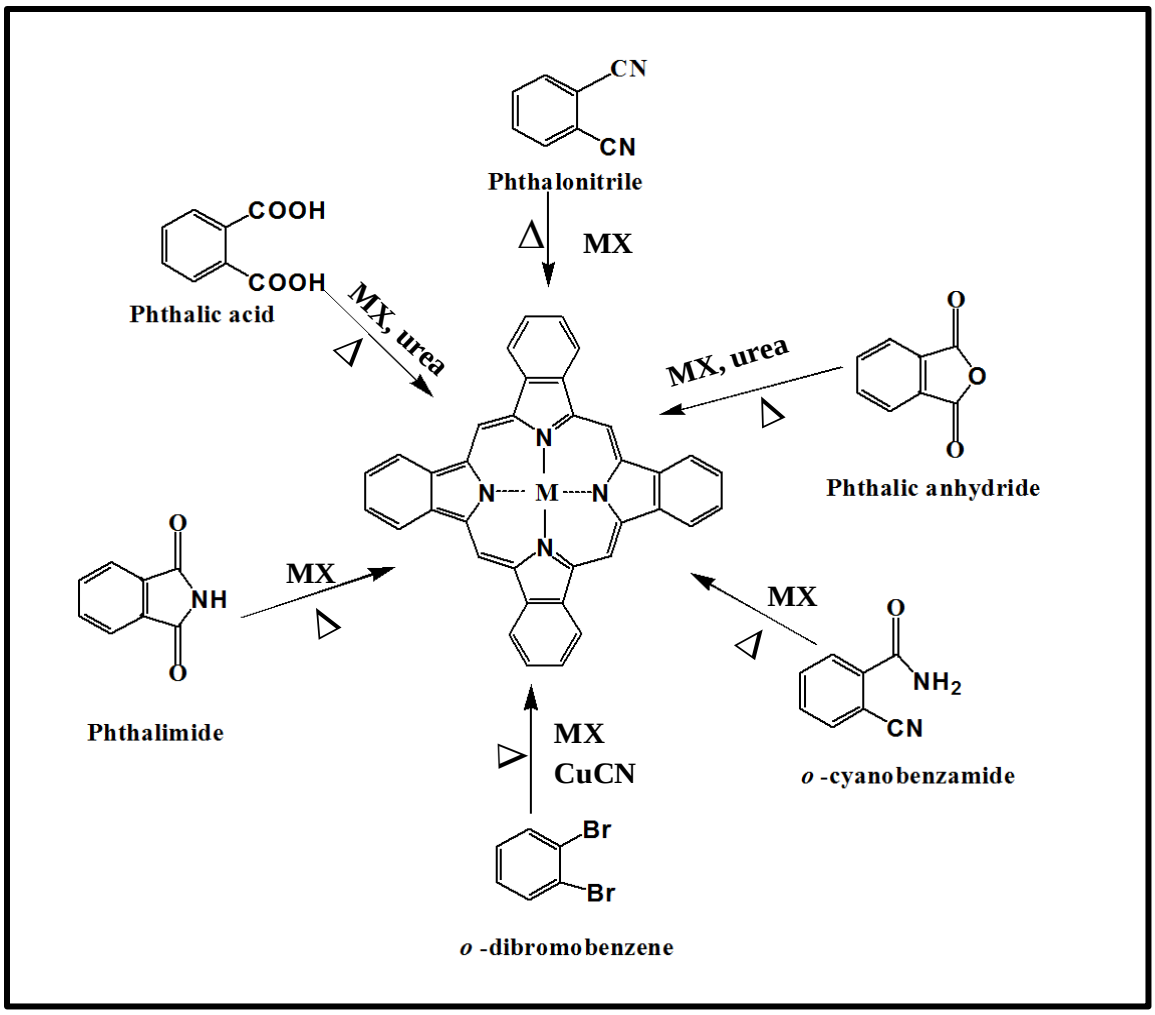

Scheme1.2: Synthesis routes to metallocyanines (MPcs) from various precursors.

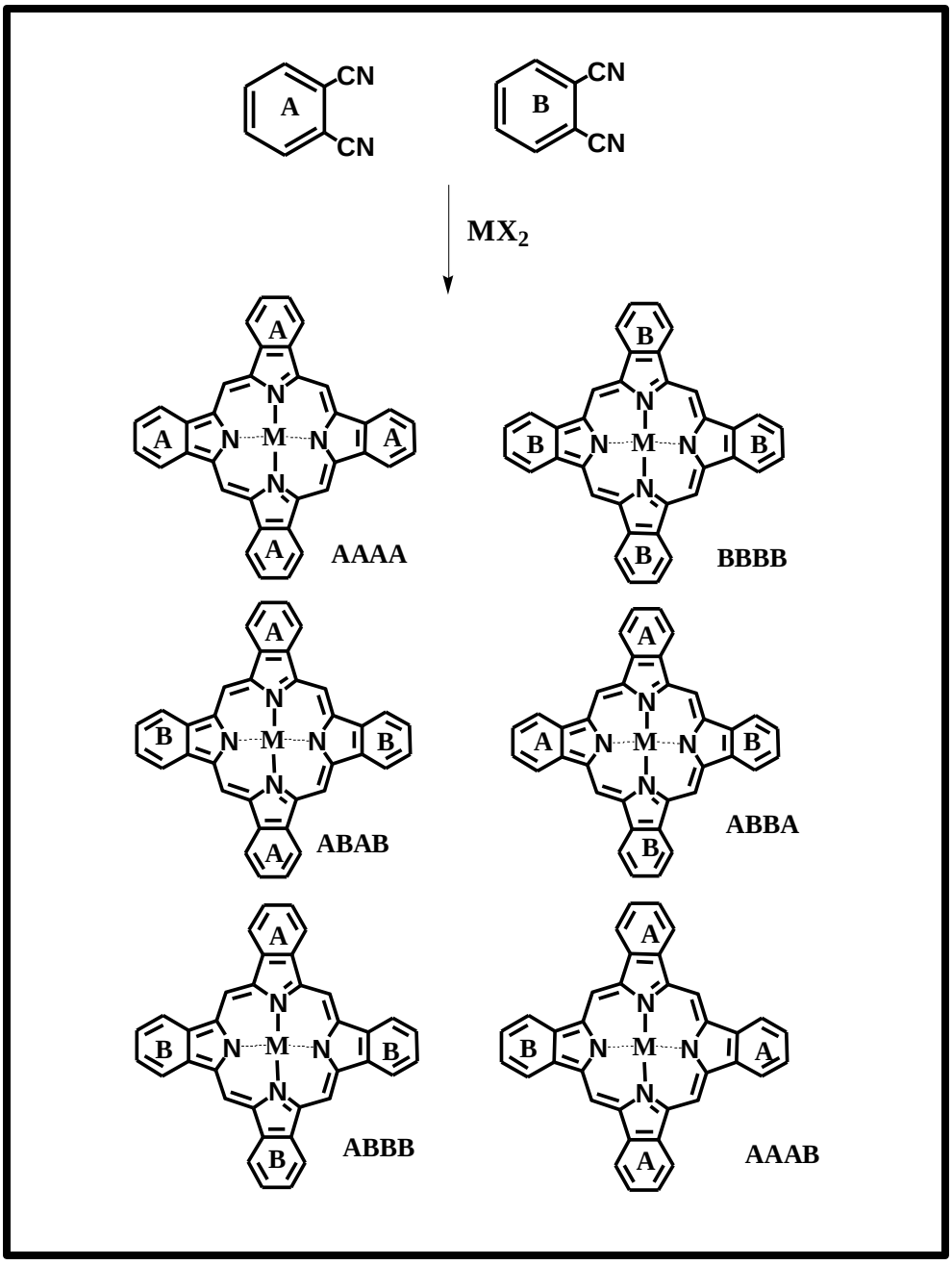

Scheme1.3: The products anticipated for a mixed condensation of two phthalonitriles **A** and **B [62, 63]**.

1.2.5. Phthalocyanine synthesized and studied in this work

Phthalocyanines reported in this work contain **(i)** Al, Mg, and Zn as central metal, **(ii)** alkythio, arylthio and terminal thiol substituents, **(iii)** quarternizable substituents and **(iv)** substitution with thiamine as a biomolecule, **Table1.1**.

Metal centers have been reported to influence the photophysical and photochemical properties of MPcs complexes. Metals with a closed shell such as zinc are known to produce high singlet oxygen quantum yields which is the main cytotoxic species required to inactivate pathogens **[64]**. The use of Al as a central metal is of particular interest since Photosens® (a sulfonated Pc derivative) is already in clinical trials for PDT **[65].** Magnesium is a small metal and does not promote intersystem crossing however; it was studied in this work for comparison.

Syntheses of metallophthalocyanine complexes containing alkylthio or arylthio ring substituents have been explored **[66-69]**. These phthalocyanine complexes show red shifted Q band that makes them good candidates for photodynamic applications. The phthalocyanine complexes in this work are peripherally tetrasubstituted with 4-[2-(dimethylamino) ethanethio] groups, (**1** and **2**). Complexes containing this substituent have been reported before for MPc complexes containing Zn, Ni, Co and Mn as central metals **[70-72]**. However aluminium and magnesium derivatives of these complexes are reported for the first time in this work. Functionalized phthalocyanine complexes containing terminal SH groups have been less studied due to the difficulty of the

synthesis **[73-76]**. These complexes readily form S-S bonds in air. A thiol substituted phthalocyanine complex (**3**) reported in this work has never been reported before. Terminal thiols are of interest because they form stronger bonds with gold nanoparticles. *The synthesis of this complex was done with assistance from our collaborators in Turkey (publication 2).*

The synthesis of water soluble phthalocyanines is desirable in photoinactivation of pathogenic microbes hence, quaternized water soluble phthalocyanines were studied in this work. Functionalization of phthalocyanines with biomolecules also provides biocompatibility and water solubility. A thiamine substituted phthalocyanine (**4**) is reported in this work for the first time. Thiamine is a water soluble vitamin which is usually found in high concentrations in the liver, kidneys, brain and the heart **[77]**.

A summary of the compounds used in this work is provided in **Table 1.1**. The behaviour of these complexes in the presence of gold nanoparticles is investigated in this work.

Table1.1: Phthalocyanines synthesized and studied in this work

Phthalocyanines	No.
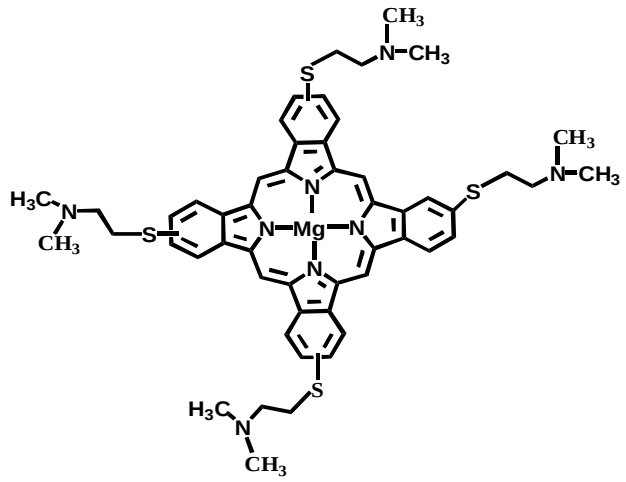 *2, (3)-Tetra-[2-(dimethylamino) ethanethio)phthalocyaninomagnesium (II)*	1
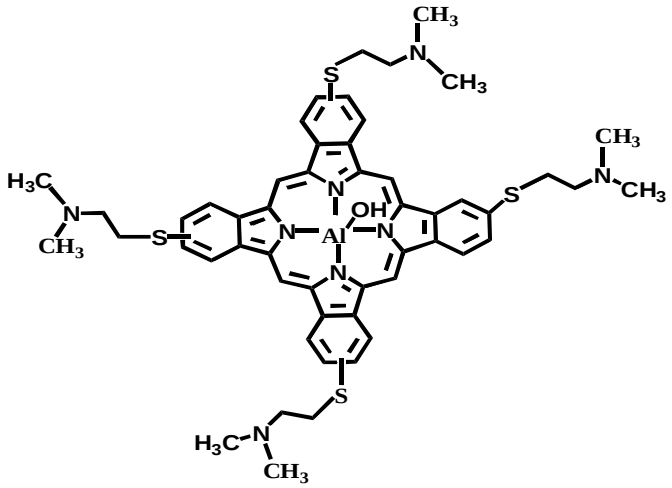 *2, (3)-Tetra-[2-(dimethylamino) ethanethio)phthalocyanino aluminium (III) hydroxide*	2

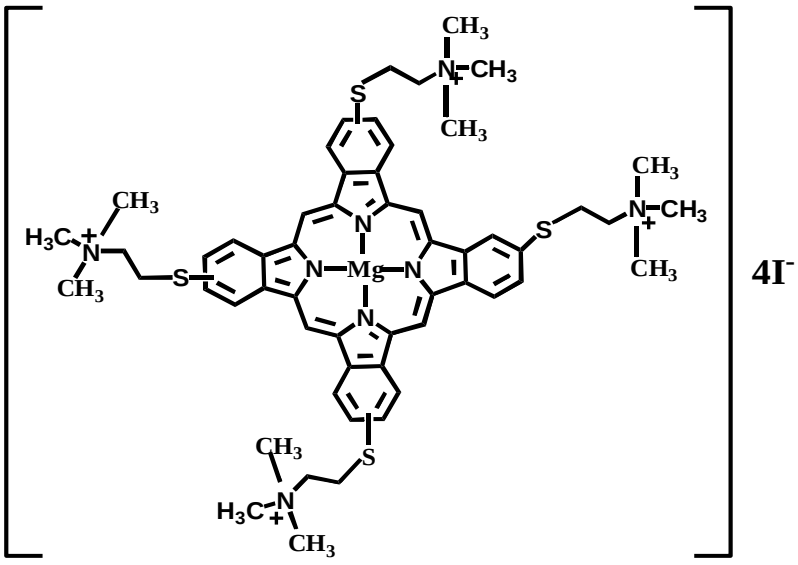

1a

Quaternized 2,(3)-Tetra[2-dimethylamino)ethanethio substituted Mg (II) phthalocyanine

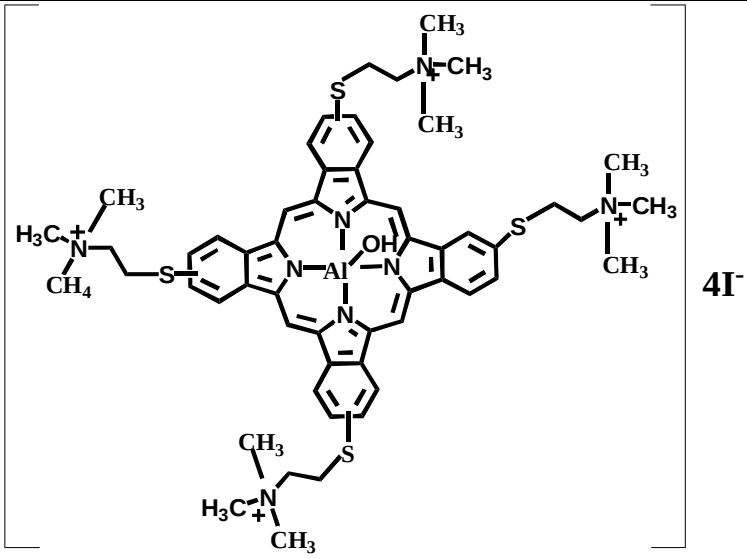

2a

Quaternized 2,(3)-Tetra[2-dimethylamino)ethanethio substituted Al(III) phthalocyanine

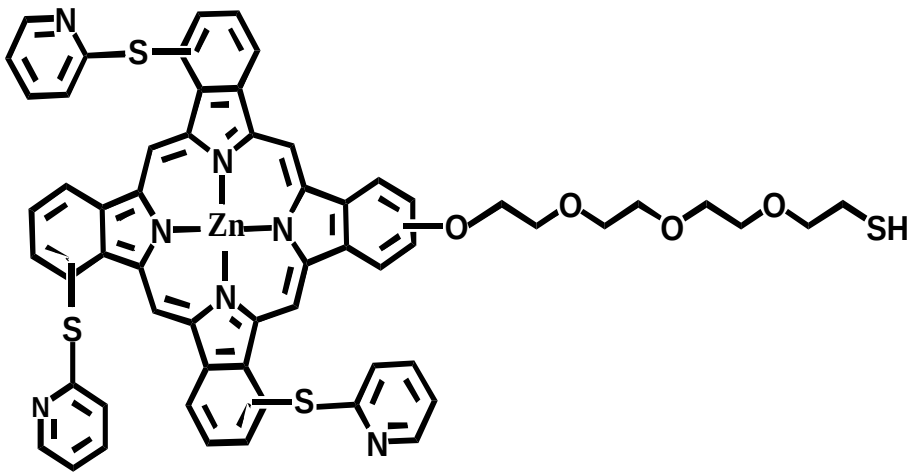

3

1,8(11),15(18)-tri-(2-mercaptopyridine)-23(24)-(4-{2-[2-(2-mercaptoethoxy)-ethoxy]ethoxy}ethoxy)phthalocyaninato zinc (II)

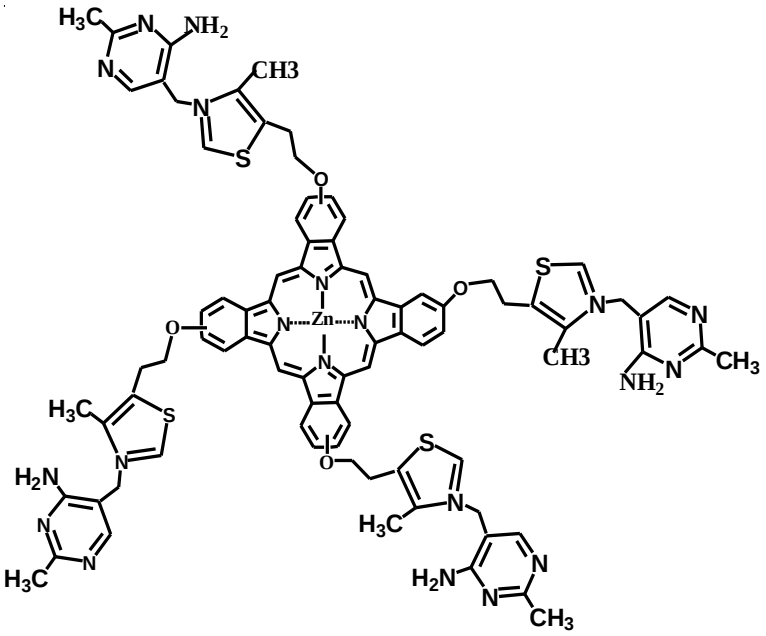

4

Tetra(4-(thiamine) substituted zinc phthalocyanine

1.2.6. Photophysical and photochemical properties

Photophysical properties of the phthalocyanines are measured by the changes in the electronic states when light is absorbed. The physical changes that take place can be explained by the Jablonski diagram (**Figure 1.8**) **[78]**.

Of interest in this work is intersystem crossing from the lowest vibronic level $\mathbf{S_1}$ to the first triplet excited state ($\mathbf{T_1}$). The process of intersystem crossing is enhanced in the presence of heavy atoms **[79]**, such as gold nanoparticles (AuNPs), which are subject of this thesis.

In the presence of molecular oxygen ($\mathbf{^3O_2}$) energy can be transferred from the excited triplet state molecules to the ground state oxygen to generate singlet oxygen ($\mathbf{^1O_2}$) which is used in photosensitization, and is of interest in this work.

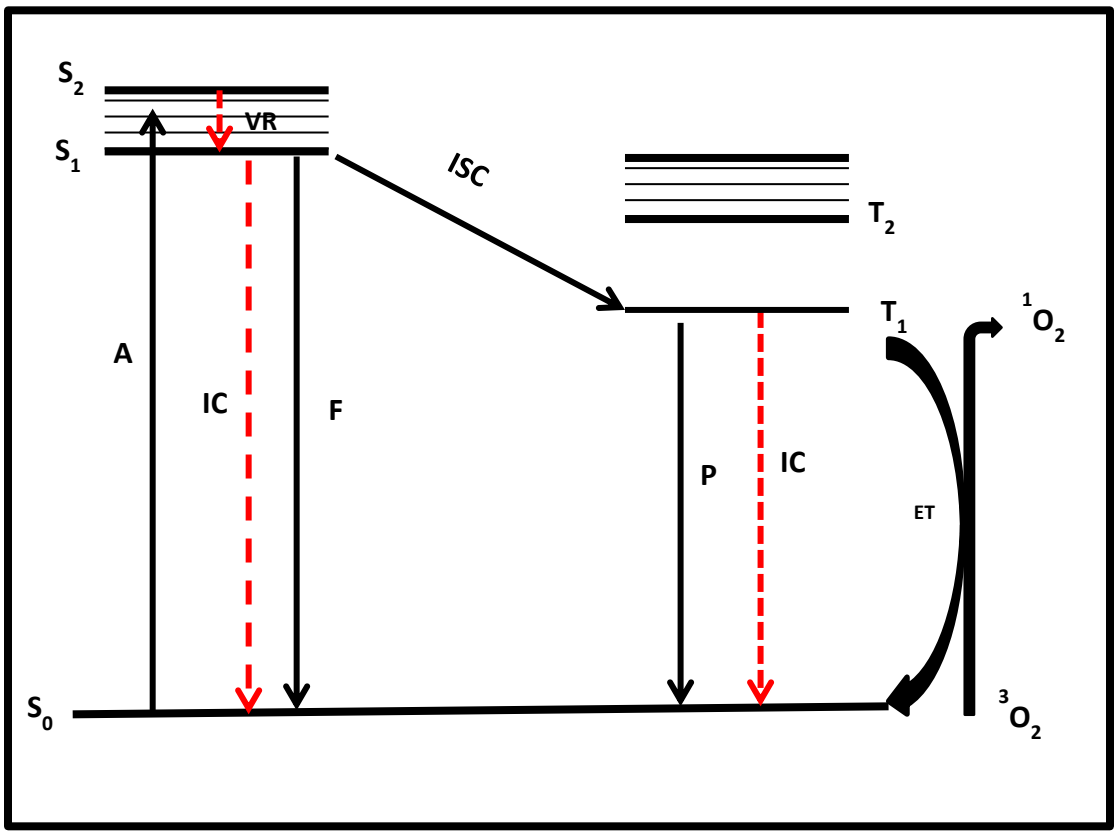

Figure 1.8: A modified Jablonski diagram showing the transition between the singlet ground state (S_0) and the electronic excited states S_1 and T_1. **(A)**=Absorption, **(IC)** = internal conversion, **(F)**= fluorescence, **(ISC)**= intersystem crossing, **(VR)**= vibrational relaxation, **(P)**= phosphorescence, **(ET)**= energy transfer.

1.2.6.1. Fluorescence quantum yield and lifetime

Fluorescence quantum yield (Φ_F) is the number of photons emitted relative to the photons absorbed. It can be determined by a comparative method **[80]** using equation **1.1**:

$$\Phi_F = \Phi_{F(std)} \frac{F.A_{std}.n^2}{F_{std}.A.n_{std}^2} \qquad \textbf{(1.1)}$$

where F and F_{std} are areas under fluorescence emission curves of the MPc complexes and the standard respectively. A and A_{std} are the absorbances of the samples and standard at the excitation wavelength and n and n_{std} are refractive indices of solvents used for samples and standard respectively. ZnPc in DMSO was used as a standard, Φ_F = 0.20, for the determination of fluorescence quantum yields **[81]**. The sample and the standard both should be excited at the same relevant wavelength. Metallophthalocyanines with heavy metals have relatively low fluorescence quantum yields because the latter promote intersystem crossing.

Fluorescence lifetime is the time a molecule spends in the excited singlet state (**S_1**) before fluorescence. Time correlated single photon counting (TCSPC) is a method used to measure fluorescence lifetimes and is used in this work. This technique detects and counts single photons. The fluorescence lifetimes of the phthalocyanines are in the order of less than 10 ns. A typical fluorescence

decay curve of a phthalocyanine in solution is shown in **Figure1.9**, **[82]**. The radiative lifetime (τ_F) is related to the non-radiative lifetime and is also used to define the behaviour of the molecule from the excited state. This is the lifetime of the molecule in the absence of the non-radiative processes and is given by **equation 1.2 [83]**.

$$\tau_0 = \tau_F / \Phi_F \qquad \textbf{(1.2)}$$

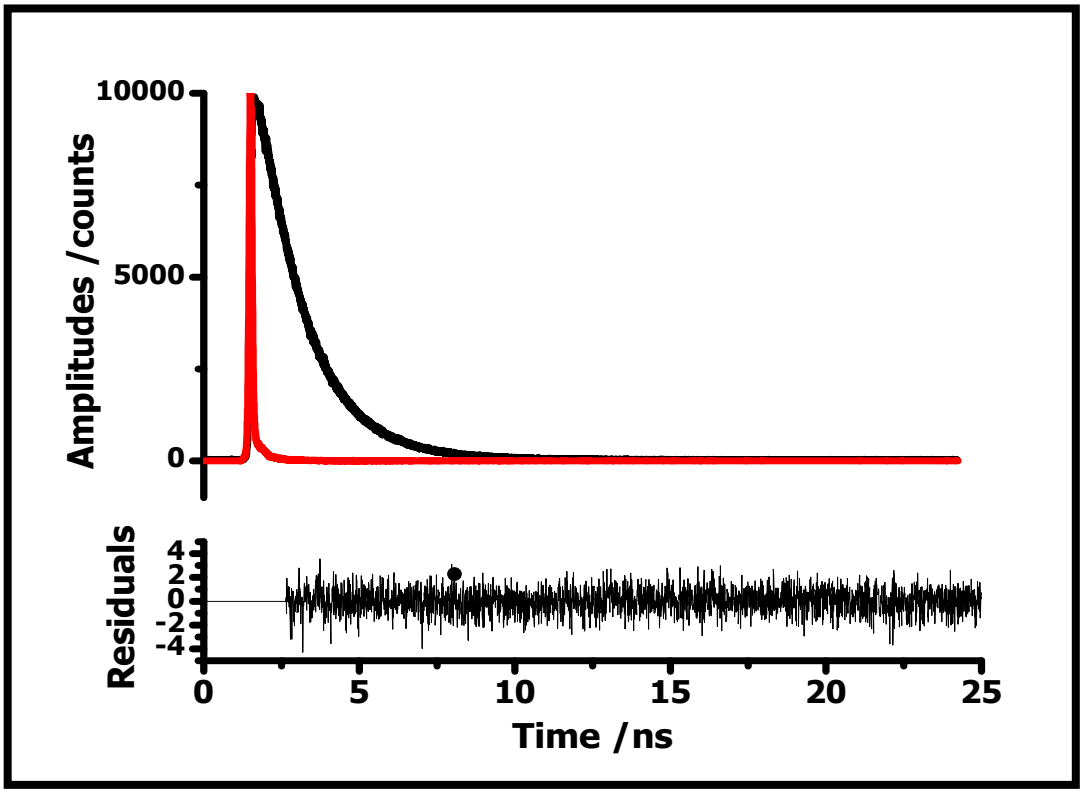

Figure 1.9: Fluorescence decay curves of a typical MPc in solution **[83]**.

1.2.6.2. Triplet quantum yield and lifetime

The laser flash photolysis technique is used to study the properties of the molecule in the triplet excited state. The triplet quantum yield (Φ_T) is used to estimate the efficiency of the molecule to populate the triplet state. The triplet quantum yields can be determined by equation **(1.3)**.

$$\Phi_T = \Phi_T^{std} \frac{\Delta A_T . \varepsilon_T^{std}}{\Delta A_T^{std} . \varepsilon_T} \qquad \textbf{(1.3)}$$

where ΔA_T and ΔA_T^{std} are the changes in the triplet state absorbances of the samples and the standard respectively. ε_T and ε_T^{std} are the triplet state molar extinction coeffients for the samples and the standard respectively. Φ_T^{std} is the triplet state quantum yield for the unsubstituted ZnPc standard Φ_T^{std} = 0.65 for ZnPc in DMSO) **[84]**.

ε_T and ε_T^{std} were calculated from the molar extinction coefficients of their respective ground singlet state, and the changes in absorbances of the ground state or the triplet state using equation **(1.4a)** and **(1.4b)**.

$$\varepsilon_T = \varepsilon_S . \frac{\Delta A_T}{\Delta A_S} \qquad \textbf{(1.4a)}$$

$$\varepsilon_T^{std} = \varepsilon_S^{std} . \frac{\Delta A_T^{std}}{\Delta A_S^{std}} \qquad \textbf{(1.4b)}$$

The triplet lifetimes can be obtained from the triplet decay curve using origin **8** software (**Figure 1.10**).

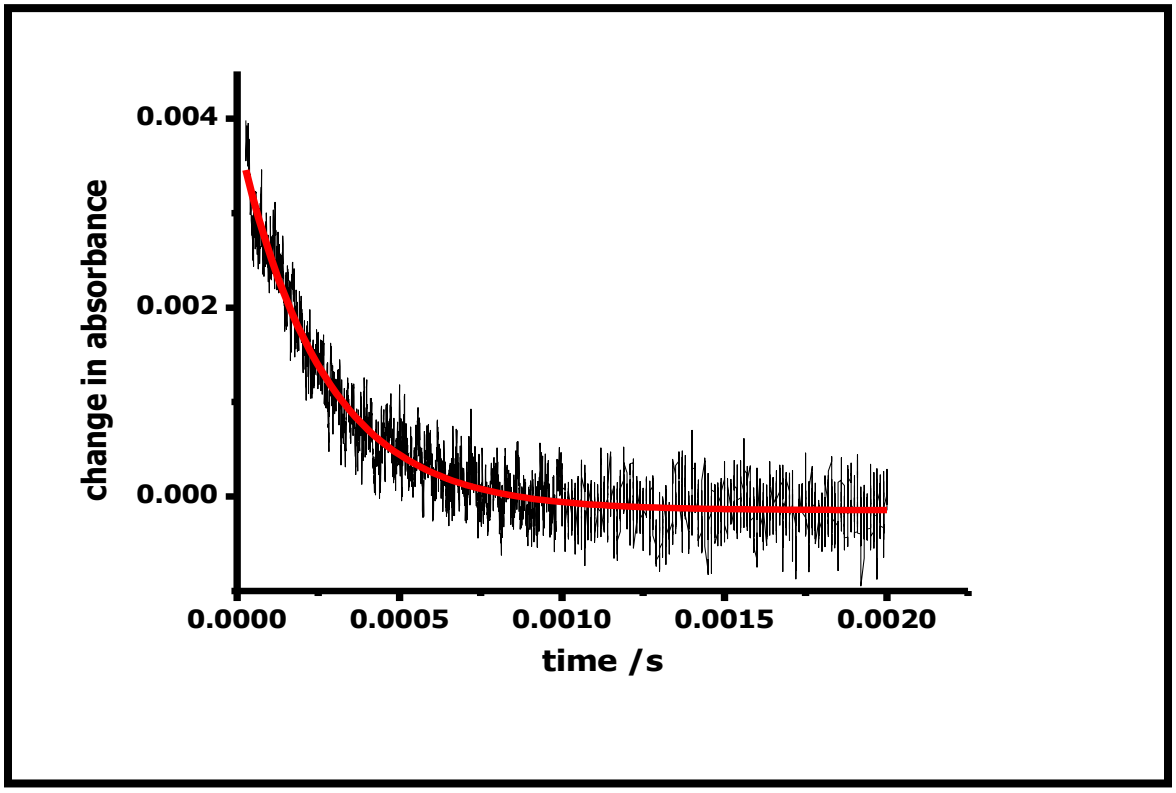

Figure 1.10: Triplet decay curves of a typical MPc in solution **[83]**.

1.2.6.3. Singlet oxygen quantum yield

Singlet oxygen production is important for photosensitizing applications of MPcs. The lifetime of the singlet oxygen is less than 100 μs in organic and aqueous solvents **[85]**. The energy for a phthalocyanine in the triplet state must be greater than 94 kJ mol^{-1} in order to achieve efficient energy transfer for the production of singlet oxygen $^1O_2$ ($^1\Delta_g$) **[65, 86]**. There are two established

methods of quantifying singlet oxygen: The chemical method requires a singlet oxygen quencher that will react with singlet oxygen as soon as it is produced in an oxygenated solution. Spectroscopic methods are then used to monitor production of singlet oxygen through the decay of a scavenger. In this work 1,3-diphenylisobenzofuran (DPBF) was used as a singlet oxygen scavenger and the relative method is used to determine singlet oxygen quantum yields. Eqn **(1.5)** is used for calculating singlet oxygen quantum yields:

$$\Phi_{\Delta} = \Phi_{\Delta}^{std} . \frac{R^{sample} . I^{std}}{R^{std} . I^{sample}} \qquad \textbf{(1.5)}$$

where (Φ_{Δ}^{std}) is the singlet oxygen quantum yield for the standard (ZnPc, Φ_{Δ}^{std}= 0.67 in DMSO)**[87]**. R^{sample} and R^{std} are the DPBF photobleaching rates in the presence of the sample under investigation and the standard, respectively. I^{sample} and I^{std} are the rates of light absorption by the sample and the standard, respectively.

Another method used in this work is the singlet oxygen luminescence method. The time resolve phosphorescence decay curve of singlet oxygen at 1270 nm is used to determine singlet oxygen quantum yield **[88]**. The dynamic course of singlet oxygen concentration can be calculated using equation **1.6** as described in reference **[89]**.

$$I(t) = B \frac{\tau_D}{\tau_T - \tau_D} [e^{-t/\tau_T} - e^{-t/\tau_D}] \qquad \textbf{(1.6)}$$

Where I (t) is the phosphorescence intensity of singlet oxygen (O_2 ($^1\Delta_g$)) at time t, τ_D is the lifetime of (O_2 ($^1\Delta_g$)) phosphorescence decay, τ_T is the triplet state lifetime and B is a coefficient involved in sensitizer concentration and singlet oxygen quantum yield. Singlet oxygen quantum yield of a phthalocyanine is then determined using equation Eq. **(1.7) [89]**:

$$\Phi_{\Delta} = \Phi_{\Delta}^{std} . \frac{B.A^{std}}{B^{std}.A} \qquad (1.7)$$

where Φ_{Δ}^{std} is the singlet oxygen quantum yield for the standard, B and B^{std} are the coefficients of the sample and the standard respectively. The singlet oxygen lifetime (τ_{Δ}) is determined by fitting the decay curves using Origin **8** software.

1.3. Nanoparticles conjugated to phthalocyanines

Gold nanoparticles (AuNPs) can be easily functionalized with photosensitizers through covalent and non-covalent methods. The displacement of the original coatings may occur through ligand exchange mechanism. This result in the adsorption of the new molecules onto the surface of the nanoparticles forming self-assembled monolayers (SAMs). This method was employed for the construction of phthalocyanine-gold nanoparticle conjugates in this work. The conjugation of gold nanoparticles to phthalocyanines has been shown to improve the photophysical and photochemical properties however, most studies have been limited to spherical gold nanoparticles **[90, 91]**. Anisotropic nanoparticles have a large surface area hence, result in higher surface density.

In this work metallophthalocyanines are conjugated to spheres, nanorods and bipyramids. The effect of aspect ratio of the gold nanorods on the photophysical properties of phthalocyanines was explored for the first time in this work. It has been reported that AuNRs possess superior long blood circulation time due to the anisotropic geometry and hence, the interest in anisotropic nanoparticles in this work **[92]**. Conjugation of bipyramids to phthalocyanines is also of interest in this work and we did not find any similar study in the literature. **Table 1.2** shows some of the phthalocyanines conjugated to gold nanoparticles that are found in literature **[93-98]**. As **Table 1.2** shows, not much work has been done on conjugation of Pcs to anisotropic nanoparticles hence this is the main focus of this work.

Table 1.2: Phthalocyanines conjugated to gold nanoparticles.

Phthalocyanines	Φ_F	Φ_T	Φ_Δ	**NPs**	**[Ref]**
1,4,8,11,15,18-Hexahexyl-22-methyl-25-(11-mercaptoundecyl phthalocyaninato zinc	-	-	0.65	spheres	**[73]**
1,1',4, 4', 8,8', 15, 15',18,18', 22, 22'-Tetradecakisdecyl-25, 25'-(11, 11' dithiodiudecyl) diphthalocyanine zinc	-	-	-	spheres	**[93]**
Tetrakis2,(3)[(1,6hexanedithiol) phthalocyanine]zinc(II)	0.07	0.80		spheres	**[94]**
Tetrasulfonated Aluminium phthalocyanine	-	-	-	Rods	**[95]**
1,4di[(3acetylsulfonylpropoate)propyloxy]-9-(10),16(17),23(24)-tri[tert-butyl]phthalocyanine	-	-	-	spheres	**[96]**
Tetra(phenylthio)phthalocyanato zinc (ZnPc(SPh)$_4$)	0.09	-	-	spheres	**[97]**

[8,15,22-tris-(naptho)-2-(amidoethanethiol)phthalocyanato] zinc (II)	0.04	0.71	-	spheres	
2(carboxy)phthalocyanine],2,9,17,23-tetrakis-[(1,6-hexanedithio) phthalocyaninato] zinc (II)	0.07	069	-	spheres	**[75]**
[9,16,23-tris-(5-trifluoromethyl-2-mercaptopyridine-phthalocyanine	0.02	0.71		spheres	
(OH)AlSmix	[a]0.67 [b]0.44	-	-	Spheres, stars	**[98]**
ZnPcSmix	[a]0.08 [b]0.05	-	-		
2,(3)-[tetra-(mercaptoacetic acid phthalocyaninato) zin (II)	[a]0.01 [b]0.09	-	-		
2,(3)-[tetra-(mercapropanoic acid phthalocaninato) zinc(II)	[a]0.03 [b]0.32	-	-		

[a]= with spheres,[b]=with stars

1.4. Photodynamic antimicrobial chemotherapy (PACT)

1.4.1. General introduction

The worldwide growing resistance of pathogenic microbes against antibiotics has fueled research on PACT as an alternative method to deal with bacterial and fungal infections. PACT requires a photosensitizer which can be illuminated with light to cause oxidative destruction of microbial pathogens. The photoinactivation of microbes was demonstrated in the 1990's **[99-101]**.

The photoinactivation mechanism involves type **I** and type **II** mechanisms (**Scheme1.4**). Type **I** process involves an electron transfer from the photosensitizer in the triplet state which result in the formation of toxic oxidation products such as superoxide, hydrogen peroxide and hydroxyl radicals. In type **II** the excited photosensitizer in the triplet state transfers energy to the ground state molecular oxygen to produce cytotoxic singlet oxygen.

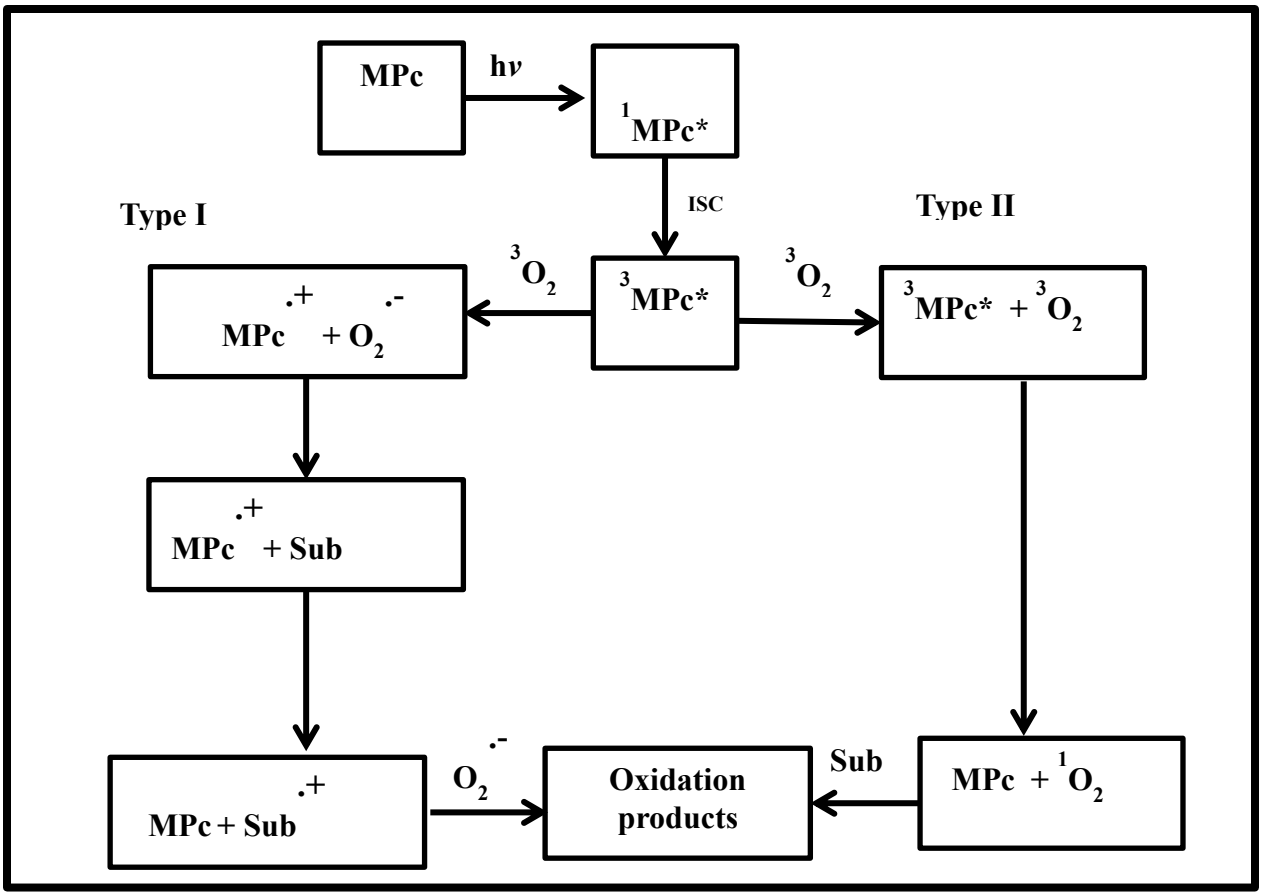

Scheme 1.4: A schematic representation of Type I and II photochemical mechanism. Sub = substrate.

1.4.2. Microorganisms studied in this work

Escherichia coli (*E. Coli*) and *Candida Albicans (C. Albicans)* are employed in this work

E. Coli is a common Gram negative bacterium that can be found in the human and animal digestive tracts. Photoinactivation of Gram (**-ve**) bacteria is more difficult compared to the Gram (**+ve**) bacteria because of the differences in the structures. The structure of Gram (**-ve**) bacteria consist of two membranes which is a cytoplasmic and an outer membrane **[99]**. The outer membrane is made up of a negatively charged lipopolysaccharide layer which becomes impermeable to neutral and negatively charged photosensitizers **[102]**. A number of cationic phthalocyanines have been used to photoinactivate *E. Coli* (**Table 1.3**) however; the studies using phthalocyanines conjugated to gold nanoparticles are limited.

Candida Albicans is the most predominant fungal pathogen found in invasive bloodstream infections **[103]**. Fungal antimicrobial photoinactivation with phthalocyanines have been reported in literature despite the complicated structure of these microorganisms (**Table 1.3**). Fungi cells contain a rigid cell wall that is made up of polysaccharide polymers such as β-glucans, chitin and glycoproteins **[104]**. Therefore, photoinactivation of fungi is more difficult compared to bacteria because the photosensitizer has to penetrate the fungal cell wall and membrane for effective PACT. Photoinactivation of both Gram (-ve) bacteria *E. Coli* and fungi is reported in this work.

1.4.3. Metallophthalocyanines in PACT

The application of phthalocyanines in photodynamic antimicrobial chemotherapy of bacteria is a growing field and promising for the treatment of pathogenic microbes. Cationic water soluble phthalocyanines are preferred over neutral and anionic for the photoinactivation of both bacteria and fungi (**Table 1.3**). There have been a lot of PACT studies that involves positively charged phthalocyanines. Some of the phthalocyanines that have been used in PACT that are found in literature are summarized in **Table 1.3**. Phthalocyanines absorb light within the biological window and produce high singlet oxygen quantum yields hence the increasing interest in the use of these molecules in PACT.

1.4.4. Gold nanoparticles in PACT

Gold nanoparticles can bind to bacteria and thus enhance photoinactivation by facilitating the binding of the photosensitizer to the bacteria **[105]**. Singlet oxygen quantum yields required for PACT can be enhanced by conjugating with gold nanoparticles which provide the heavy atom effect. Gold nanoparticles also have the ability to absorb light and rapidly convert it to heat through non-radiative processes. For this reason, gold nanoparticles have potential as photothermal agents in photothermal inactivation of bacteria **[106]**. Photosensitizers have been conjugated with gold nanoparticles to enhance photoinactivation however, most of these studies focused on spherical gold

nanoparticles. The photoinactivation of *Staphylococcus aureus* bacteria was enhanced by conjugation of gold nanoparticles to indocyanine dye through a synergetic effect of photodynamic and photothermal therapies **[107]**. Enhanced photoinactivation of bacteria have also been observed in dye-gold nanoparticles in which the gold nanoparticles are used to catalyse the production of reactive oxygen species (ROS) **[108-110]**. The use of gold nanoparticles in combination with phthalocyanines has not been explored in detail especially the use of non-spherical nanoparticles (**Table 1.3**) **[111-120]**. Hence, the effect of both spherical and anisotropic gold is explored in this work.

Table 1.3: Phthalocyanines and phthalocyanines-gold nanoparticles used in PACT.

Phthalocyanines	microorganism	NPs	[Ref]
(Cationic) Zinc(II)2, 9, 16,23-tetrakis[4-(N-methylpyridyloxy)]-phthalocyanine iodide	*Candida Albicans, Escherichia Coli, Enterococcus seriolicida, Pseudomonas aeruginosa*	-	**[111,112]**
(Cationic) {2(3),9(10),16(17),23(24)-tetrakis[1,3-bis(N,N,N-trimethylammonium)-2-propyloxy]phthalocyaninato}zinc(II) iodide	*Escherichia Coli Staphylococcus aureus*	-	**[113]**
Cationic pyridinium zinc phthalocyanine (PPC)	*Escherichia Coli,*	-	**[114]**

(Cationic)*Lead(II)2,9,23-tetrakis[4-(N-pyridoloxy)]-phthalocyanine (PbTePyPc)*	*Escherichia Coli*	-	**[115]**
Anionic tetra-sulphonated phthalocyanine (TSPc), neutral tetra-diethanolamine phthalocyanine (TDEPc)	*Pseudomonas aeruginosa, Enterococcus seriolicida*	-	**[116]**
(Cationic) 2[2,4,6tris(trimethylammoniummethyl)phenoxy]phthalocyaninato zinc(II) iodide	*Escherichia Coli, Pseudomonas aeruginosa, Staphylococcus aureus*	-	**[117]**
Cationic tetrakis-(3-methylpyrodyloxy)-phthalocyanine zinc(II) , Anionic tetrakis-(4-Sulfophenoxy) phthalocyanine zinc(II)	*Staphylococcus aureus, Pseudomonas aeruginosa, Candida Albicans*	-	**[118]**

(Anionic) ***4-tetrakis-(5-trifluoromethyl-2-pyridoxy)phthalocyaninato zinc (II)-poly-L-lysine***	*Staphylococcus aureus*	spheres	**[119]**
(Neutral) Bis-(1,6-hexanedithiol)SiPc (SiHDTPc)	*Staphylococcus aureus, Bacillus Subtilis*	spheres	**[120]**

1.6. Summary of aims

The aims of this thesis can be summarized as follows:

- Synthesize and characterize metallophthalocyanines substituted with sulfur and nitrogen groups for binding with gold nanoparticles.
- Study the spectroscopic behaviour (ground state electronic absorption, excitation and fluorescence emission) of MPcs.
- Study the photophysical (fluorescence quantum yields, fluorescence lifetimes, triplet quantum yields and triplet lifetimes) and photochemical

properties (singlet oxygen quantum yields) of the MPcs alone and in the presence of nanoparticles.

- Synthesize and characterize spherical and non-spherical gold nanoparticles.
- Synthesize and characterize phthalocyanine-gold nanoparticle conjugates.
- Study the effect of shaped nanoparticles, phthalocyanine and phthalocyanine-gold NPs conjugates in photodynamic antimicrobial and antifungal chemotherapy.

Chapter 2
Experimental

This chapter reports on all the experiments procedures, synthetic procedures and methods of characterization for all complexes used during the course of the study.

2.1 Materials

2.1.1 Solvents

Ethanol, chloroform, n-hexane, diethylether, n-pentanol, acetone, dimethylformamide (DMF), dimethylsulphoxide (DMSO), dimethyl amino ethanol (DMAE), dichloromethane (DCM), tetrahydrofuran (THF), toluene, thionyl chloride and methane sulfonyl chloride were purchased from Merck. All solvents were dried and purified as described by Perrin and Armarego [**121**]. Deuterated dimethylsulfoxide (DMSO-d_6), deuterated acetone (Acetone-d_6) and deuterated dimethylformamide (DMF-d_5) from Sigma Aldrich. Nitric and hydrochloric acids were purchased from B&M Scientific. Deionized water was used for all aqueous solution preparations.

2.1.2 Reagents for the synthesis and characterization of phthalocyanines

Magnesium chloride, aluminium chloride, potassium carbonate, zinc phthalocyanine (ZnPc), diphenylisobenzofuran (DPBF), zinc chloride, thiamine chloride were purchased from SIGMA Aldrich. 1, 8-diazabicyclo [5, 4, 0] undec-7-ene (DBU) and methyl iodide were obtained from Fluka. The purity of the products was tested in each step by thin layer chromatography (TLC) and silica

$60PF_{254}$. All other reagents were obtained from commercial suppliers. Phosphate-buffered solutions of pH 7.4 and 9 were prepared using appropriate amounts of Na_2HPO_4, KH_2PO_4 and chloride salts, dissolved in ultra-pure water.

2.1.3. Reagents for the synthesis of gold nanoparticles

Trisodium citrate (99%), $HAuCl_4$, sodium borohydride, trisodium citrate (99%), cetyltrimethylammonium bromide, (CTAB), silver nitrate, ascorbic acid, tetraoctylammonium bromide (TOABr) and gold standard for ICP (99%) were purchased from Sigma Aldrich.

2.1.4. Reagents for the microbial studies

Nutrient agar (**HG 0000C1.500**) and nutrient broth (**HG000C24.500**) were purchased from Merck. Distilled water was used for the preparation of phosphate buffer saline [NaCl, KCl, Na_2HPO_4, KH_2PO_4] (PBS, pH 7.04), agar and broth solutions. Deionized water was used for all solution preparations. KWIK Stik *C. albicans* (**ATCC 24433**) and *E. coli* (**ATCC 25922**) crystal strains were purchased from Microbiologics.

2.2. Equipment

(i) Mass spectral data were collected with a Bruker AutoFLEX III Smartbeam TOF/TOF Mass spectrometer. The instrument was operated in positive ion mode using an m/z range of 400-3000. The voltage of the ion sources were set at 19 and 16.7 kV for ion sources 1 and 2 respectively, while the lens was set

at 8.50 kV. The reflector 1 and 2 voltages were set at 21 and 9.7 kV respectively. The spectra were acquired using dithranol as the MALDI matrix, using a 337 nm nitrogen laser.

(ii) ^{1}H nuclear magnetic resonance signals were recorded on a Bruker AMX 400 MHz NMR spectrometer.

(iii) Infrared spectra were recorded on Perkin Elmer Spectrum 100 FT-IR spectrometer.

(iv) Elemental analyses for CHNS were done using a Vario-Elementar Microcube ELIII Series.

(iv) Ground state electronic absorption spectra were performed on Shimadzu UV-2550 spectrophotometer,

(v) Fluorescence excitation and emission spectra were recorded on a Varian Eclipse spectrofluorimeter.

(vi) Fluorescence lifetimes were measured using a time correlated single photon counting (TCSPC) setup (FluoTime 200, Picoquant GmbH) (**Figure 2.1**). The excitation source was a diode laser (LDH-P-670 driven by PDL 800-B, 670 nm, 20 MHz repetition rate, 44 ps pulse width, Picoquant GmbH). Fluorescence was detected under the magic angle with a peltier cooled photomultiplier tube (PMT) (PMA-C 192-N-M, Picoquant) and integrated electronics (PicoHarp 300E, Picoquant GmbH). A monochromator with a spectral width of about 8 nm was used to select the required emission wavelength band. The response function of the system, which was measured with a scattering Ludox solution (DuPont),

had a full width at half-maximum (FWHM) of about 300 ps. The ratio of stop to start pulses was kept low (below 0.05) to ensure good statistics. All luminescence decay curves were measured at the maximum of the emission peak. The data were analysed with the program FluoFit (Picoquant, GmbH).

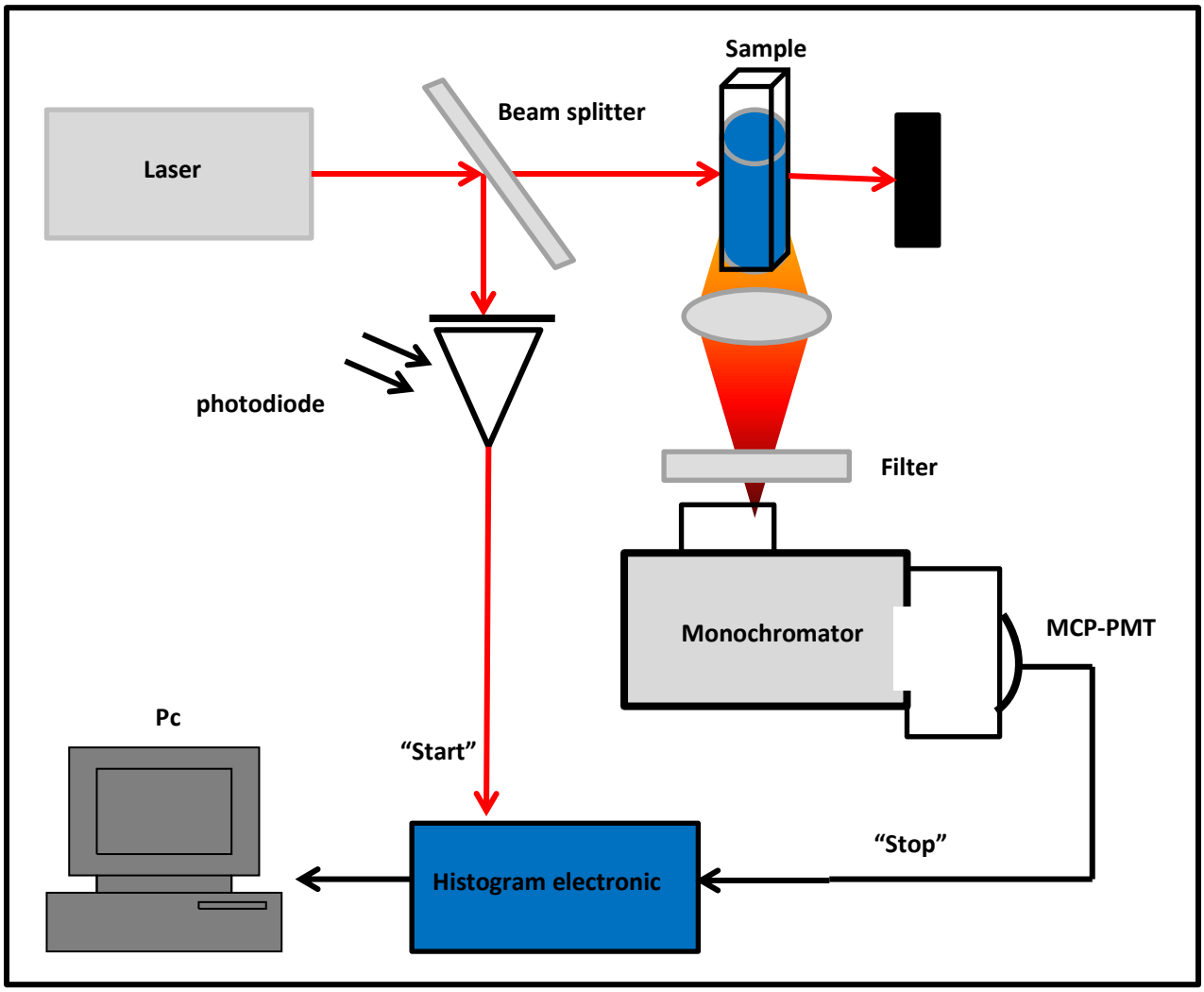

Figure 2.1: A schematic diagram of the setup of the TCSPC equipment (TCSPC). MCP-PMT = (multi-channel plate detector)-Photomultipier tube, Pc = personal computer.

(vii) The triplet decay kinetics data were collected on a laser flash photolysis system (**Figure 2.2**). The light pulses used in excitation were produced by a Quanta-Ray Nd: YAG laser (1.5 J/9 ns), pumping a Lambda Physik FL 3002 dye laser (Pyridin 1 in methanol). The analyzing beam source was from a Thermo Oriel 66902 xenon arc lamp, and a photomultiplier tube was used as a detector. Signals were recorded with a two channel, 300 MHz digital real time oscilloscope (Tektronix TDS 3032 C). The samples were placed in a 1 cm path length fluorescence spectrophotometric cell, degassed by bubbling argon for 30 min and irradiated at the Q band maxima. The triplet lifetimes were determined by exponential fitting of the kinetic curves using the Origin Pro8 software.

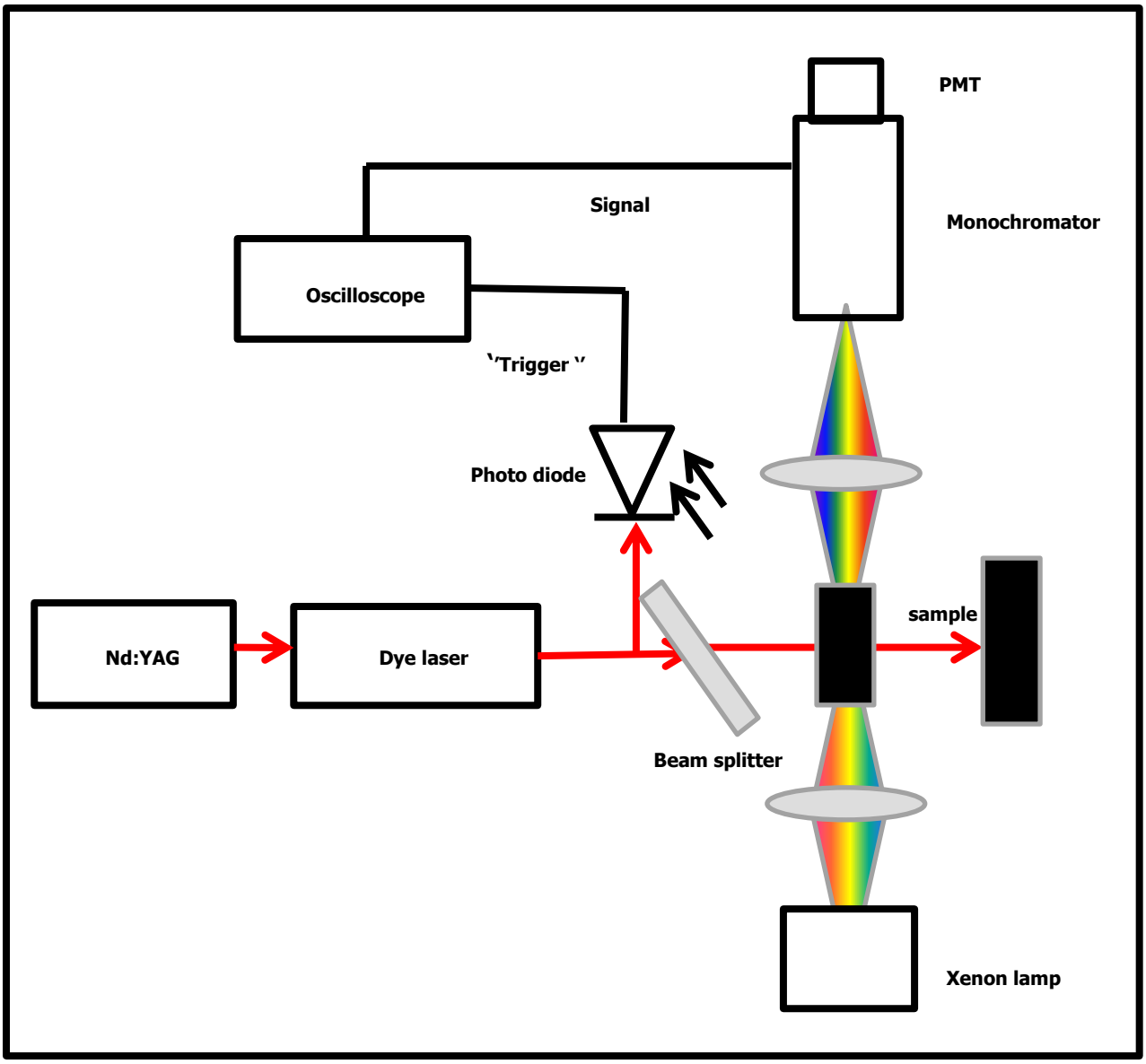

Figure 2.2: Schematic diagram of laser flash photolysis setup.

(PMT= photomultiplier tube)

Determination of singlet oxygen quantum yields and irradiation of microbial plates were done using the General Electric Quartz lamp (300 W) as irradiation source, a 600 nm glass (Schott) and water filters were used to filter off ultra-violet and far infrared radiations, respectively **(Figure 2.3)**. An interference filter 670 nm with band of 40 nm was placed in the light path just before the cell containing the sample. The intensity of the light reaching the reaction vessel was measured with a power meter (POWER MAX 5100, Molelectron Detector Inc).

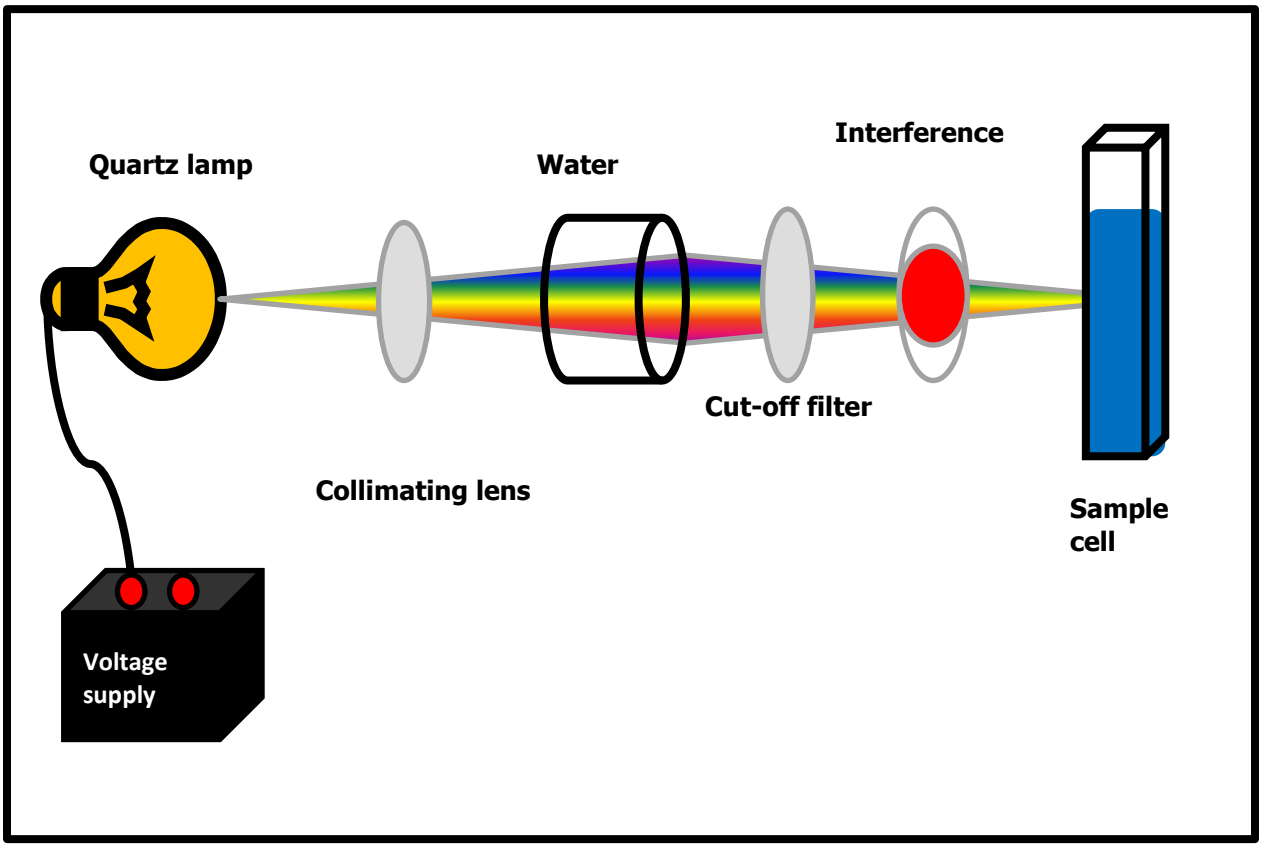

Figure 2.3: Schematic diagram of photo-irradiation setup.

(viii) The time resolved singlet oxygen phosphorescence at 1270 nm was also used to determine the singlet oxygen quantum yields in aqueous solution. The dynamic phosphorescence decay of singlet oxygen ($^1O_2$) species was demonstrated using its phosphorescence at 1270 nm. For these studies, an ultra-sensitive germanium detector (Edinburgh Instruments, EI-P) combined with a 1000 nm long pass filter (Omega, RD 1000 CP) and a 1270 nm band-pass filter (Omega, C1275, BP50) was used to detect $^1O_2$ phosphorescence under excitation using a Quanta-Ray Nd:YAG laser which provided a 400 mJ, 9 ns pulses of laser light at 10 Hz pumping a Lambda-Physik FL3002 dye laser (Pyridin 1 dye in methanol), with a pulse period of 7 ns and repetition rate of 10 Hz. The near-infrared phosphorescence of the samples were focused onto the germanium detector using a lens (Edmund, NT 48-157) with the detection direction perpendicular to the excitation laser beam. The detected signals were averaged with a digital oscilloscope (Tektronics, TDS 360) to show the dynamic decay of $^1O_2$. The data obtained was analyzed using ORIGIN Pro 8 software.

(ix) Transmission electron microscope (TEM) images were obtained using a JEOL TEM 1210 transmission electron microscope at 100 kV accelerating voltage. TEM samples were prepared by placing a drop of conjugates or nanoparticle solution on the sample grid and allowing it to dry before measurements.

(x) X-ray powder diffraction (XRD) patterns were recorded on a Bruker D8, Discover equipped with a Lynx Eye Detector, using Cu Kα radiation (λ = 1.5405 Å, nickel filter). Data were collected in the range from 2θ = 5° to 100°, scanning at 1° min^{-1} with a filter time-constant of 2.5s per step and a slit width of 6.0 mm. Samples were placed on a zero background silicon wafer slide. The X-ray diffraction data were treated using Eva (evaluation curve fitting) software. Baseline correction was performed on each diffraction pattern by subtracting a spline fitted to the curve background and the full width at half maximum values used in this study was obtained from the fitted curves.

(xi) X-ray photoelectron spectroscopy (XPS) data were collected using a Kratos Axis Ultra DLD, using an Al (monochromatic) anode, equipped with charge neutralizer and the operating pressure kept below 5 x 10^{-9} torr. For wide/survey XPS scans, the following parameters were used: emission current was kept at 5 mA and a dual anode (AI) voltage at 15kV. The resolution used to acquire wide/survey scans was at 160 eV pass energy using a hybrid lens in the slot mode. The centre used for the scans was at 520 eV and the width at 1205 eV, with steps at 1 eV and dwell times at 300 ms. For the high resolution scans, the resolution was changed to 10 eV pass energy in the slot mode.

(xii) Energy dispersive spectroscopy (EDX) was done on an INCA PENTA FET coupled to the VAGA TESCAM using 20 kV accelerating voltage.

(xiii) The concentration of gold atoms (Au^0) in AuNPs was determined using a ThermoElectron ICAP 6000 inductively coupled plasma (ICP) spectrometer with

an optical Emission spectroscopy (OES) detector. Gold nanoparticles were digested by addition of 3 mL of aqua regia for ICP measurements. Standard calibration was achieved at concentrations ranging from 0.5 to 5 ppm. A minimum of three measurements were made for each sample of gold nanoparticles. Gold was analysed at wavelengths of 208, 242 and 267 nm.

2.3. Synthesis of gold nanoparticles (AuNPs)

2.3.1. Citrate capped spherical AuNP (citrate-AuNS)

*Citrate capped AuNS were conjugated to water soluble Pcs **1a** and **2a***

Gold nanoparticles capped with citrate were synthesized according to the method reported in literature by Lee and Meisel [**122**]. Briefly, an aqueous solution of $HAuCl_4$ (0.0005 M) was heated to boiling followed by addition of trisodium citrate 10 mL (1 %). The solution turned ruby red and was stirred for 30 mins and was cooled to room temperature.

2.3.2. TOABr capped spherical AuNP (TOABr-AuNS)

*TOABr-AuNS (organic soluble) were conjugated to a non-water soluble Pc **3**.*

Synthesis of TOABr stabilized AuNPs has been reported before [**96**]. Briefly, 2 mL of $HAuCl_4$ aqueous solution (25 mM) was vigorously stirred with 3 mL toluene solution of TOABr (85 mM,) until all of the gold chloride was

transferred to the organic phase. The reducing agent, $NaBH_4$, in an aqueous solution (36 mM, 2 mL) was added dropwise for 10 min. The Au solution changes color from brownish yellow, to milky, to scarlet and finally purple. After the addition of $NaBH_4$, the mixture was stirred vigorously for 30 min. The gold nanoparticles were washed repeatedly with deionized H_2O to remove the reducing agent and were stored in a minimum amount of toluene (1 mL).

2.3.3. Synthesis of CTAB capped nanorods (AuNRs)

Seed solution (used as nanospheres, AuNS):

CTAB was used to cap AuNS (CTAB-AuNS) for comparison with capped AuNRs. CTAB was used here as a shape directing agent for the formation of anisotropic AuNPs.

The seed AuNS solution was prepared following literature methods [**23**], with slight modifications: aqueous solution of 2.5×10^{-4} M (5 mL) $HAuCl_4$ was mixed with 10 mL of 0.1 M CTAB solution, and the mixture stirred for 2 min. Then, 0.6 mL of an ice cold aqueous solution of 0.01 M $NaBH_4$ was added, and the mixture hand shaken at 2 min intervals. The solution was allowed to stand for 2 hr and then used for the subsequent synthesis of shaped AuNPs.

Growth of gold nanorods (AuNRs (2.0), AuNRs (3.2) AuNRs (4.7) and AuNRs (7.1) *(numbers in brackects refered to aspect ratio)*

*AuNRs (**2.0**), (**4.7**) and (**7.1)** were studied with complex **4** while (**3.2**) was studied with **2a** and compared with AuBPs, see **Table 3.1**.*

The growth solution was prepared according to literature [**23**] by mixing 10 mL of 0.1 M CTAB, 5 mL of 1×10^{-4} M $HAuCl_4$ and 0.004 M $AgNO_3$, **Table 2.1**. The aspect ratio of the nanorods was adjusted by adding different amounts of 0.004 M $AgNO_3$ of 0.19, 0.22, 0.25 and 0.5 mL for AuNRs with aspect ratios of 7.1, 4.7, 3.2 and 2.0, respectively. To this solution, 0.07 mL of 0.1 M ascorbic acid (A.A) was added and the reaction turned colourless. Then the seed solution CTAB-AuNS (15 μL) prepared above was added and the mixture was hand shaken and left undisturbed between 30-37 °C for 24 h. AuNRs were purified by centrifuging for 20 min at 2000 rpm to remove the unreacted gold and spherical gold nanoparticles. The supernatant was removed and the resulting pellet of AuNRs was dissolved in 3 mL of distilled water. The AuNRs of different aspect ratios are represented as AuNRs (**2.0**), AuNRs (**3.2**), AuNRs (**4.7**) and AuNRs (**7.1**).

2.3.4. Synthesis of CTAB-AuBPs (BPs = bipyramids)

*CTAB-AuBPs were synthesized for comparison with CTAB-AuNRs (**3.2**) and CTAB-AuNS. These nanoparticles were studied with Pc **2a**.*

AuBPs were synthesized the same way as the nanorods except the silver concentration was increased to 0.04 M, **Table 2.1**. AuBPs were separated from unreacted gold and nanospheres (by-products) by centrifuging the gold solutions at 2000 rpm for 20 mins. The supernatant was removed and the solid nanoparticles were dispersed in 3 mL of distilled water.

Table 2.1: Reaction conditions for the synthesis of anisotropic gold nanoparticles.

Sample	[CTAB] (M)	[$HAuCl_4$] (M)	[$AgNO_3$] (M)	[A.A] (M)[a]	$NaBH_4$ (M)
AuNS	**0.1**	**2.5×10^{-4}**	**-**	**-**	**0.01**
AuNR	**0.1**	**2.5×10^{-4}**	**0.004**	**0.1M**	**-**
AuBP	**0.1**	**2.5×10^{-4}**	**0.04**	**0.1M**	**-**

[a] A. A = ascorbic acid.

2.4. Synthesis of Phthalocyanines

Zinc tetrasulfophthalocyanine (ZnTSPc) was synthesized and purified according to well known procedures [**123**]. $AlPcS_{Mix}$ (containing a mixture of sulfonated derivatives and used as a standard in the determination of singlet oxygen quantum yields in water) was synthesized according to literature methods [**124**]. 4-Nitrophthalonitrile (**5**), **Scheme 3.1**, [**125, 126**], 4-[2-(dimethylamino) ethanethio] phthalonitrile (**7**) **Scheme 3.2** [**70**], (4-(2-{2-[2-(2-hydroxyethoxy) ethoxy] ethoxy}-ethoxy) phthalonitrile (**8**) **Scheme 3.4** [**127-129**] and 3-(2-mercaptopyridine) phthalonitrile (**9**) **Scheme 3.4** [**130**] were synthesized and purified according to literature procedures.

2.4.1. Synthesis of 4-(thiamine) phthalonitrile (6) (Scheme 3.1)

Thiamine hydrochloride**,** (6.34 g (18 mmol) was added to compound **5** (1.5 g, 9.4 mmol) in DMF under argon. After stirring for 15 min at room temperature, K_2CO_3 was added (5 g, 36 mmol) in portions. The reaction mixture was stirred at room temperature for 2 days. The mixture was then poured into ice and the precipitate was filtered and dried. Yield: 2.4 g (65%) IR ($\upsilon max/cm^{-1}$): 2228 (C-N), 3032-3044 (Ar-CH), 2954 (Alph-CH) 3361 (N-H), 1594 (C=C). 1H NMR (acetone-D6):8.18 (s, 1H, Ar-H), 7.97 (d, 1H, Ar-H), 7.90 (d, 1H, Ar-H), 7.79 (s, 1H, Ar-H), 7.76 (s, 1H, Ar-H), 4.33 (s, 2H, NH_2), 3.11 (t, 2H, O-CH_2), 2.89 (t, 2H, -CH_2), 2.75 (s, 2H, -CH_2), 2.36 (s, 3H, CH_3), 2.23 (s,

3H,CH_3). Anal. Calc for $C_{20}H_{19}N_6OS$: C 61.37, H 4.89, N 21.46, S 8.19; Found: C 61.26, H 4.76, N 21.35, S 7.98.

2.4.2. Synthesis of 2,(3)-tetra[2(dimethylamino)ethanethio)phthalocyanino magnesium (II) (1) (Scheme 3.2)

Compound **7** (0.35 g, 1.5 mmol) was added to dry n-pentanol (3.0 mL) in the presence of excess anhydrous $MgCl_2$, a catalytic amount of DBU was then added, and the mixture was left stirring and heated to 140 ^oC for 12 hr under an argon atmosphere. After cooling to room temperature, an ethanol/water (1:1) mixture was added and the resulting precipitate centrifuged and washed several times with water. The product was purified on a silica gel column with diethyl ether/DMF (9:1) as mixture eluent. Yield: 0.12 g, (34 %). IR: v_{max}/cm^{-1}: 3014, 3006 (Ar-C-H), 2934, 2854 (Aliph-C-H),1448 (C=C), 1328, 1064, 977. ^1H NMR (DMSO-d_6): δ 8.62-7.47 (m, 12H, Ar-H), 3.5 (t, 8H, SCH_2), 2.89 (t, 8H, NCH_2), 2.47 (s, 24H, CH_3). MALDI-TOFMS: Calc. *m/z*: 949.57, Found: 949.6, 716.8 [M-4($CH_2N(CH_3)_2$]$^+$, 891.1 [M-$CH_2N(CH_3)_2$]. UV-vis (DMSO) λ_{max} /nm (log ε) 361 (4.5), 626 (4.2), 693(4.9). Calc. for $C_{48}H_{52}MgN_{12}S_4$: C 60.71, H 5.52, N 17.70, S 13.51; Found: C 61.02, H 6. 25, N 16.63, S 12.99.

2.4.3. 2,(3)tetra[2-(dimethylamino) ethanethio)phthalocyanito aluminium (III)hydroxide (2) (Scheme 3.2)

Compound **2** was synthesized and purified using same method as complex **1** with some modifications**.** A mixture of Compound **7** (0.35 g 1.5 mmol) was reacted with an excess of $Al(OH)_3$ in n-pentanol (2 mL) in the presence of catalytic amounts of DBU. The mixture and heated under reflux for 12 hr at 140 ^oC. The reaction mixture was cooled to room temperature and a dark green product was precipitated in ethanol/water (1:1) mixture and then washed with ethanol. The product was purified on a silica gel column using the same eluent as in compound **1**. Yield: 0. 14 g**,** (40%); IR, ν_{max}/cm^{-1} 3288 (OH), 3009 (Ar-C-H), 2933-2763 (C-H), 1589, 1456 (C=C), 1368, 1316, 1061, 963; ^1H NMR (DMSO-d_6): 8.9 (s, 12H, H-Ar), 3.47 (t, 8H, SCH_2), 2.9 (t, 8H, NCH_2), 1.83 (s, 24H, CH_3). UV-vis (DMSO) λ_{max} /nm (log ε) 365 (4.2), 632 (4.0), 697 (4.4). MALDI-TOFMS: Calc. *m/z*: 969,2 Found 954.4 $[M\text{-}CH_3]^+$, 952.4 $[M\text{-}OH]^+$, 909.01$[M\text{-}4CH_3]^+$. Calc. for $C_{48}H_{53}AlN_{12}OS_4$: C, 59.48; H, 5.51; N, 17.34; S, 13.23. Found: C, 59.34; H, 5.43; N, 17.23; S, 13.16.

2.4.4. Quaternized 2,(3)-tetra [2-(dimethylamino) ethanethio substituted Mg (II) and Al (III) complexes (1a) and (2a) (Scheme 3.2)

Complex **1** (0.1 g, 0.1 mmol) or **2** (0.1 g, 0.1 mmol) was heated gently in chloroform (2, 5 mL) and an excess of CH_3I which was added dropwise. The reaction mixture was heated under reflux for 3 h, cooled to room temperature

and the precipitated product collected by centrifugation and washed several times with hot chloroform.

Compound 1a

Yield: 0.05g (52%); IR, ν_{max}/cm: 3003 (Ar-CH), 2850 (Aliph-CH), 1598, 1472 (C=C), 1368, 1161, 951. ^{1}H NMR (DMSO-d_6): δ ppm 9.61-7.78 (m, 12H, Ar-H), 4.06 (t, 8H,SCH_2), 3.88 (t, 8H, NCH_2), 3.37 (s, 36H, CH_3);MALDI-TOFMS:Calc.$[M-4I]^+$ *m/z*:1009.4;Found:1009.2 $[M-4I]^+$. UV-vis (DMSO) λ_{max} /nm (log ε) 362 (4.7), 622(4.4), 693 (5.1). Calc. $C_{52}H_{64}I_4MgN_{12}S_4$; C 41.16, H 4.25, N 11.08, S 8.45; Found: C 40.49, H 4.23, N 10.77, S 7.49.

Compound 2a

Yield: 0.1 g (72%); IR, ν_{max}/cm: 3412 (OH), 2979-2886 (Alph-CH), 1591, 1468 (C=C), 1370, 1065, 963; ^{1}H NMR (DMSO-d_6): 9.25 (s, 12H, H-Ar), 3.95 (t, 8H, S-CH_2), 3.80 (t, 8H, N-CH_2), 3.25 (s, 36H, CH_3); UV-vis (DMSO) λ_{max} /nm (log ε) 363 (4.6), 632 (4.3), 691(5.0). MALDI-TOFMS calc. $[M-4I]^+$ *m/z*: 1029.41 Found: 1065 [M-4I]+2(H_2O)]. Calc. For $C_{52}H_{65}AlI_4N_{12}OS_4$: C 40.63, H 4.26, N 10.94, S 8.34; Found: C 39.69, H 4.53, N 10.78, S 8.23.

2.4.5. 1,8(11),15(18)-tri-(2-mercaptopyridine)23(24)(4(2{2[22 mercaptoethoxy)-ethoxy]ethoxy}ethoxy)phthalocyaninatozinc(II) (ZnPcSH) (3) (Scheme 3.4)

*Compound **3** was synthesized from **10** and **11**.*

(A)1,8(11),15(18)-Tri-(2-mercaptopyridine)-23(24)-(4-(2-{2-[2-(2-hydroxyethoxy)-ethoxy]ethoxy}ethoxy) phthalocyaninato zinc(II) (10) (Scheme 3.4).

A mixture of 4-(2-{2-[2-(2-hydroxyethoxy)ethoxy]ethoxy}-ethoxy)phthalonitrile (**8**) (100 mg, 0.31 mmol), 3-(2 mercaptopyridine) phthalonitrile (**9**) (222.2 mg, 0.94 mmol), DBU (0.1 mL, 0.63 mmol) and $Zn(OAc)_2$ (114.4 mg, 0.63 mmol) was refluxed in dry pentanol (3 mL) for 24 h under argon atmosphere. Then, the reaction mixture was cooled to room temperature and poured into n-hexane. The green solid product was precipitated and collected by filtration. Crude product (**10**) was purified over a silica gel column using firstly 25:1 and then 10:1 dichloromethane: ethanol solvent mixture as eluent. Yield: 50 mg (15%). IR [(ATR) υ_{max}/cm^{-1}]: 3400 (O-H), 3053 (Ar C-H), 2921-2864 (C-H), 1607 (C=N), 1571 (C=C), 1482, 1448, 1418, 1386, 1331, 1315, 1240, 1095(C-O-C), 962, 896, 731. UV–Vis (DMSO): λ_{max} nm (log ε) 693 (4.81), 624 (4.14), 346 (4.43). ^{1}H NMR (500 MHz, DMSO-d_6): δ, ppm= 8.72-7.01 (m, 24H, Pc-H and Pyridyl-H), 4.22-3.12 (m, 16H, CH_2). Calc. for $C_{55}H_{41}N_{11}O_5S_3Zn$: C 60.19; H 3.77; N 14.04; Found: C 60.42; H 3.81; N 14.20. MS (MALDI-TOF), m/z (%): Calc. 1097.59, Found 1098.42 $[M+H]^+$ (100).

(B)1,8(11),15(18)-Tri-(2-mercaptopyridine)-23(24)(4-(2-{2-[2-(2-methanesulfonylethoxy)-ethoxy]ethoxy}ethoxy)phthalocyaninato zinc(II) (11) (Scheme 3.4).

Compound **10** (30 mg, 0.027 mmol) was dissolved in dichloromethane (10 mL) in the presence of triethylamine (20 drops, excess) and cooled down to ~0°C in ice bath. Methane sulfonyl chloride (10 drops, excess) was added drop-wise to the solution. The mixture was allowed to warm to room temperature and stirred for 30 min. The reaction was monitored by thin-layer chromatography (TLC) using 25:1 dichloromethane: ethanol solvent mixture as eluent. When compound **10** was completely consumed, the product was extracted with water/dichloromethane phase and was dried with anhydrous sodium sulphate. Dichloromethane was removed and crude product (**11**) was purified by preparative TLC (silica gel) using 25:1 dichloromethane: ethanol solvent system as eluent. Yield: 30 mg (94%). IR [(ATR) υ_{max}/cm^{-1}]: 3061 (Ar C-H), 2919 -2851 (C-H), 1608 (C=N), 1571 (C=C), 1449, 1417, 1386, 1329, 1238, 1172 (S=O), 1096 (C-O-C), 963, 896, 804, 758, 740. UV–Vis (DMSO): λ_{max} nm (log ε) 693 (5.14), 630 (4.61), 343 (4.82). ^{1}H NMR (500 MHz, DMSO-d_6): δ, ppm= 8.89-6.99 (m, 24H, Pc-H and Pyridyl-H), 4.55-3.37 (m, 16H, CH_2), 3.15 (s, 3H, CH_3). Calc. for $C_{56}H_{43}N_{11}O_7S_4Zn$: C 57.21; H 3.69; N 13.11; Found: C 57.54; H 3.88; N 13.45. MS (MALDI-TOF), m/z (%): Calc. 1175.68, Found 1176.97 $[M+H]^+$ (100).

(C) Compound (3)

Tetrahydrofuran (THF) (10 mL) and ethanol (3 mL) mixture was deoxygenated by sonication for 30 min using ultrasonic bath. Compound **11** (20 mg, 0.018 mmol) was dissolved in this previously prepared solvent mixture and the solution was refluxed under argon atmosphere in the dark. Then, thiourea (10 mg, excess) was added during reflux and the reaction was followed by TLC. After the starting compound **11** was consumed; argon was bubbled through the reaction mixture. Aqueous sodium hydroxide solution (20%, 4 mL) which was previously deoxygenated by sonication for 30 min was added and the mixture was refluxed for 2 h. When the reaction was complete (monitoring by TLC), the resulting mixture was poured into a mixture of dilute hydrochloride acid and ice and extracted with dichloromethane. The organic phase was extracted and dried with anhydrous sodium sulphate. Crude product (**3**, **ZnPcSH**) was purified by preparative TLC (silica gel) using 10:1 dichloromethane: ethanol solvent system as eluent Yield: 12 mg (63%). IR [(ATR) υ_{max}/cm^{-1}]: 3079 (Ar C-H), 2919-2867 (C-H), 1603 (C=N), 1524 (C=C), 1481, 1449, 1386, 1323, 1279, 1238, 1109, 1081, 944, 895, 762, 741. UV–Vis (DMSO): λ_{max} nm (log ε) 693 (4.53), 643 (4.16), 343 (4.27). ^{1}H NMR (500 MHz, DMSO-d_6): δ, ppm= 9.48-7.48 (m, 24H, Pc-H and Pyridyl-H), 7.09 (s, 1H, S–H), 4.65-3.28 (m, 16H, CH_2). Calc. for $C_{55}H_{41}N_{11}O_4S_4Zn$: C 59.32; H 3.71; N 13.83; Found: C 59.61; H 3.94; N 13.78. MS (ES-MS), m/z (%): Calc. 1113.66, Found 1136.17 $[M+Na]^+$ (100).

2.4.6. Synthesis of zinc tetra (4-(thiamine) phthalocyanine (ZnTTAPc) (4) (Scheme 3.3).

A mixture of **6** (0.3 g, 0.18 mmol), anhydrous zinc chloride (0.0061 g, 0.045 mmol) and DBU (1 mL, 6.3 mmol) was refluxed in dimethyl amino ethanol for 8 hr. The product was cooled to room temperature and precipitated with ethanol. After filtration the product was washed repeatedly with ethanol. The product was purified in a reverse phase column using a mixture of methanol and acetonitrile (1:2) as an eluent. Yield: 2.9g (58 %). IR: 3492 (N-H), 3051, 3079 (Ar-CH) 2958, 2921(Alph-CH), 1610 (N-H bending), 1226 (C-O-C) 1576, (C=C). ^{1}H NMR (DMF-D_7): 9.53-9.89 (m, 12H, Ar-H), 8.41 (s, 4H, S-CH-N), 7.27 (s, 4H, CH=N), 5.76 (s, 8H, CH_2-N), 3.66 (s, 8H, NH_2), 3.29 (t, 8H, O-CH_2), 2.90(t, 8H,-CH_2), 2.47 (t, 12H, CH_3), 2.21 (s, 12H, CH_3), MALDI- TOFMS. Calc. m/z 1631.27, Found: $[M]^+$:1630.51.UV-Vis (DMF) λmax/nm (log ε)358 (4.6), 617 (4.2), 686 (4.97). *Anal.* Calc for $C_{80}H_{76}N_{24}O_4S_4Zn$: C 58.89, H 4.69, N 20.61, S 7.86; Found: C 58.49, H 4.66, N 21.09, S 7.87.

2.5. Synthesis of phthalocyanine-gold nanoparticle conjugates

2.5.1. Synthesis of complex 1a or 2a- citrate-AuNS

The aqueous solution of the colloidal citrate capped gold nanoparticles was added into an equal amount of DMSO and mixed at room temperature for 2 min. A solvent mixture containing some DMSO was needed in order to avoid aggregation of Pcs alone. A solution of complex **1a** or **2a** (3 mg, 0.002 mmol) in

DMSO (5 mL) was mixed with 20 mL of the gold nanoparticle solution and stirred for 24 hr (at room temperature) to allow ligand exchange of the citrate for the phthalocyanines to take place. The conjugated system was purified in a size exclusion column in Bio-Beads (Bio-Beads S-X1 from Bio-Rad) using DMSO as an eluent.

2.5.2. Synthesis of ZnPcSH (3) -TOABr AuNS

A mixture of **ZnPcSH** (**3**) (3 mg, 0.003 mmol) and TOABr-AuNS gold particles in toluene (1 mL) was stirred for 24 hr for the ligand exchange to take place. After this time, the reaction mixture was diluted with toluene, and the unreacted Pc was separated in a size-exclusion column (Bio-Beads S-X1 from Bio-Rad) using toluene as an eluent.

2.5.3. Synthesis of complex 2a-AuNR (3.2) Complex 2a-AuBP and complex 2a-AuNS (all capped with CTAB)

Quaternized 2,(3)-Tetra [2-(dimethylamino) ethanethio substituted Al (III) complex ***(2a)*** (10 mg, 0.0065 mmol) was dissolved in DMSO (5 mL) to make a phthalocyanine solution. A solution of each of the differently shaped gold nanoparticles (10 mL) was mixed with of complex **2a** in DMSO and stirred for 24 hr at room temperature. The conjugates were purified in a size exclusion column in Bio-Beads using DMSO as an eluent. The conjugates are represented as **2a – CTAB-AuNS**, **2a - AuNR (3.2)** and **2a - AuBP**.

2.5.4. Conjugation of ZnTTAPc (4) to nanorods with different aspect ratio (AuNS (2.0), (4.7) and (7.1)

Before use for coordination to **ZnTTAPc** (**4**), AuNRs solution was centrifuged for 5 min to remove excess CTAB. The clear liquid was discarded and the resulting gold pellet was dissolved in 1 mL distilled water. The solution of gold nanoparticles (1 mL) of diferent aspect ratio was mixed with 1 mL aqueous solution (pH 9) of **ZnTTAPc** (**4**) (2 mg/mL) and this mixture was stirred for about 5 min then further diluted with 3 mL distilled water and stirred overnight. The conjugate was purified in a size exclusion column in Bio-Beads using pH 9 buffer as an eluting solvent.

2.6. Physical characterization of AuNPs

Physical characterization of the nanoparticles provides useful information about the loading of phthalocyanines onto gold nanoparticles in the conjugates.

Methods reported in literature [**131, 132**] were employed in this section.

Total number of Au atoms per AuNP. The total number of gold atoms per nanoparticle was calculated using equation **2.1**.

$$V_{(NP)} = NV_{(atom)} \qquad (2.1)$$

where $V_{(NP)}$ in the volume of the AuNP (sphere or rod) and $V_{(atom)}$ is the volume of the Au atom. The volumes of a sphere (V (sphere)) and nanorod (V(rod)) are given by equations **2.2** and **2.3**, respectively and employed in equation **2.1**.

$V(\text{sphere}) = 4/3\pi r^3$ (**2.2**)

$V(\text{rod}) = 4/3\pi r^3+\pi r^2(l-2r)$ (**2.3**)

where r is the radius and l is the length (the latter for the nanorod only).

Surface area of AuNPs. The surface area of a rod may be determined using equation **2.4** [**133**].

$SA\ \textbf{(rod)} = 2\pi r^2 + 2\pi rl$ (**2.4**)

where r and l are radius and length of a rod respectively. The usual equation ($4\pi r^2$) was employed for the calculation of the surface area of the sphere.

Number of surface Au atoms per AuNP. The number of surface Au atoms N(surface) may be determined by dividing the surface area of the nanoparticle by the cross- sectional area of an atom, equations **2.5** and **2.6** [**131**].

$N_{\text{surface (sphere)}} = 4\pi\ (r_{NP})^2\ /\ \pi\ (r_{atom})^2$ (**2.5**)

$N_{\text{surface (rods)}} = 2\pi r^2 + 2\pi rl/\ \pi\ (r_{atom})^2$ (**2.6**)

where r_{atom} is the radius of the atom.

Extinction coefficients of AuNPs. Extinction coefficients of the AuNRs were determined using established methods [**134,135**] and Beer's law, **equation 2.7**

$A = \varepsilon lc$ (**2.7**)

where A is absorbance, ε is the extinction coefficient ($M^{-1}cm^{-1}$), l is the path

length (cm), and c is the AuNRs concentration (M). ICP was used to determine the total number of gold atoms/mL, which was converted to moles per L using Avogadro's constant.

The total number gold nanoparticles was estimated using **equation (2.8)** [**131**].

$$N_{(NP)} = N_{(Au\ atoms)} / N_{(total)} \quad (\mathbf{2.8})$$

The number of Pc molecules was obtained using the Beer's law (**equation 2.7**) and the Q band absorption maximum of the phthalocyanines, assuming the extinction coefficient does not change upon conjugation. The number of Pc molecules on the gold nanoparticles was then estimated from the ratio of the number of Pc molecules to the number of AuNPs.

2.7. Photophysical and photochemical methods

2.7.1. Fluorescence quantum yields

The fluorescence quantum yields of the Pcs and Pc-AuNPs conjugates were determined in either DMF, DMSO, pH9 buffer or a comparative method, **Equation1.1**. Unsubstituted ZnPc in DMF (Φ_F= 0.30) [**136**], DMSO (Φ_F = 0.20 [**81**] and AlPcSmix in aqueous solutions (Φ_F= 0.44[**137**] were employed as standards. Both sample and standard were excited at the same wavelength. The absorbances of the solutions at the excitation source were about 0.05 to avoid any filter effects.

2.7.2. Triplet quantum yields and lifetimes

The decay kinetics of the triplet absorption of the phthalocyanines and phthalocyanine-gold nanoparticle conjugates were recorded using the laser flash photolysis set-up, **Figure 2.2**. The absorbances of the phthalocyanines and phthalocyanine-gold nanoparticle conjugates were adjusted to be approximately 1.5, respectively at their Q-band maximum. After introducing the solution into a 1 cm quartz cell, argon was bubbled through the solution to remove dissolved oxygen. The triplet quantum yields were determined using **Equation 1.3**. Unsubstituted ZnPc in DMF (Φ_T = 0.56) [**138**], DMSO (Φ_T = 0.65 [**84**] and AlPcSmix in aqueous solutions (Φ_F=0.44), [**137**] were employed as standards. Triplet lifetimes were determined from the kinetic data obtained using Origin Pro 8 software.

2.7.3. Singlet oxygen quantum yields

A chemical method was used for the determination of Φ_Δ of the phthalocyanines and phthalocyanine-gold nanoparticle conjugates in solution. The experiments were conducted in air with 1.5 ml of each Pc or Pc-AuNP solution with approximate absorbance of 1 at the Q band mixed with an equal volume of a DPBF solution with approximate absorbance of 2 at 416 nm. The resulting solution was irradiated using the set-up shown in **Figure 2.3** and the degradation of the DPBF was monitored by recording the UV-Vis spectra of the sample solution at time intervals. The Φ_Δ values were determined using **Equation 1.5** and employing ZnPc in DMSO = 0.67 [**139**] as the standard.

The determination of Φ_Δ in DMF and aqueous solutions was also achieved by employing an optical method. The optical method involves the observation of the fluorescence kinetic decay of the singlet oxygen generated at 1270 nm in air using the method described in (**Section 1.2.6.3**). Sodium azide (NaN_3) was used as singlet oxygen quencher. The Φ_Δ values were then determined using **Equation. 1.7.** AlPcSmix in aqueous solution (Φ_Δ = 0.42) [**140**] and ZnPc in DMF (Φ_Δ = 0.56) [**141**] were employed as standards.

2.8. Photoinactivation studies

***2a**, **2a**-AuNRs (**3.2**) and **2a**-AuBPs were employed for cell studies. **2a** is a cationic and water soluble molecule hence, it is suitable for PACT, as an example representing all water soluble Pcs (**1a**, **4**).*

2.8.1. Preparation of microorganisms

C. albicans and *E. coli* cultures were grown on a nutrient agar plate prepared according to the manufacturer's specifications of striking to obtain individual colony. The colony was then inoculated into nutrient broth and then placed on a rotary shaker (~ 200 rpm) overnight at 30 and 37 °C for *C. albicans* and *E. coli,* respectively. Aliquots of the culture were aseptically transferred to 4 mL of fresh broth and incubated again to mid logarithmic phase (OD 620 nm ≈ 0.6). The bacteria cultures in the logarithmic phase of growth were harvested by the removal of broth culture using centrifugation (3500 rpm for 5 min),

washed once with PBS (10 mM) and re-suspended in 4 mL PBS. Then, the bacteria culture was diluted to 1/1000 in PBS. The microorganisms in PBS were serially diluted and plated, then the colony forming units were counted. The initial colony forming units per mL (CFU/mL) were calculated using **equation 2.9** and were found to be to ~ 10^7 and 10^8 (CFU)/mL) for *E. coli* and *C. albicans,* respectively.

CFU/mL = number of colonies per mL plated/total dilution factor (**2.9**)

E. coli was also prepared using the same processure as above.

2.8.2. Photo-irradiation conditions

The power outputs of 25.25 mW (used for *E. coli*) or 27.75 mW (used for *C. albicans*) were measured with a POWER MAX 5100 (Molelectron detector incorporated) power meter. Illumination area was 0.3 cm^2. Light intensities at 691 nm were 2.93 x 10^{17} and 3.22 x 10^{17} photons cm^{-2} s^{-1} for *E. Coli* and *C. albicans* respectively in PACT studies. The set-up used for photoinactivation is shown in **Figure 2.2**.

2.8.3. In vitro photoinactivation experiments

Preliminary experiments were performed in order to determine the appropriate light dose and photosensitizer concentration. **Figure 2.4** shows the set-up for antimicrobial studies. Photodynamic inactivation studies were conducted

following the methods used by Dupoy *et al* and Mantareva *et al* [**142,143**]. Briefly, *C. albicans* cells (10^8 CFU/mL) were incubated with **2a** or **2a**-AuNPs at a concentration of 35 μM. The mixture was incubated in an oven equipped with a shaker for 30 min in the dark at 30 ^oC. Then half (2 mL) of the samples containing **2a** or **2a**-AuNPs and cells was irradiated at the Q-band maximum of the photosensitizers in quartz cell, using the set-up described above at different time intervals, while the other half was kept in the dark for dark toxicity studies. After irradiation, 100 μL samples were serially diluted and plated on agar plates [**143, 144**]. Similar procedure was used for the conjugates. The concentration of the complex **2a** in the **2a**-AuNPs was adjusted by absorbance of the Q-band. Thus the Q band absorbances were the same for the Pc alone and when conjugated to AuNPs. Photoinactivation of *E. coli* containing an initial population of $\mathbf{10^7}$ (CFU/mL) was carried out using similar procedures but for these studies the concentration of the complex **2a** was reduced to 20 μM and the samples was incubated at 37 °C.

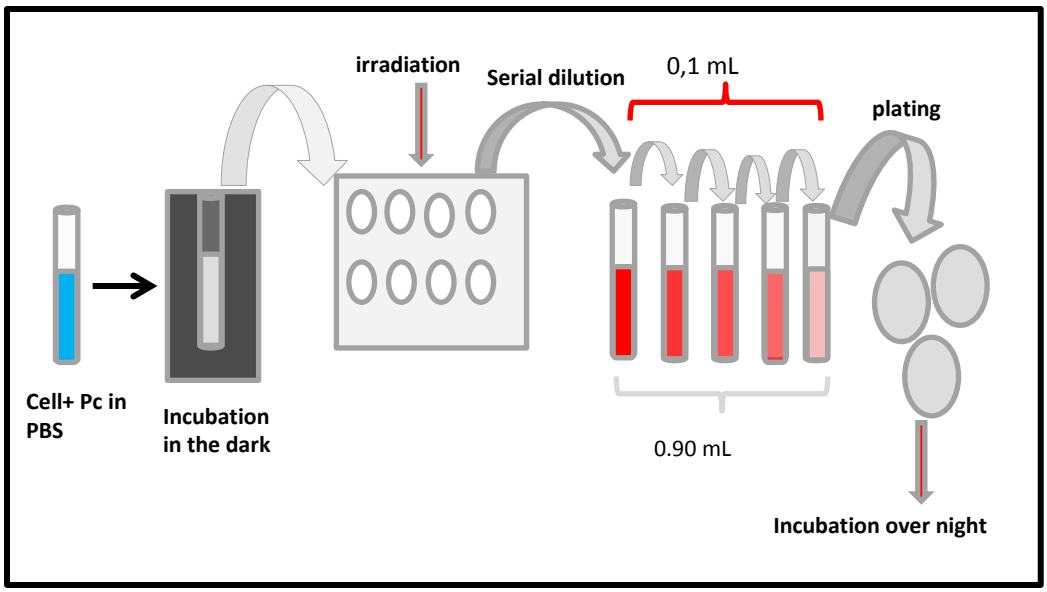

Figure 2.4: Schematic illustration of an in vitro photoinactivation experiment with Pc.

Results and Discussion

3. Synthesis and characterization

4. Photophysical and Photochemical properties

5. Photoinactivation studies

6. Fe Protoporphyrin IX binding to metallothionein

Publications

The results discussed in the following chapters have been presented in the articles below that have been published or submitted for publication to peer-reviewed journals. These articles have not been referenced in this thesis.

1. **Thandekile P. Mthethwa**, Yasin Arslanoglu , Edith Antunes, Tebello Nyokong; Photophysical behaviour of cationic 2-(dimethylamino) ethanethio tetrasubtituted phthalocyanine complexes in the presence of gold nanoparticles, *Polyhedron*, 38 (2012), 169-177.

2. **Thandekile P. Mthethwa**, Sinem Tuncel, Mahmut Durmuş and Tebello Nyokong, Photophysical and photochemical properties of a novel thiol terminated low symmetry zinc phthalocyanine complex and its gold nanoparticles conjugate, *Dalton Tans*. 42 (2013), 4922-4930.

3. **T. P. Mthethwa,** Tebello Nyokong, Fluorescence behaviour and singlet oxygen generating abilities of aluminium phthalocyanine in the presence of anisotropic gold nanoparticles, Journal of Luminescence 157, (2014), 207-214.

4. **Thandekile Mthethwa,** E. Antunes and T. Nyokong, Photophysical properties of a new water soluble tetra (4-(thiamine) substituted zincphthalocyanine conjugated to gold nanorods of different aspect ratios, *Dalton Trans.,* 43, (2014), 8230-8240.

5. **Thandekile Mthethwa** and Tebello Nyokong**,** Photo inactivation of *Candida Albicans* and *Escherichia Coli* using aluminium (III) phthalocyanine on gold nanoparticles, *Photochem. Photobio. Sci.,* Accepted with revision.

Chapter 3
Synthesis and Characterization

This chapter reports on the syntheses and characterization of phthalocyanines and phthalocyanine-gold nanoparticle conjugates employed in this work.

3.1. Gold nanoparticles-phthalocyanine conjugates

All the conjugates synthesized and studied in this work are summarized in **Table 3.1**. Gold is known to form strong bonds with nitrogen and sulfur. Metallophthalocyanines (MPcs) reported in this work are expected to form nitrogen-gold or sulfur-gold bonds with the gold nanoparticles, since they contain sulfur-containing groups and/or nitrogen-containing groups as substituents on the phthalocyanine ring. Complexes **1a** and **2a** both have sulfur groups on the periphery of the phthalocyanine ring, thus phthalocyanine complexes are attached to the AuNPs surface by Au–S bond through formation of self-assembly monolayers.

Complex **ZnPcSH (3)** is most likely to attach to the AuNPs surface via Au-S bond due to the SH group terminating the ethoxy ligand. However, it is possible that the sulfur atoms of the mercapto group of **3** also coordinate to the AuNPs. It is expected that the stronger bond will be that of SH group, resulting in a perpendicular arrangement on the AuNPs. Complex **ZnTTAPc (4)** contains sulfur on the thiazole group and the amine from its pyrimidine group of the thiamine. This molecule could attach to AuNP through nitrogen or sulfur.

Notes:

- Water soluble complexes **1a** and **2a** were conjugated to citrate capped spherical AuNPs (AuNS) in order to study the effect of central metal (Mg vs Al). Citrate capping allows AuNS to be water soluble.
- Complex **2a** was further conjugated to different shaped AuNPs. CTAB was employed as a capping agent, since it is a shape directing agent and was used for the formation of AuBP and AuNR (**3.2**). For comparison CTAB was also used for the synthesis of AuNS. The effect of shape (e.g. AuNR and AuBPs) was investigated in comparison with spherical AuNP.
- The non-water soluble complex **3** was conjugated to TOABr-AuNS. TOABr is an organic soluble phase transfer capping agent which makes AuNPs organic soluble and was required since the complex **3** is only soluble in organic solvents.
- In order to check the effect of size of the AuNRs complex **4** was conjugated to AuNRs with different aspect ratio.

Table 3.1: Phthalocyanine-gold nanoparticles conjugates studied in this work.

Complex	**AuNPs**
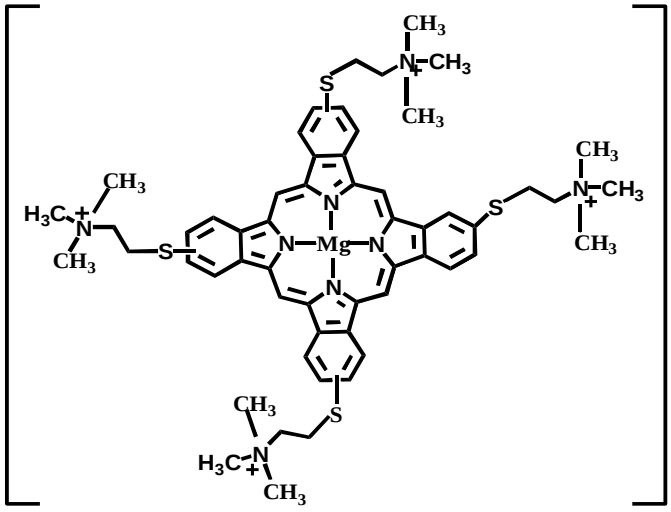 **4I⁻** **1a**	**Citrate-AuNS**
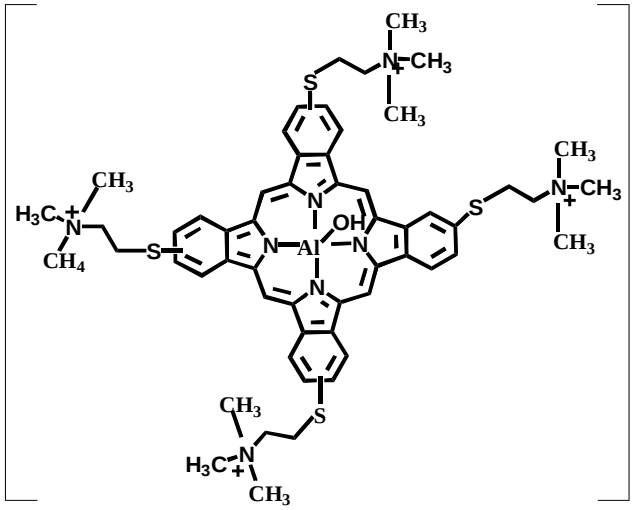 **4I⁻** **2a**	**Citrate-AuNS** **CTAB-AuNS** **CTAB-AuNR (3.2)** **CTAB-AuBPs**

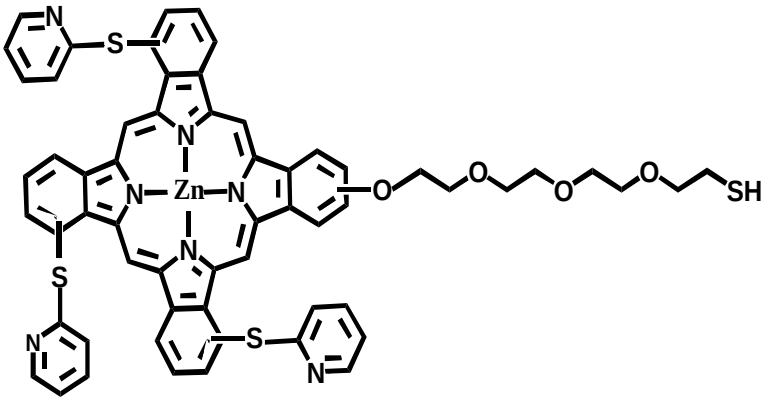 **3**	**TOABr-AuNS**
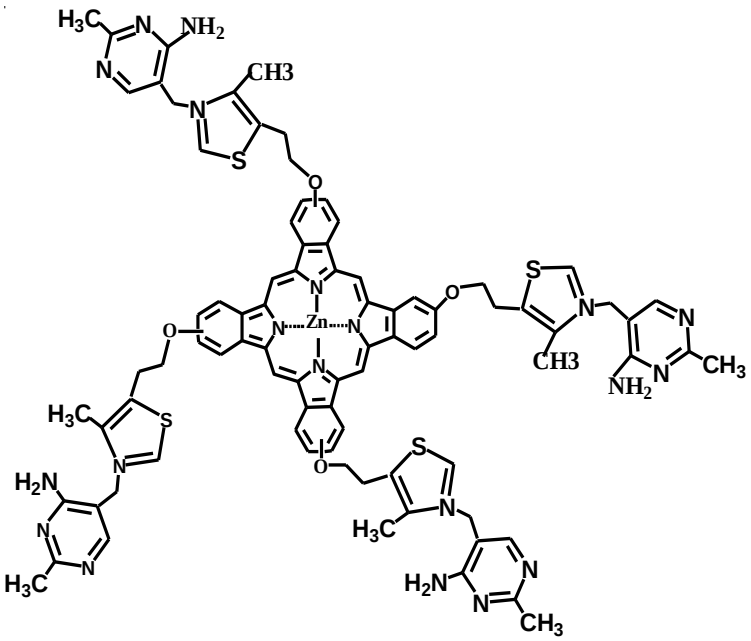 **4**	**CTAB**-AuNS, **CTAB**-AuNR (**2.0**), (**4.7**) and (**7.1**)

3.2. Synthesis and characterization of phthalocyanines

3.2.1. Thiamine phthalonitrile (6)

Thiamine substituted phthalonitrile (**6**)(**Scheme 3.1**) was characterized using IR, elemental analysis and ^{1}H NMR spectroscopies. IR confirmed the presence of the N-H and the aliphatic CH stretches which shows that the successful substitution of the phthalonitrile with thiamine. ^{1}H NMR of the thiamine phthalonitrile confirmed all the aromatic and aliphatic protons as expected. The two protons from amino group were around 4.33.

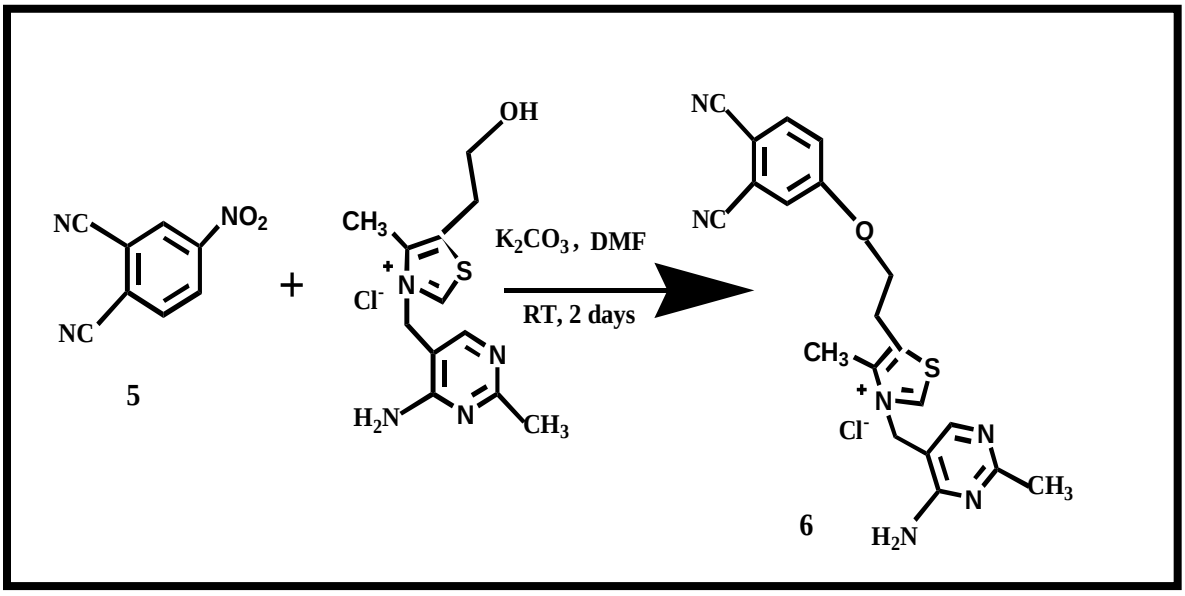

Scheme 3.1: Synthesis of a thiamine substituted phthalonitrile.

3.2.2. Tetra-substituted symmetrical phthalocyanines (1, 2, 4)

The synthetic route used to obtain *(3)-tetra- [2-(dimethylamino) ethanethio) phthalocyanino magnesium (II)* (**1**), *2,(3)Tetra [2-(dimethylamino) ethanethio)phthalocyanito aluminium (III) hydroxide* **(2)**, *and their quaternized derivatives (complexes **1a** and **2a**)* is shown in **Scheme 3.2**. The synthesis procedure to thiamine substituted Pc (**ZnTTAPc**) (**4**) is shown in **Scheme 3.3**.

Characterization of the compounds was achieved using infra-red (IR), UV-Vis, NMR and mass spectroscopies, as well as elemental analysis. ^{1}H NMR showed all the protons in their correct positions. The absence of the sharp C≡N vibration (~2230 cm^{-1}) in the IR spectra of phthalocyanine complexes confirmed phthalonitrile cyclization. All complexes gave satisfactory characterization as shown in the experimental section. The IR spectrum confirmed the presence of hydroxide in the axial position for **2** (or **2a**) with an OH vibration being observed at 3288 cm^{-1} for **2** and 3412 cm^{-1} for **2a**. Elemental analysis results were consistent with the predicted structures with percentage carbon values less than 1%. Elemental analysis of thiamine substituted zinc phthalocyanine confirmed the absence of chloride and hence the non-ionic nature of the molecule following an extensive purification procedure.

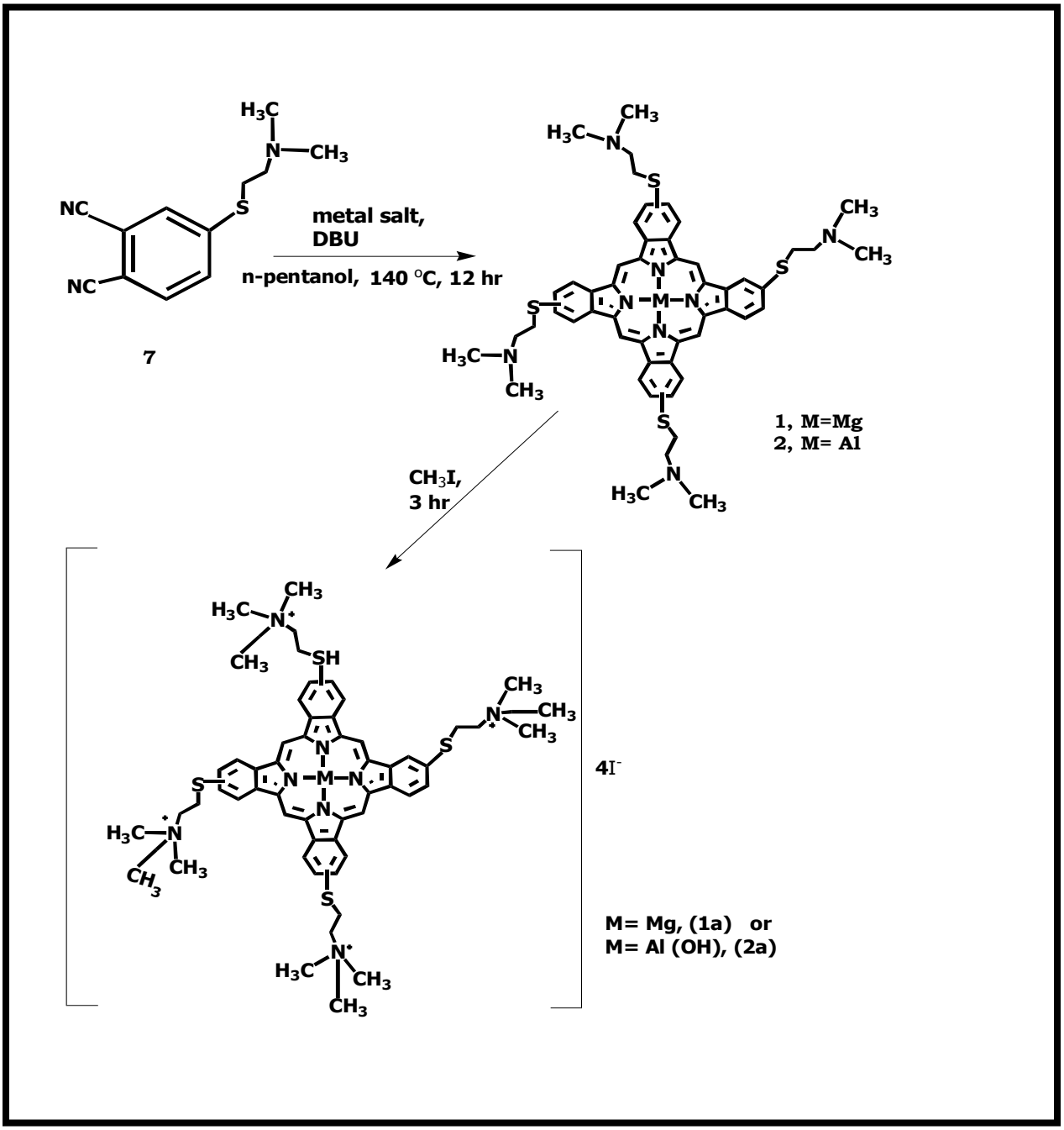

Scheme 3.2: Synthesis route to phthalocyanines **1**, **2**, **1a** and **2a**.

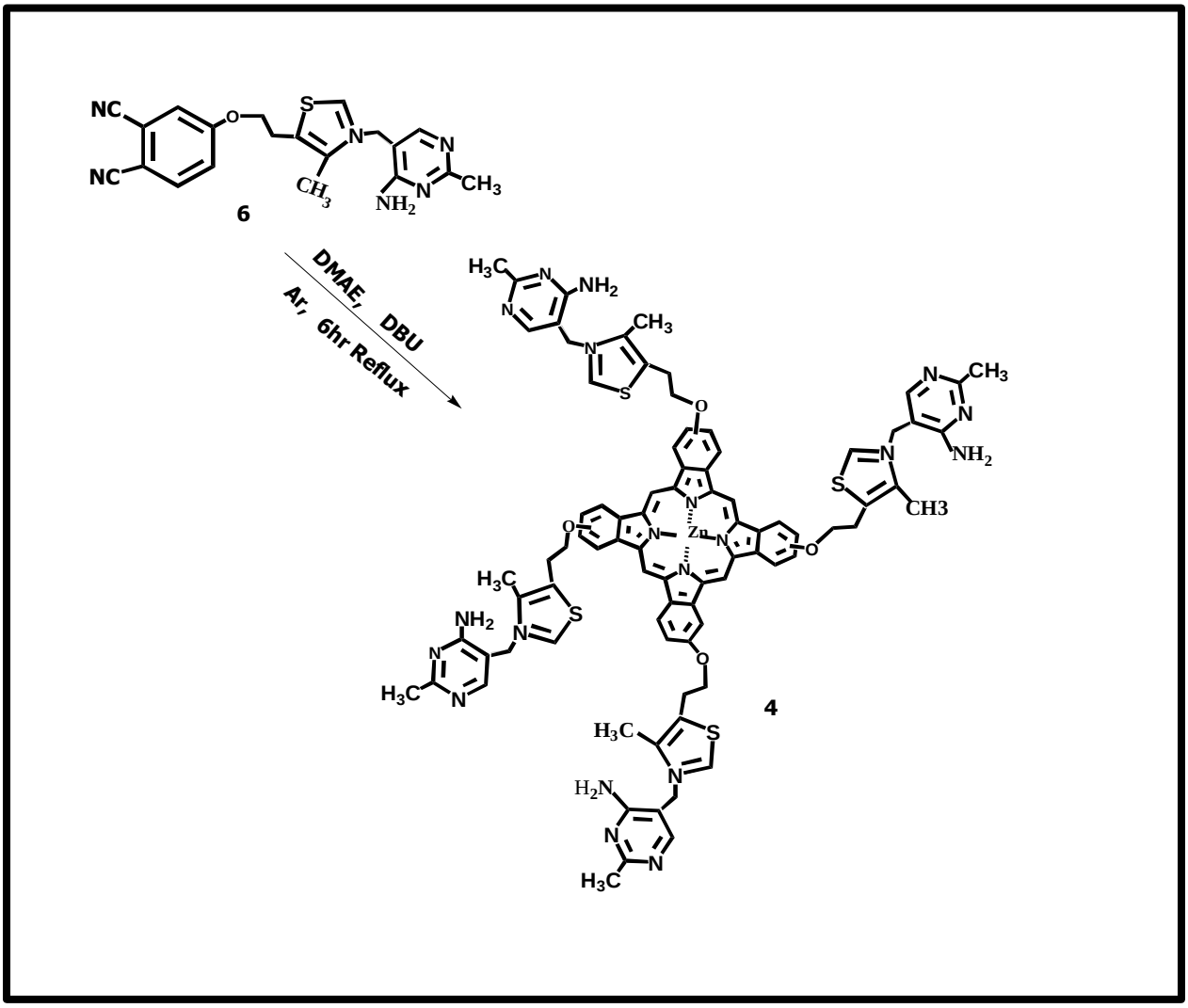

Scheme 3.3: Synthesis route to thiamine substituted phthalocyanine (**ZnTTAPc**) (**4**).

3.2.3. 1,8(11),15(18)-tri-(2-mercaptopyridine)-23(24)-(4-(2-{2-[2-(2-mercaptoethoxy)- ethoxy]ethoxy}ethoxy)phthalocyaninato zinc(II) (3) (ZnPcSH) (Scheme 3.4) (3)

The synthesis of unsymmetrical phthalocyanines is complicated compared to symmetrically substituted Pcs as they often require extensive purification methods to obtain the desired product. **Scheme 3.4** shows the chemical structure and synthetic route of compound **3**. Statistical condensation method of two phthalonitriles **8** and **9** was employed in this work. The synthesis of complex **3** starts with the synthesis of **10**. The terminal hydroxyl group on complex **10** was converted into its mesylate counterpart using a triethylamine (TEA) followed by the addition of methanesulfonyl chloride to give the substituted phthalocyanine **11**. Finally, the terminal thiol functional group was obtained under an inert atmosphere in the absence of light, in a previously degassed THF/ethanol solvent mixture containing complex **11**. The resulting product was then hydrolysed using 20% NaOH (also previously degassed). The inert atmosphere inhibits the formation of disulfides via aerobic oxidations and ensures the formation of complex **3**.

The ^{1}H NMR spectrum of the target complex **3** showed aromatic protons between 7.48 and 9.48 (integrating for 24 protons), the CH_2 groups between 3.28 and 4.65 (integrating for 16 protons) and the SH group at 7.09 integrating for 1 NH proton). The mass spectrum of the complex showed a molecular ion peak at 1136.17 amu as M + Na peak.

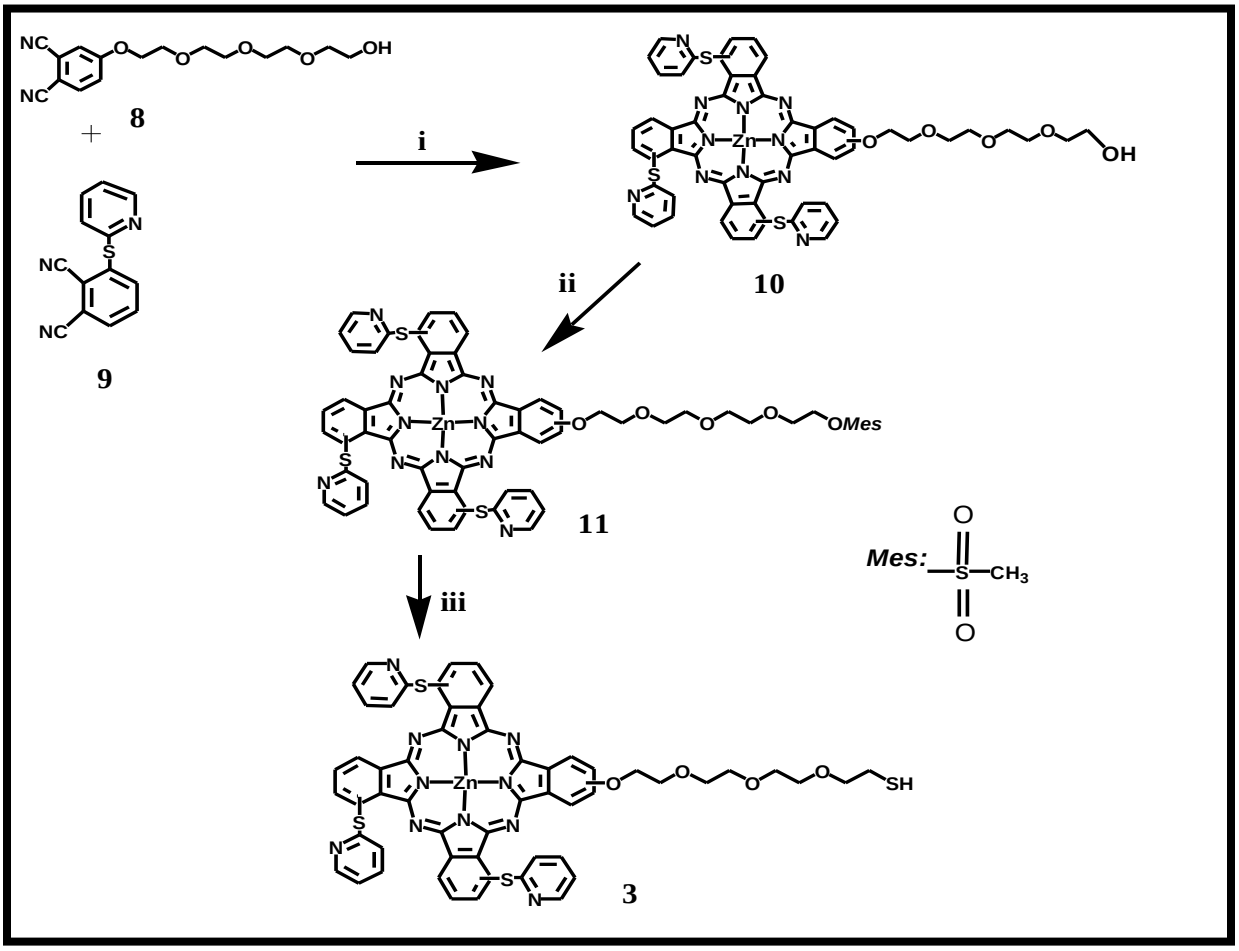

Scheme 3.4: Synthesis route to phthalocyanine **3** (**ZnPcSH**). **i***:* $Zn(OAc)_2$, pentanol, DBU; **ii**: Methane sulfonyl chloride, triethylamine, dichloromethane; **iii** *1*) Thiourea, ethanol, THF, *2*), NaOH.

3.3. Ground state absorption and fluorescence spectra of the phthalocyanines

(***ZnTTAPc***) (***4***) *was studied in DMF and in aqueous solution at pH 9 because the triplet and singlet oxygen signals in DMSO were poor compared to DMF. Complexes* ***1****,* ***2****, and* ***3*** *were studied in DMSO. Complexes* ***1a*** *and* ***2a*** *were studied in DMSO and water.*

The absorption spectrum of complex **1** shows the Q-band at 693 nm (**Table 3.2** and **Figure 3.1**), whereas for complex **2** the Q-band was observed at 697 nm, **Table 3.2** (**Figure 3.1**) in DMSO. Both samples show a narrow Q band typical of metallated phthalocyanines and both complexes (**1** and **2**) obeyed Beer's law at concentrations below 8.0×10^{-5} M in DMSO.

The quaternized complexes **1a** and **2a** showed a blue shifted Q band, **Figure 3.1**, **Table 3.2** compared to unquaternized derivatives, **1** and **2**, respectively. The blue shift is associated with the engagement of the lone pair of the nitrogen on the ethanethiol chain following quaternization. The nitrogen donates a lone pair of electrons to the Pc resulting in a red shift of the Q-band and once engaged after quaternization a blue shift occur. In DMSO, complexes **1a** and **2a** obeyed Beer's law at concentration below 6.3×10^{-6} M. The absorption spectrum of complex **3, Figure 3.1** shows broadening typical of aggregation with a broad peak near 630 nm and a more intense and sharper peak at 694 nm due to the monomer. However **ZnPcSH (3)** obeys Beer's law at concentrations lower than 2×10^{-6} M in DMSO.

Table 3.2: UV-Vis and fluorescence spectral results of the phthalocyanine complexes.

Complex	Solvent	$\lambda_{Q\ band}$ (nm) (absorption)	λ_{Qband} (nm) (excitation)	$\lambda_{Q\ band}$ (nm) (emission)
1	DMSO	693	691	700
2	DMSO	697	701	707
1a	DMSO	687	688	699
2a	DMSO	691	692	703
1a	H_2O	630, 686	689	702
2a	H_2O	691	693	704
3	DMSO	694	695	708
4	DMF	688	688	699
4	pH 9 buffer	638, 696	696	704
4	pH 9 buffer +Triton X 100	638, 696	696	704

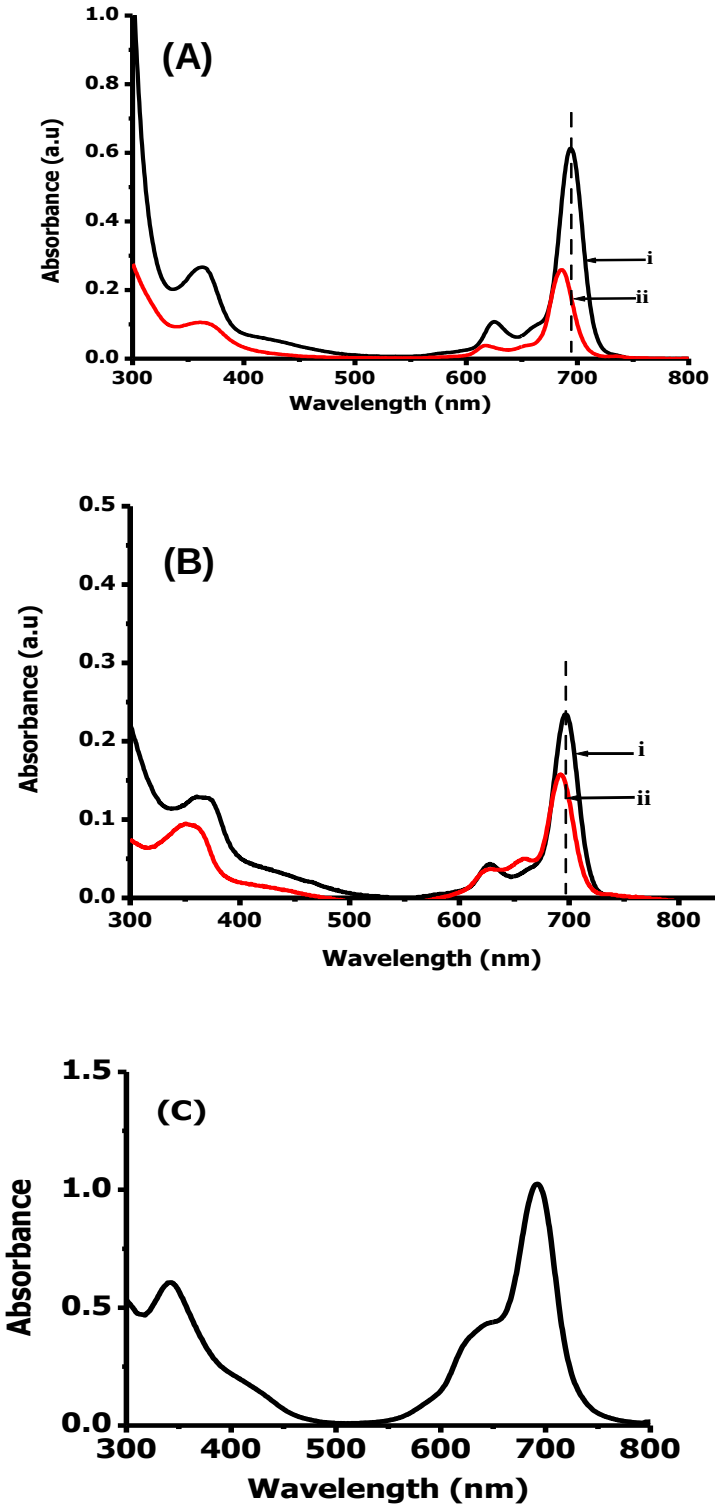

Figure 3.1: Absorption spectra of (A) **1**(i) and **1a** (ii), (B) **2**(i) and **2a** (ii) and (C) **3** in DMSO.

The quartenized complexes **1a** and **2a** were highly soluble in water, however, **1a** in particular showed extensive aggregation, **Figure 3.2(A)**, as judged by the splitting of the Q band showing two bands at 630 nm due to the aggregates and at 686 nm due to the monomer. Complex **2a** containing an axial ligand, shows less aggregation with only some broadening to the blue side of the Q band, **Figure 3.2(B)**. Addition of a surfactant, Triton X 100, could effectively break the aggregates for **1a**, (**Figure 3.2(A)**) while for **2a** an increase in Q band absorption is observed in the presence of Triton X 100, **Figure 3.2(B)**. In DMSO, **Figure 3.1**, a single Q band was observed confirming that the split Q band in water is due to aggregation and not demetalation for **1a**. The UV-Vis spectrum of the **ZnTTAPc** (**4**) shows two absorption peaks at 638 nm and 696 nm due to aggregation in aqueous solutions, **Figure 3.2 (C)** and **Table 3.1**. The blue shifted band at 638 nm is due to the aggregates and the band at 696 nm is the monomer peak. After the addition of Triton X 100 the aggregate peak decreased and the monomer peak intensity increased, but there is still some aggregation.

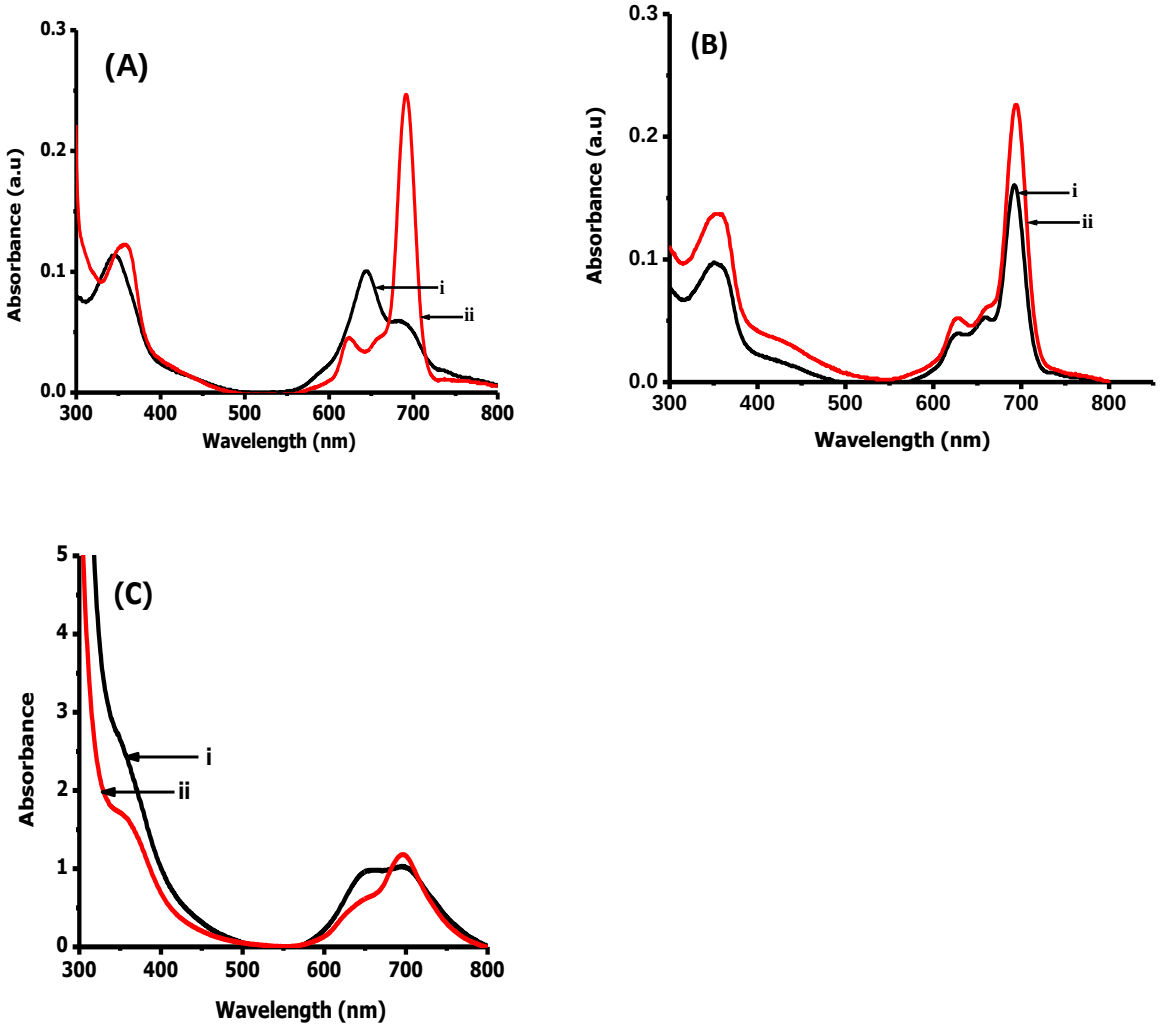

Figure 3.2: Absorption spectra of the complex (A) **1a**, (B) **2a** and (C) **4** in (i) pH9 buffer and (ii) pH9 buffer + Triton X 100.

The ground state absorption and fluorescence properties of all the complexes studied in this work are summarized in **Table 3.2**. The UV-Vis absorption, emission and excitation spectra of complexes **1, 3** in DMSO and **4** in DMF are shown in **Figure 3.3**. The absorption spectra were similar to excitation spectra

and mirror images of the emission spectra for **1** and **4**. Similar behaviour was observed for the quaternized complexes **1a** and **2a** in DMSO (**Figures not shown**). The excitation spectrum is narrower than the absorption spectrum due to aggregation for **3, Figure 3.3** (**B**). For the quaternized complexes (**1a** and **2a**) in aqueous medium, there was a disagreement between absorption and emission spectra due to aggregation, **Figure 3.4 A** and **B** as aggregates quench the fluorescence. The same behaviour was observed for **4** in pH 9 buffer + Triton X 100 (**Figure 3.4** (**C**))

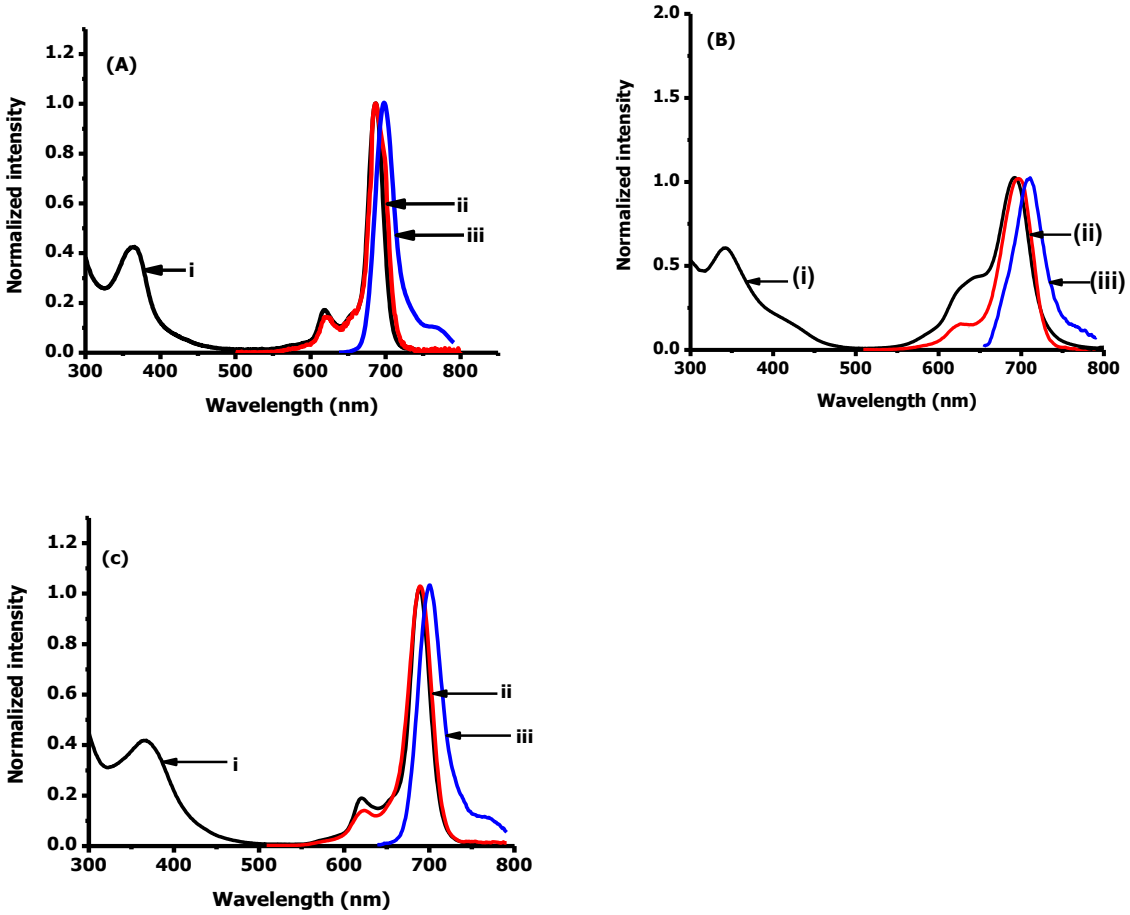

Figure 3.3: (i) Absorption, (ii) excitation and (iii) emission spectra of complexes (A) **1** and (B) **ZnPcSH** (**3**) in DMSO and (C) **ZnTTAPc** (**4**) in DMF.

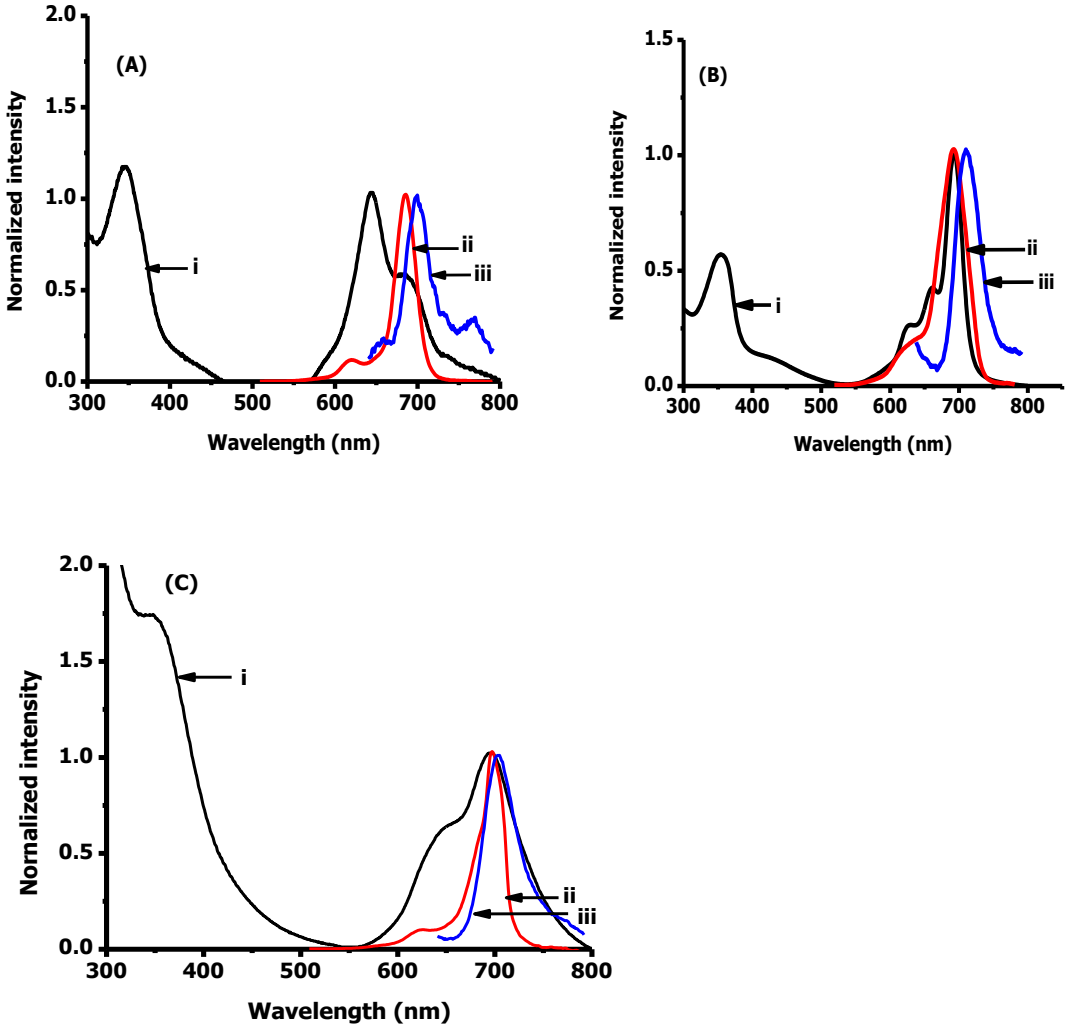

Figure 3.4: (i) Absorption, (ii) excitation and (iii) emission spectra of complexes (A) **1a** in H_2O, (B) **2a** in H_2O and (C) **ZnTTAPc** (**4**) in pH 9 buffer + Triton X.

3.4. XRD and TEM Characterization of metallophthalocyanine-gold conjugates

3.4.1. AuNS conjugates

Table 3.3. *summarizes the sizes of the AuNPs obtained from TEM.*

3.4.1.1. CTAB-AuNS (2a, 4) and Citrate-AuNS (1 a) and (2 a)

Figure 3.5 (**A**) shows well dispersed citrate-AuNS with an average size of 5.2 nm. On conjugation with **1a** or **2a** TEM images show aggregation of spherical particles, **Figure 3.5**(**B and C**). Similar observation has recently been reported for Pc complexes conjugated with AuNPs [**91**]. The average size of the citrate-AuNS in the conjugates was 10.6 nm and 11.5 nm for **1a**-citrate-AuNS and **2a**-citrate-AuNS respectively, **Table 3.3**. CTAB-AuNS size was 5.4 nm and on conjugation to **2a** or **4** the size increased to 11.2 and 5.6 nm, **Table 3.3**.

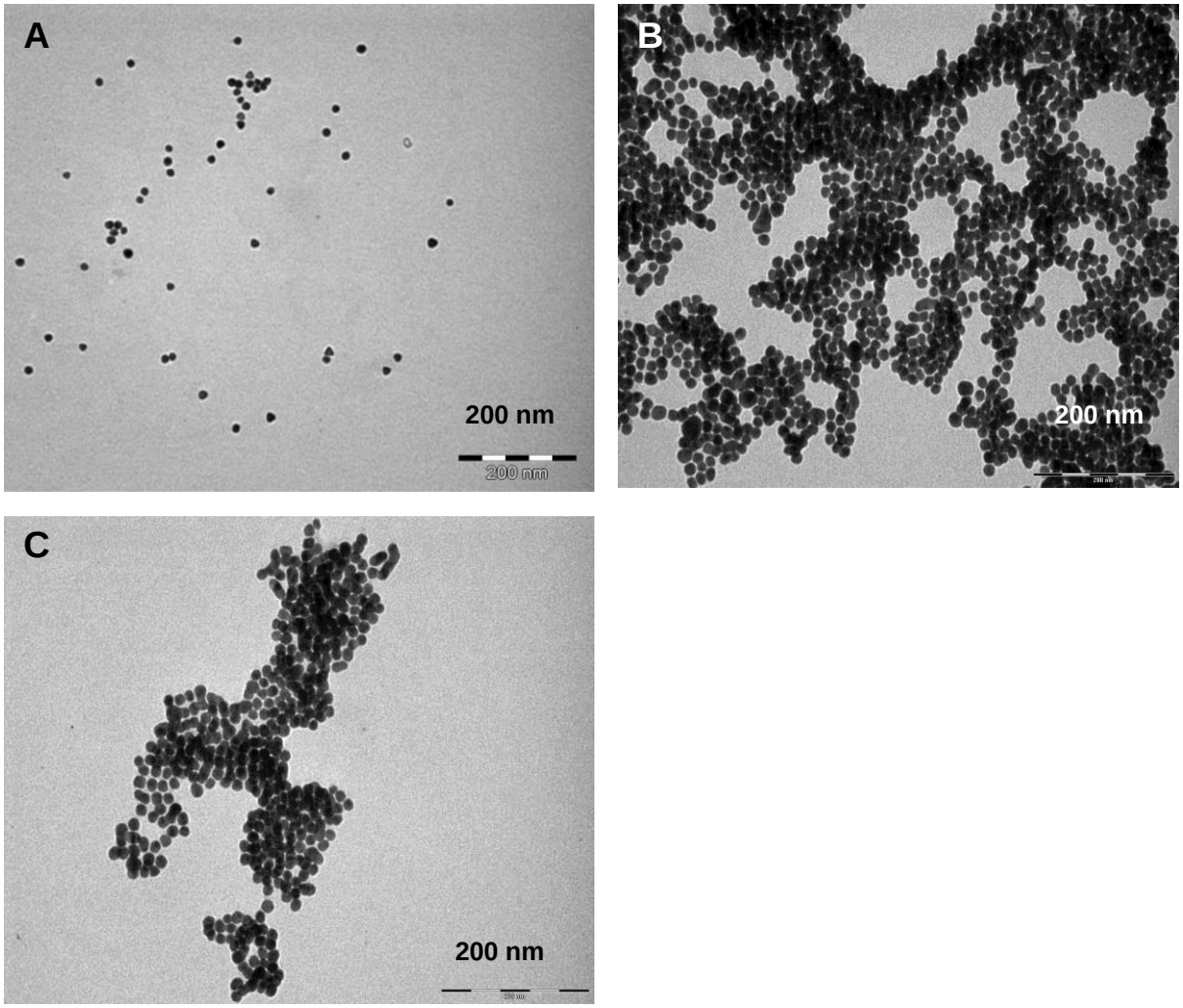

Figure 3.5: TEM images of (**A**) citrate-AuNS, (**B**) **1a**-citrate-AuNS and (C) **2a**-citrate-AuNS.

The average size of the citrate-AuNS synthesized was also determined by powder XRD, **Figure 3.6**, and by using the Scherrer [**145**] **Equation 3.1**:

$$d(\text{Å}) = \frac{k\lambda}{\beta Cos\theta} \qquad (\mathbf{3.1})$$

where k is an empirical constant equal to 0.9, λ is the wavelength of the X-ray source, (1.5405 Å), β is the full width at half maximum of the diffraction peak, and θ is the angular position of the peak. The average size of the citrate-AuNS was 5.4 nm using as determined using the peak at 64.63°, hence similar to size obtained from TEM. The gold nanoparticles show slightly broader peaks as compared to the conjugate due to a bigger size of the conjugate. It has been reported that both the degree of crystallization and the change in interplanar space, imply a new crystal form or a new compound in phthalocyanines [**146**]. Thus the change in 2θ angles and d-spacings (**Figure 3.6**) including the appearance of new XRD peaks confirm a new crystal formation of the phthalocyanine or a new compound, confirming conjugation. The 2θ angles and d-spacings in **1a**-citrate AuNPs and **2a**-citrate AuNS are almost the same as for unconjugated gold nanoparticles.

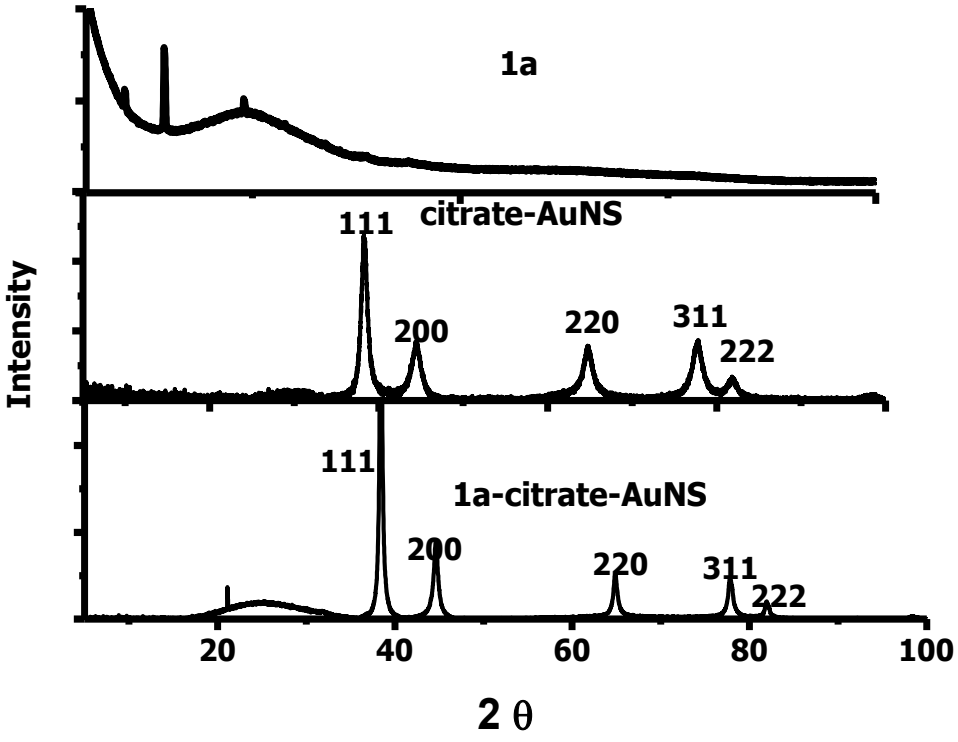

Figure 3.6: XRD patterns of **1a**, citrate-AuNS, and **1a**-AuNS.

3.4.1.2. TOABr-AuNS linked to 3

TEM micrographs of the AuNPs and **ZnPcSH** (**3**)–TOABr-AuNS, **Figure 3.7** show monodispersed spherical AuNPs with an average particle size of 5.5 nm, **Table 3.3**. On conjugation with **ZnPcSH** (**3**) complex the particles show slight aggregation (**Figure. 3.7(B)**), with an estimated average size of 16.2 nm.

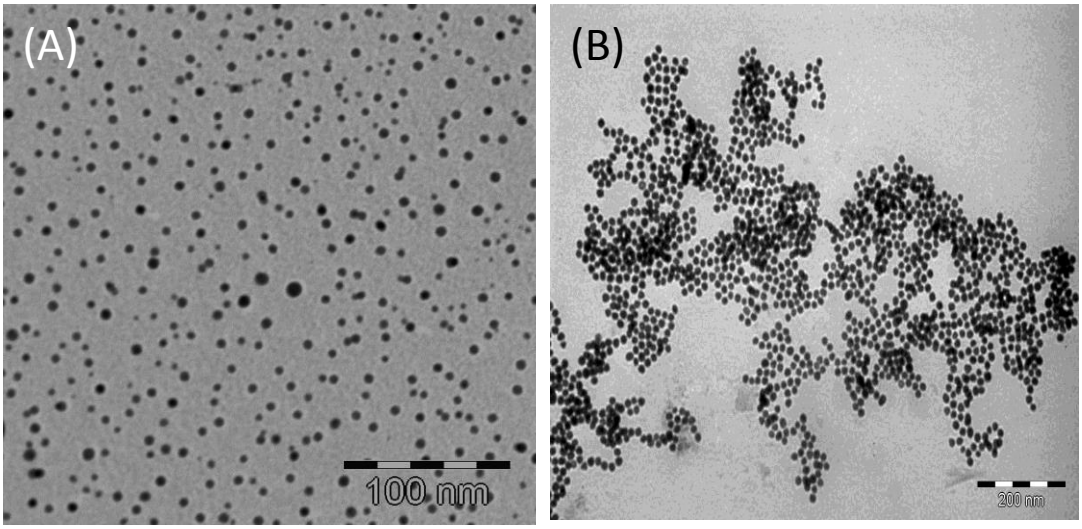

Figure 3.7: TEM micrographs of (A) TOABr-AuNS, and (B) **3**-AuNS.

The XRD patterns of TOABr-AuNS and **3**-AuNS were both indexed to a face centred cubic structure of gold nanoparticles (**Figure 3.8**). The estimated average size of the TOABr-AuNS and **3**-AuNPs were 5.3 nm and 17 nm, respectively, using the peak at 37.58°. The values are similar to those obtained from TEM, **Table 3.3**. The large size of **3**-AuNS suggests aggregation.

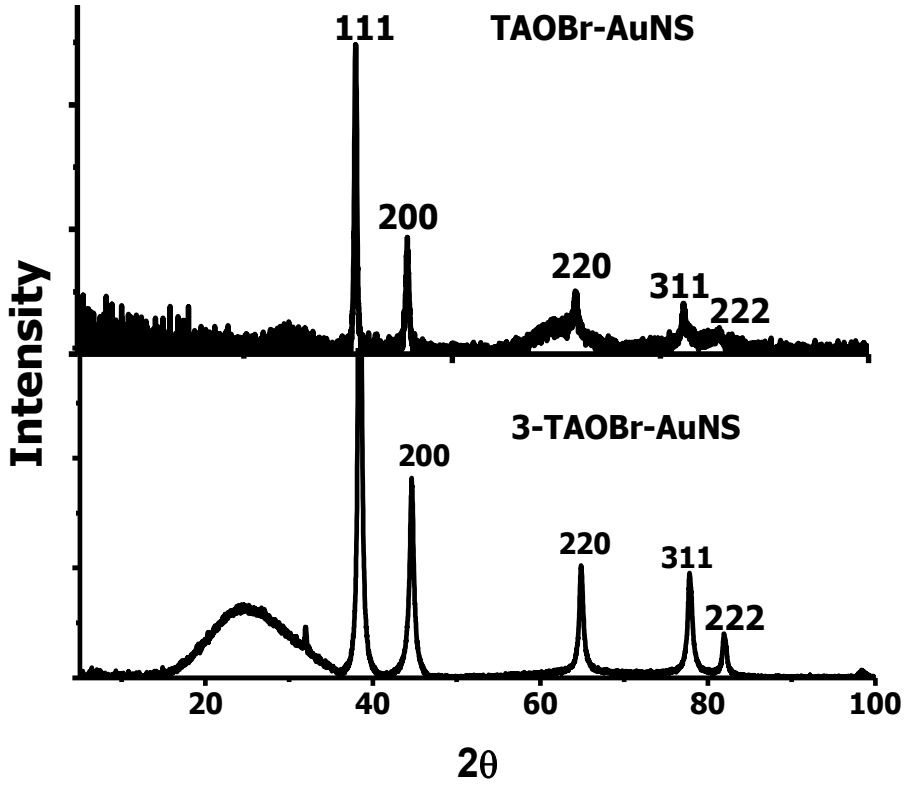

Figure 3.8: XRD patterns of AuNP, **ZnPcSH (3)** and **3**-TOABr-AuNS.

3.4.2. Conjugates with non-spherical gold nanoparticles

3.4.2.1. AuNRs and AuBPs

*AuNRs (**3.2**) was compared to AuBPs hence, one size of NRs is discussed here. Complex **2a** was used as an example to study the effect of different shapes (NRs and BPs)*

The TEM image in **Figure 3.9** (**A**) shows the distribution of the as synthesized AuNRs (represented as AuNRs (**3.2**). The average aspect ratio (length/diameter) of the nanorods was 3.2. **2a-AuNR (3.2)** conjugate in **Figure 3.9**(**B**) shows that upon conjugation the rods were drawn closer together showing some aggregation, with an aspect ratio of 3.7. Increasing the concentration of the $AgNO_3$ solution from 0.004 M to 0.04 M favored the formation of gold nanoparticles with a bipyramidal shape (**AuBP**) (**Figure 3.9** (**C**)). Lui and Guyot-Sionnest [**31**] also observed the formation of bipyramidal gold nanostructures in the presence of silver nitrate. The aspect ratio of the bipyramidal nanoparticles was found to be 2.5. Upon conjugation AuBPs the aspect ratio increased to 2.9 showing aggregation (**Figure 3.9** (**D**)).

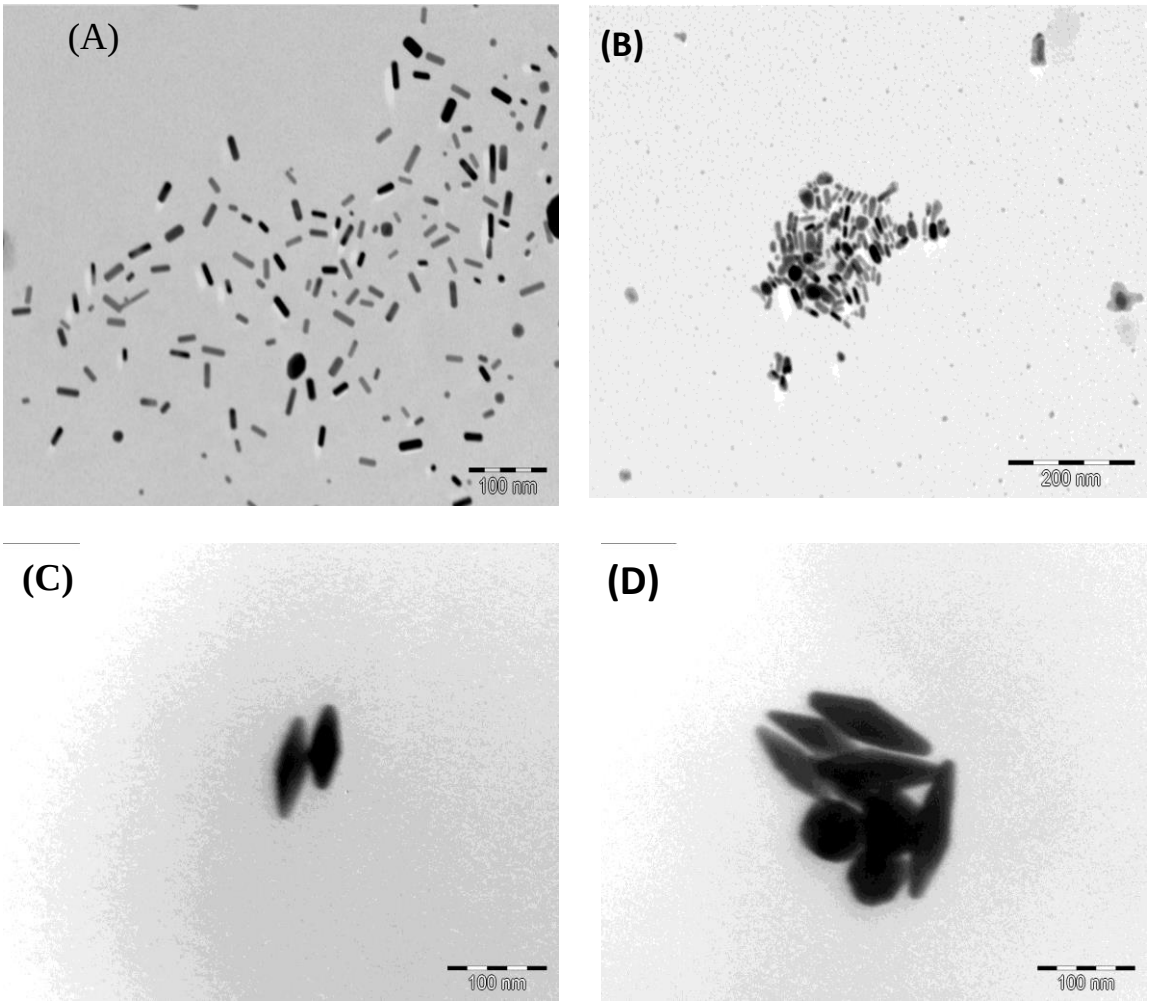

Figure 3.9: TEM images of (A) **AuNR (3.2)** alone and (B) complex **2a-AuNR (3.2)**, (C) **AuBP** alone and (D) complex **2a- AuBP**.

3.4.2.2. Synthesis of different sized gold nanorods

TEM image (**Figure not shown**) of CTAB-AuNS (represented as AuNR (**1.0**)), which were used for comparison with AuNR has an average size of 5.4 nm as discussed above. AuNRs shown in **Figure 3.10** have the aspect ratio of (**A**) **2.0**, (**B**) **4.7** and (**C**) **7.1** (represented as AuNRs (**2.0**), AuNRs (**4.7**) and AuNRs (**7.1**)), respectively. The morphology of the gold nanoparticles did not change upon conjugation except the slight changes in particle sizes, **Figure 3.10**. The aspect ratios of the conjugated NRs (to **4**) were (**2.9)**, (**4.9)** and (**7.8)** showing a slight increase in size.

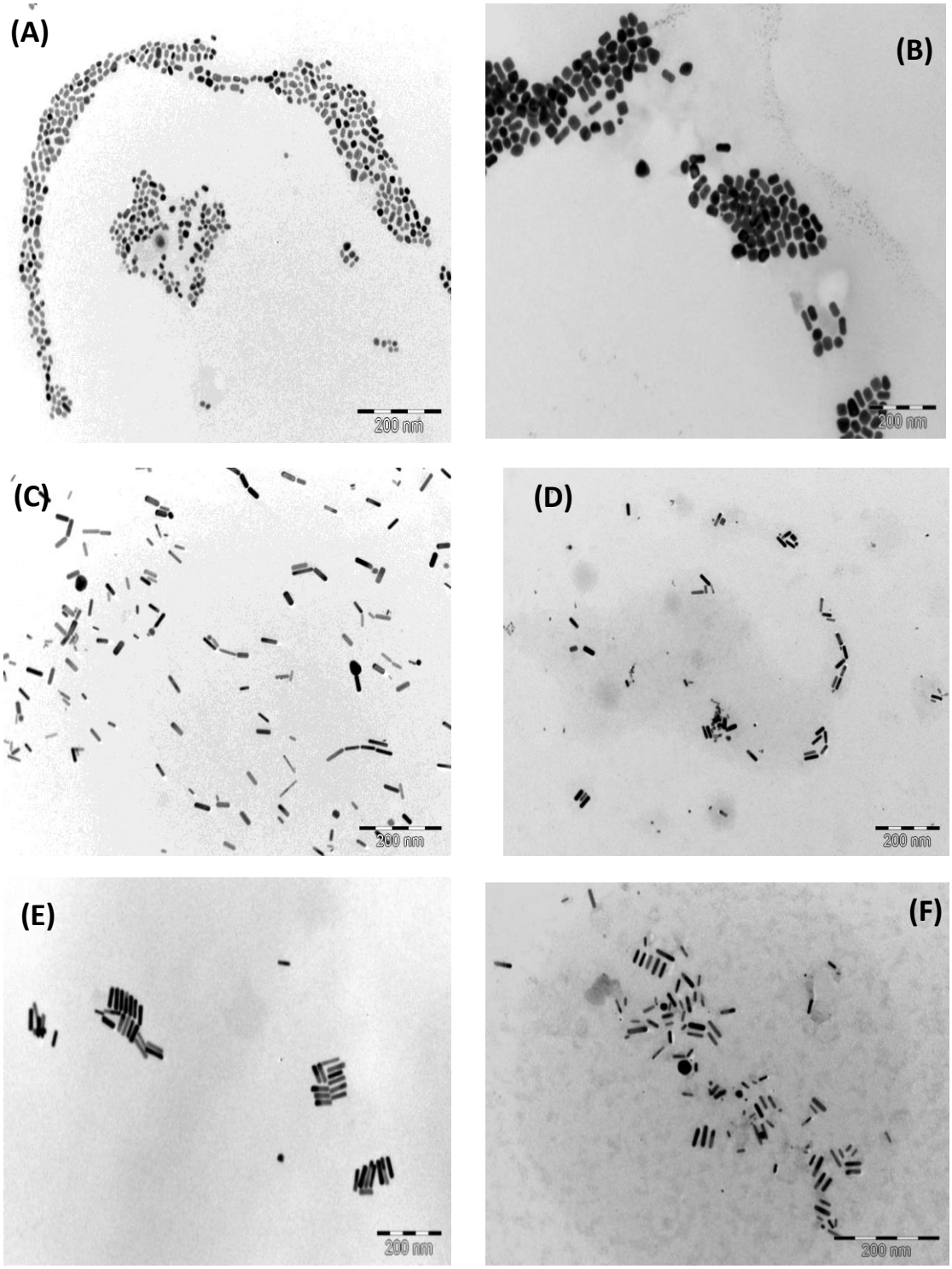

Figure 3.10: TEM images of gold (A) AuNRs (**2.0**), (B) **4**-AuNRs (**2.0**), (C) AuNRs (**4.7**), (D) **4**-AuNRs (**4.7**), (E) AuNRs (**7.1**), and (F) **4**-AuNRs (**7.1**).

Table 3.3: Sizes of AuNS and NRs (from TEM) and their SPR wavelength maxima.

Sample	Size (TEM)	SPR λ(nm)	solvent
Citrate-AuNS	**5.2**	**530**	**H_2O**
1a- Citrate-AuNS	**10.6**	**539**	**DMSO**
2a- Citrate-AuNS	**11.5**	**550**	**DMSO**
TOABr-AuNS	**5.5**	**510**	**Toluene**
3-TOABr-AuNS	**16.2**	**516**	**DMSO**
CTAB-AuNS	**5.4**	**518**	**H_2O**
2a-CTAB-AuNS	**11.2**	**547**	**DMSO**
4-CTAB-AuNS	**5.6**	**543**	**pH9buffer**
CTAB-AuNR (2.0)	**[a]2.0**	**528, 643**	**H_2O**
4-CTAB-AuNR (2.0)	**[a]2.9**	**546**	**pH9buffer**
CTAB-AuNR (3.2)	**[a]3.2**	**513, 749**	**H_2O**
4-CTAB-AuNR (3.2)	**[a]3.7**	**538**	**pH9buffer**
CTAB-AuNR (4.7)	**[a]4.7**	**518, 745**	**H_2O**
4-CTAB-AuNR (4.7)	**[a]4.9**	**528**	**pH9buffer**
CTAB-AuNR (7.1)	**[a]7.1**	**518, 825**	**H_2O**
4-CTAB-AuNR (7.1)	**[a]7.8**	**525, 840**	**pH9buffer**
CTAB-AuBP	**[a]2.5**	**548**	**H_2O**
2a-CTAB-AuBP	**[a]2.9**	**548**	**DMSO**

[a] aspect ratio.

3.5. Ground state absorption and fluorescence spectra of Pc-AuNP conjugates.

3.5.1. AuNPs alone

Citrate-AuNS shows the surface plasmon resonance (SPR) band for AuNP at 530 nm. This is consistent with the reported SPR peak for gold nanoparticles of sizes less than 50 nm [**147,148**]. The surface plasmon peak in TOABr-AuNS was observed around 510 nm. **Figure 3.11** shows the UV-Vis spectra of the gold nanospheres and nanorods with varying aspect ratios. Gold nanospheres showed one absorption peak at 518 nm. However, for nanorods there were two absorption peaks observed and the longitudinal peak was tuned to the near infrared, **Table 3.3** by increasing the aspect ratio. The aspect ratio of the gold nanorods was controlled by the amount of silver nitrate added and was found to decrease with an increase in $AgNO_3$. The SPR for all the AuNPs are listed in **Table 3.3**.

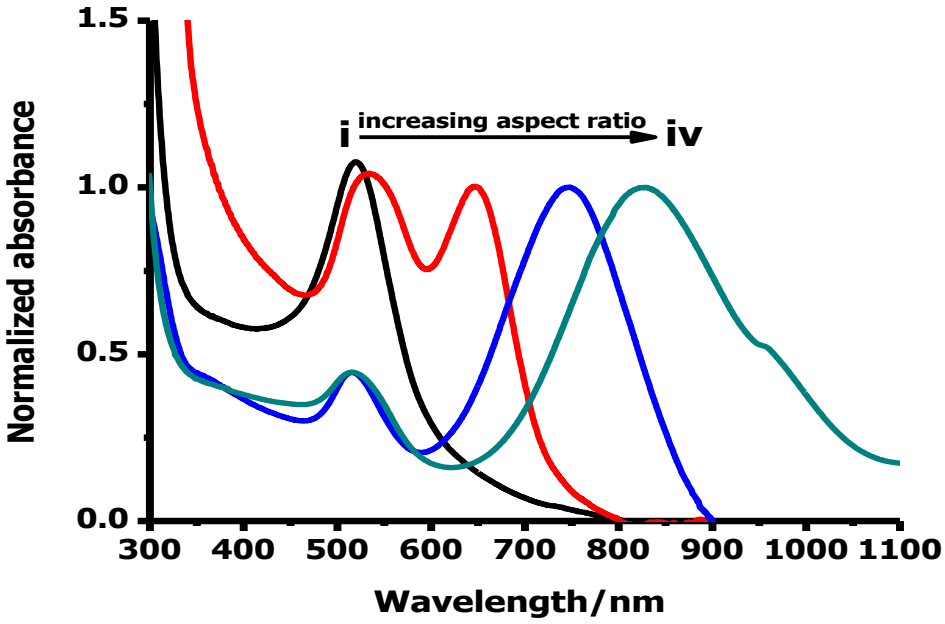

Figure 3.11: UV-Vis spectra of AuNPs (i) CTAB-AuNS, **4**-AuNRs (**2.0**), **4**-AuNRs (**4.7**) and **4**-AuNRs (**7.1**).

3.5.2. Conjugates AuNS with 1a, 2a and 4

SPR bands of AuNS in the conjugates are red shifted due to an increase in size upon conjugation with phthalocyanines. For example upon conjugation with the phthalocyanine the SPR peak of citrate-AuNS shifted to 539 and 550 nm for **1a** or **2a** respectively, from 530 nm of AuNS alone (**Table 3.3**).

Table 3.4: Spectral properties of phthalocyanines- AuNPs conjugates.

Conjugate	$^{a}\lambda_{Abs}$ /nm	$^{a}\lambda_{Exc}$ /nm	$^{a}\lambda_{Em}$ /nm	Solvent
1a	**687**	**688**	**699**	**DMSO**
1a-citrate-AuNS	**684**	**689**	**698**	**DMSO**
2a	**691**	**692**	**703**	**DMSO**
2a-citrate-AuNS	**685**	**686**	**695**	**DMSO**
2a –CTAB-AuNS	**685**	**686**	**695**	**DMSO**
2a- AuNR(3.2)	**702**	**703**	**717**	**DMSO**
2a- AuBP	**704**	**704**	**720**	**DMSO**
3	**694**	**695**	**708**	**DMSO**
3-TOABr-AuNS	**692**	**694**	**706**	**DMSO**
4	**638, 696**	**696**	**704**	**pH 9 buffer**
4 –CTAB-AuNS	**692**	**693**	**704**	**pH 9 buffer**
4 -AuNR (2.0)	**694**	**694**	**706**	**pH 9 buffer**
4 -AuNR (4.7)	**692**	**692**	**703**	**pH 9 buffer**
4 -AuNR (7.1)	**692**	**692**	**712**	**pH 9 buffer**

$^{a}\lambda_{Abs}$ = Absorption maximum, λ_{Exc} = excitation maximum, λ_{Em} = emission maximum.

The UV-Vis spectra are shown in **Figure 3.12** for **1a**-citrate-AuNS, **2a**-citrate-AuNS, **3**-TOABr-AuNS (in DMSO) and **4**-CTAB-AuNS in pH 9 buffer together with their unconjugated phthalocyanine derivatives. The conjugation of phthalocyanine molecules on AuNS results in broadening and blue shifting of the phthalocyanine Q-band absorption, **Table 3.4**. The broadness was attributed to aggregation of the tightly packed phthalocyanine molecules on the gold surface [**96**]. A blue shift in the Q band is observed upon conjugation since the SR groups are now engaged with the AuNPs reducing their electron donating abilities. The absorption spectra of both **1a**-citrate-AuNS and **2a**-citrate-AuNS in water (without DMSO) showed extensive aggregation, hence are not included. **Figure 3.12** (**D**) shows the UV-Vis spectra of **4**-CTAB-AuNS in pH 9 buffer.

The conjugation of gold nanoparticles to **4** slightly changed the Q-band maxima of the monomer peak of **4**, and the aggregation was reduced. Thus linking of CTAB-AuNS to **4** reduces aggregation. Disaggregation of Pc molecules has been observed before for star shaped AuNPs but not for spherical ones [**98**]. However, in this work the spherical nanoparticles also break aggregates, **Figure 3.12** (**D**).

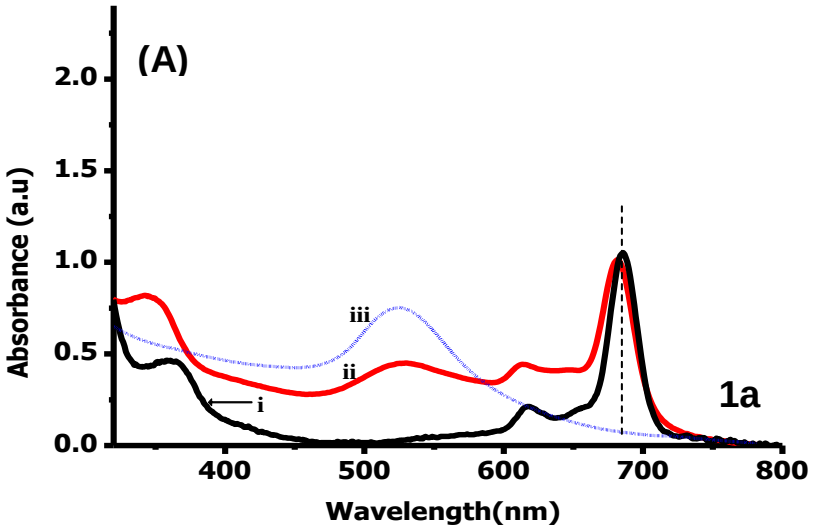
(A)
Absorbance (a.u)
Wavelength(nm)
iii
ii
i
1a

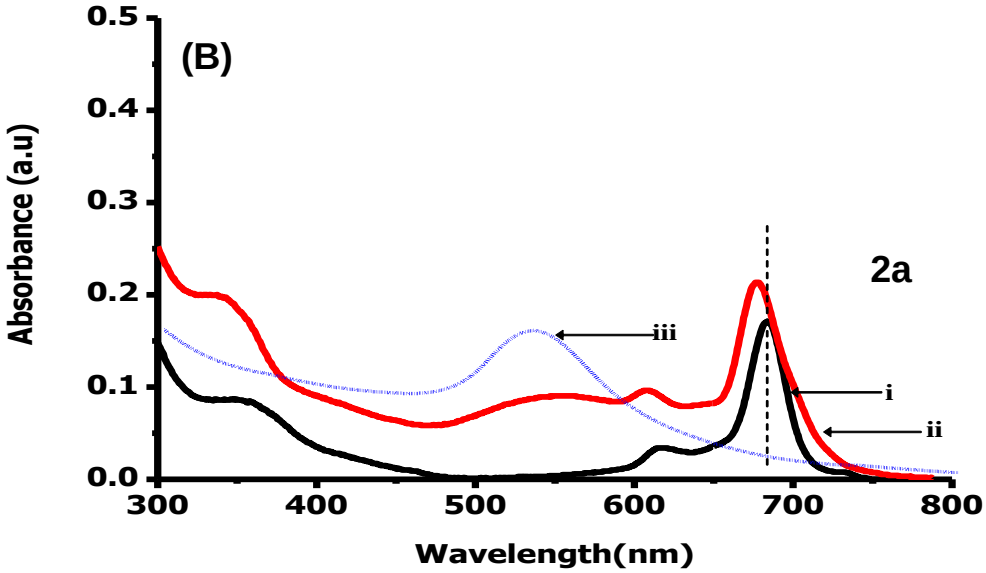
(B)
Absorbance (a.u)
Wavelength(nm)
iii
i
ii
2a

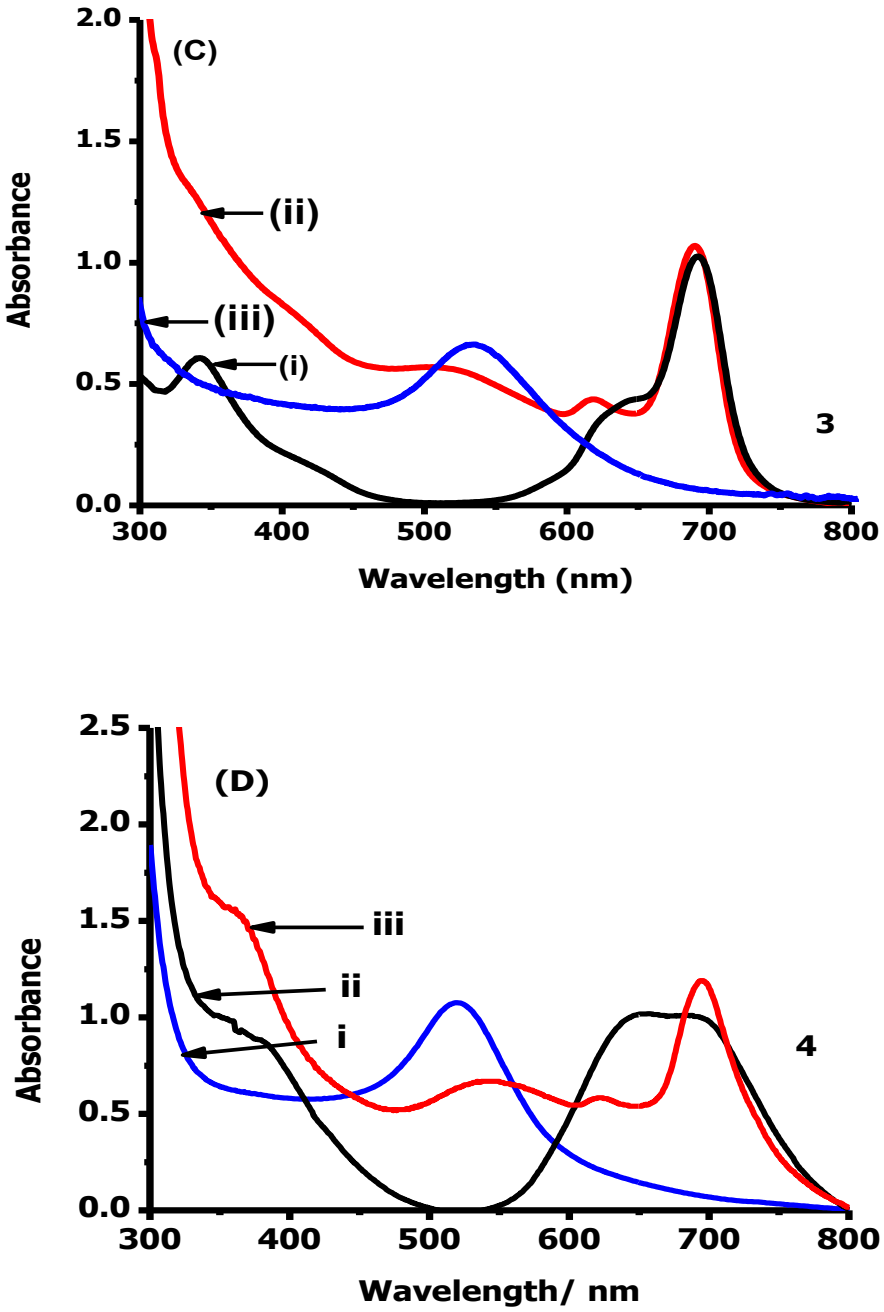

Figure 3.12: UV-Vis spectra of AuNS and their conjugates; (A) **1a** in DMSO, (B) **2a**, in DMSO (C) **3** in DMSO and (D) **4** in pH 9 buffer; (i) Pc, (ii) Pc-AuNS and (iii) AuNS. (For **1a** and **2a** conjugated to citrate-AuNS, **3** to TOABr-AuNS and **4** to CTAB-AuNS)

The UV-Vis absorption, emission and excitation spectra of **1a**-citrate-AuNS, **2a**-citrate-AuNS, **3**-TOABr-AuNS, **4**-CTAB-AuNS are shown in **Figure 3.13**. The absorption spectra were not similar to excitation spectra due to broadening by AuNPs.

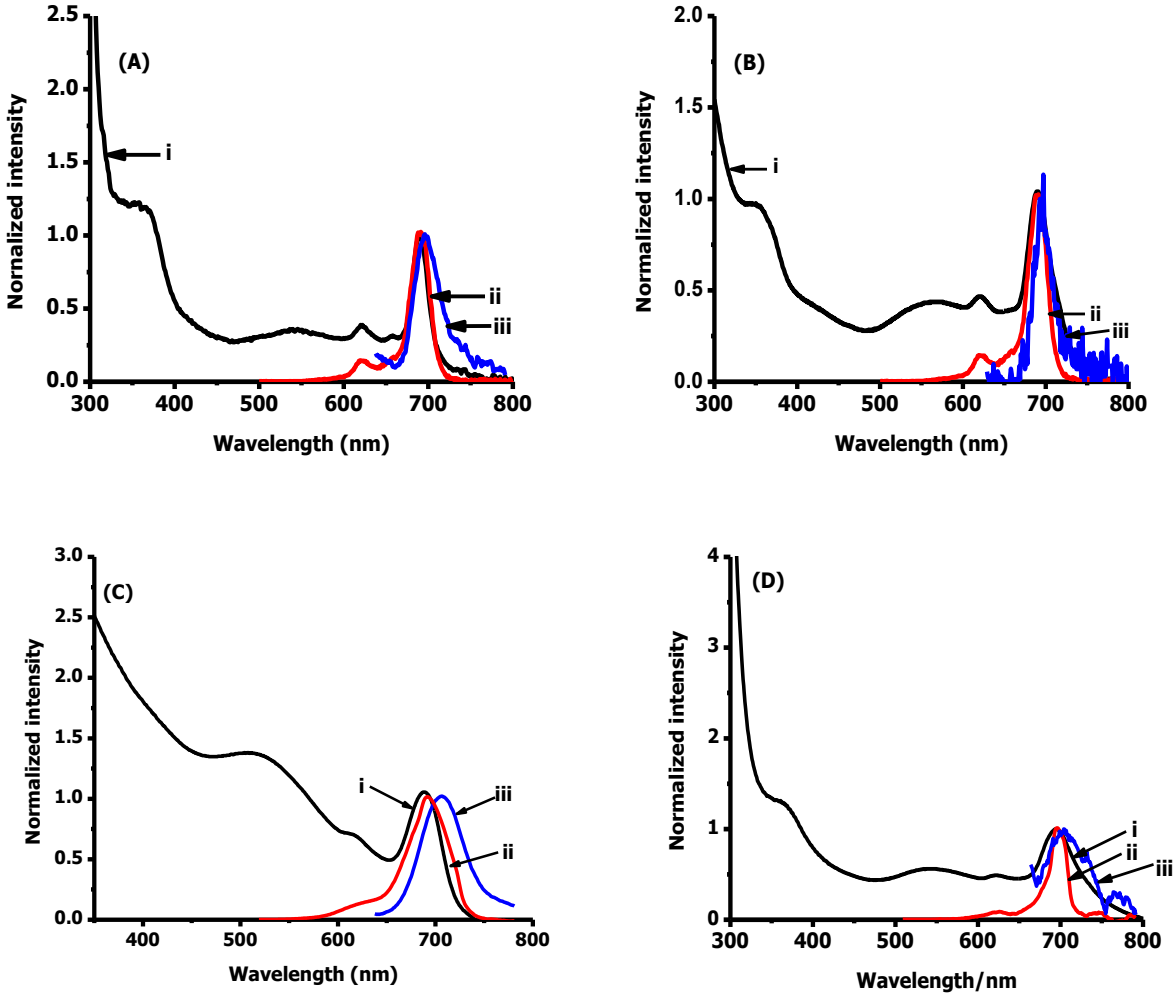

Figure 3.13: (i) Absorption, (ii) excitation and (iii) emission spectra of (A) **1a-citrate-AuNS** in DMSO, (B) **2a-citrate-AuNS** in DMSO**,** (C) **3-TOABr-AuNS** in DMSO and **4-CTAB-AuNS** in pH 9 buffer.

3.5.3. Conjugates of 2a with AuNRs and AuBPs

The conjugation of AuNRs (**3.2**) resulted in the red shifting, **Table 3.4**, and broadening of the Q-bands of **2a** in DMSO (**Figure 3.14A and B**). Broadening of the phthalocyanine Q-band absorption in the presence of nanoparticles was also observed for the AuNS as explained above. Red shifts were observed instead of a blue shift for AuNS. It is possible that the red shifts observed in the Q band of the Pc in the presence of the AuNR may be due to longitudinal dipole moment arrangement of both, which is known to result in red shifts for other chromophores [**149**]. This shows that anisotropism favours red shifting of the Q-band compared to the blue shift observed for AuNS.

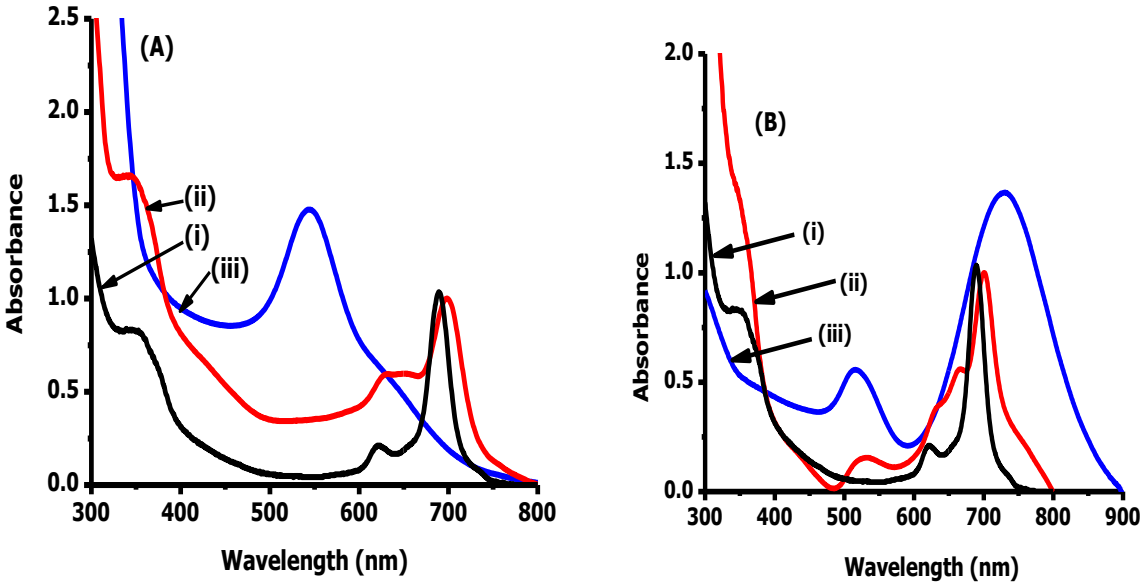

Figure 3.14: UV-Vis spectra of (A) AuBPs and (B) AuNRs (**3.2**), and their conjugates. (i) **2a** and (ii) **2a**-AuBPs or **2a**-AuNRs (**3.2**) and (iii) AuBP or AuNRs in DMSO.

3.5.4. Conjugates of 4 with AuNRs (different aspect ratio)

The UV-Vis spectra of **4**-AuNR (different aspect ratio) in pH 9 buffer are shown in **Figure 3.15**. The conjugation of AuNRs to **4** did not significantly shift the Q band (**Table 3.4**) maxima of the monomer peak of **4** but the aggregation was reduced as judged by the decrease in the aggregate peak near 630 nm. The nitro or sulfur groups on compound **4** are not directly substituted to the phthalocyanine ring, thus there is a larger distance between the nanoparticles and the Pc ring compared to the conjugates of **2a**. For this reason it is possible that conjugation of AuNPs to **4** would not have a significant effect on the shifting of the Q band as in **2a**. Thus linking of AuNPs to **4** reduces aggregation, as discussed above for AuNS (**Figure. 3.15**).

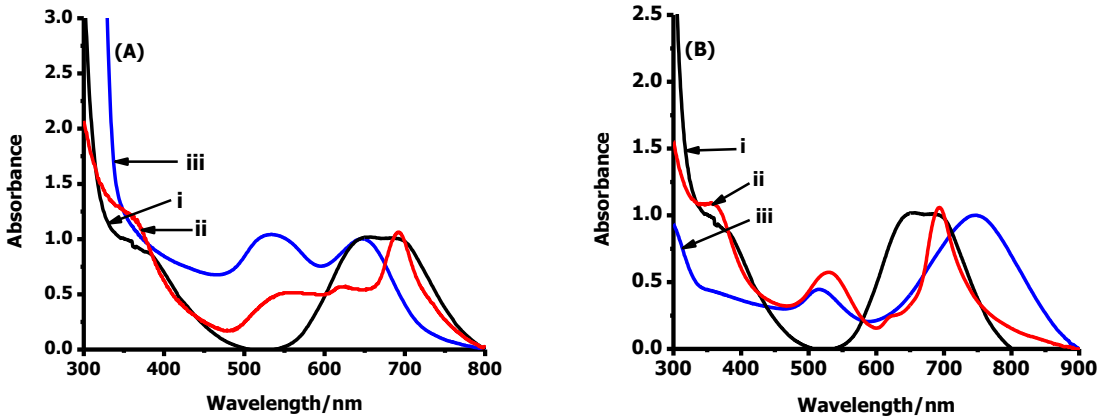

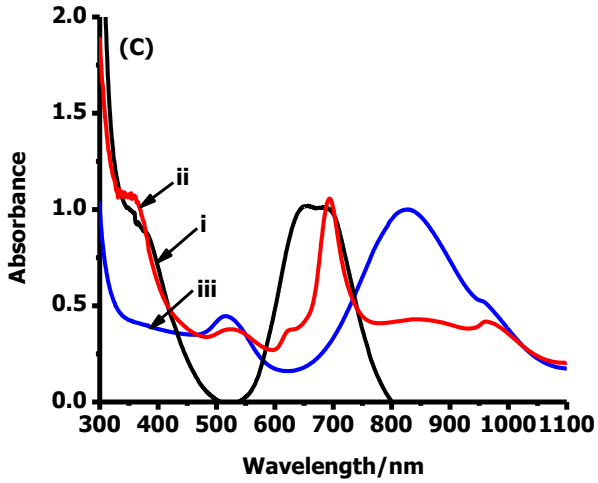

Figure 3.15: UV-Vis spectra of (i) **ZnTTAPc (4)**, (ii) **4**-AuNRs and (iii) AuNPs alone; (A) AuNRs (**2.0**), (B) AuNRs (**4.7**) and (C) AuNRs (**7.1**), and the conjugates.

There is a narrowing of the excitation spectra compared to absorption spectra for Pc-AuNPs conjugates due to the SPR band, **Figure 3.16** and **3.17**. As stated above and also reported in literature [**96**], tight packing of the phthalocyanines on the gold nanoparticle surface results in broadening of the phthalocyanine Q-band in the absorption spectra.

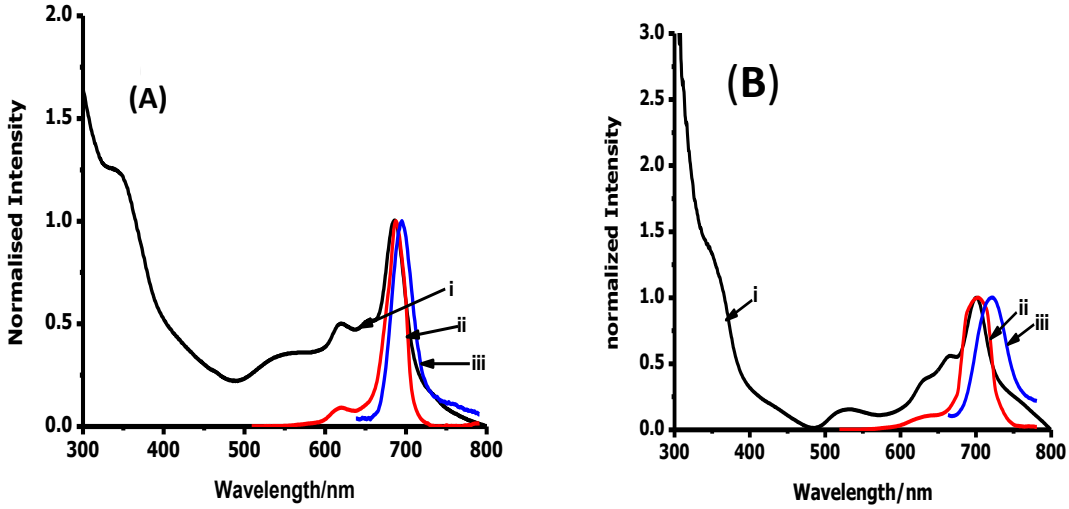

Figure 3.16: (i) Absorption, (ii) excitation and (iii) emission spectra of (A) **2a- AuBPs**, (B) **2a-AuNR (3.2)** in DMSO.

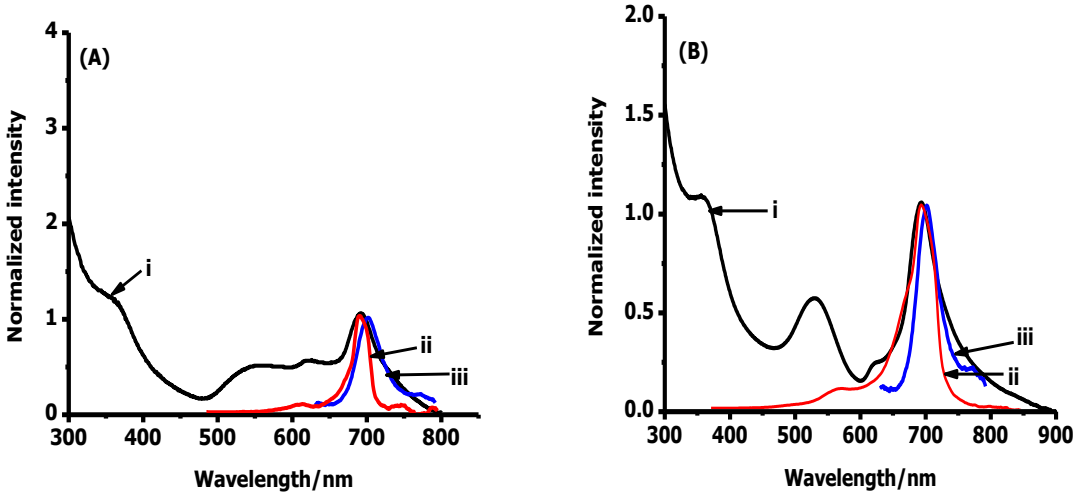

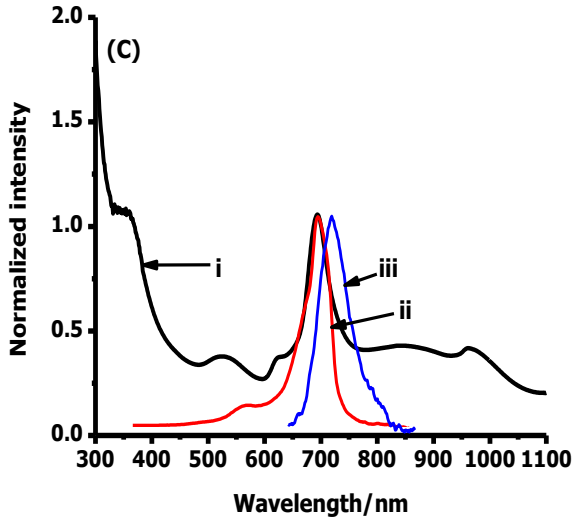

Figure 3.17: (i) Absorption, (ii) excitation and (iii) emission spectra of (A) **4**-AuNRs (**2.0**), (B) **4**- AuNRs (**4.7**) and (C) **4**-AuNRs (**7.1**) in pH 9.

3.6. XPS analysis of phthalocyanine binding on AuNPs

*The XPS studies for the binding of Pcs to AuNPs were studied using **2a**-AuNRs (**3.2**) and **4**-AuNRs (**4.7**) as examples.*

3.6.1. XPS analysis of 2a-CTAB-AuNRs (3.2)

Figure 3.18(A) shows the XPS spectra of **2a** and **2a**-AuNRs (**3.2**). The existence of the S 2p doublets ($2p_{3/2}$ and $2p_{1/2}$) is a result of the spin-orbit coupling [**150**]. The phthalocyanine alone showed two characteristic peaks at 161.0 and 162.4 eV. The $2p_{3/2}$ at 161 eV is commonly attributed to isolated sulfur or intact molecules [**151**]. However, for the conjugate **2a**-AuNRs (**3.2**) the two S 2p peaks shifted to higher binding energies at 162.5 and 163.7 eV, **Figure 3.18 A(ii)**. The 162.5 eV peak is due to the sulfur bonded to gold surface while the second peak at 163.7 eV could be assigned to physisorbed molecules on gold surface [**152-155**]. The shift in the binding energies is due to the loss of the electron lone pair when sulfur is adsorbed on gold surface.

The nitrogen 1s high-resolution XPS spectrum of the phthalocyanine showed three characteristic peaks at 398.0, 400.1 and 401.7 eV, **Figure 3.18 B(i)**. These peaks were attributed to C=N, pyrrolic nitrogen and the quaternary nitrogen [**155-157**]. **Figure 3.18 B (ii)** shows the nitrogen 1s XPS spectrum of **2a**-AuNRs (**3.2**) conjugate. There are two characteristic peaks at 396.2 and 397.9 eV corresponding to N-Al and N-C, respectively [**158**]. The quaternary N 1s peak disappeared upon conjugation with gold nanoparticles showing the

participation of this nitrogen in the complex **2a**-AuNRs (**3.2**) conjugates. The reaction of the quaternary nitrogen on metal nanoparticle surfaces is very common in the literature [**26, 159-161**].

The carbon 1s XPS spectra of the phthalocyanine and the **2a**-AuNRs conjugate are shown in **Figure 3.18 C**. The peaks at 282.4 eV and 283.7 eV were observed on the **2a** for C=C and C-C and/or C-H respectively, **Figure 3.18 C(i)**. Carbon 1s XPS spectrum of **2a**-AuNRs (**3.2**) showed the peaks at 283.7 eV and 285.0 eV which are attributed to C=C and C-C and/or C-H, respectively [**162**], **Figure 3.18 C (ii)**. The peak shifting towards larger binding energies can be associated with loading onto AuNPs, as suggested by **Yang *et al*** [**163**].

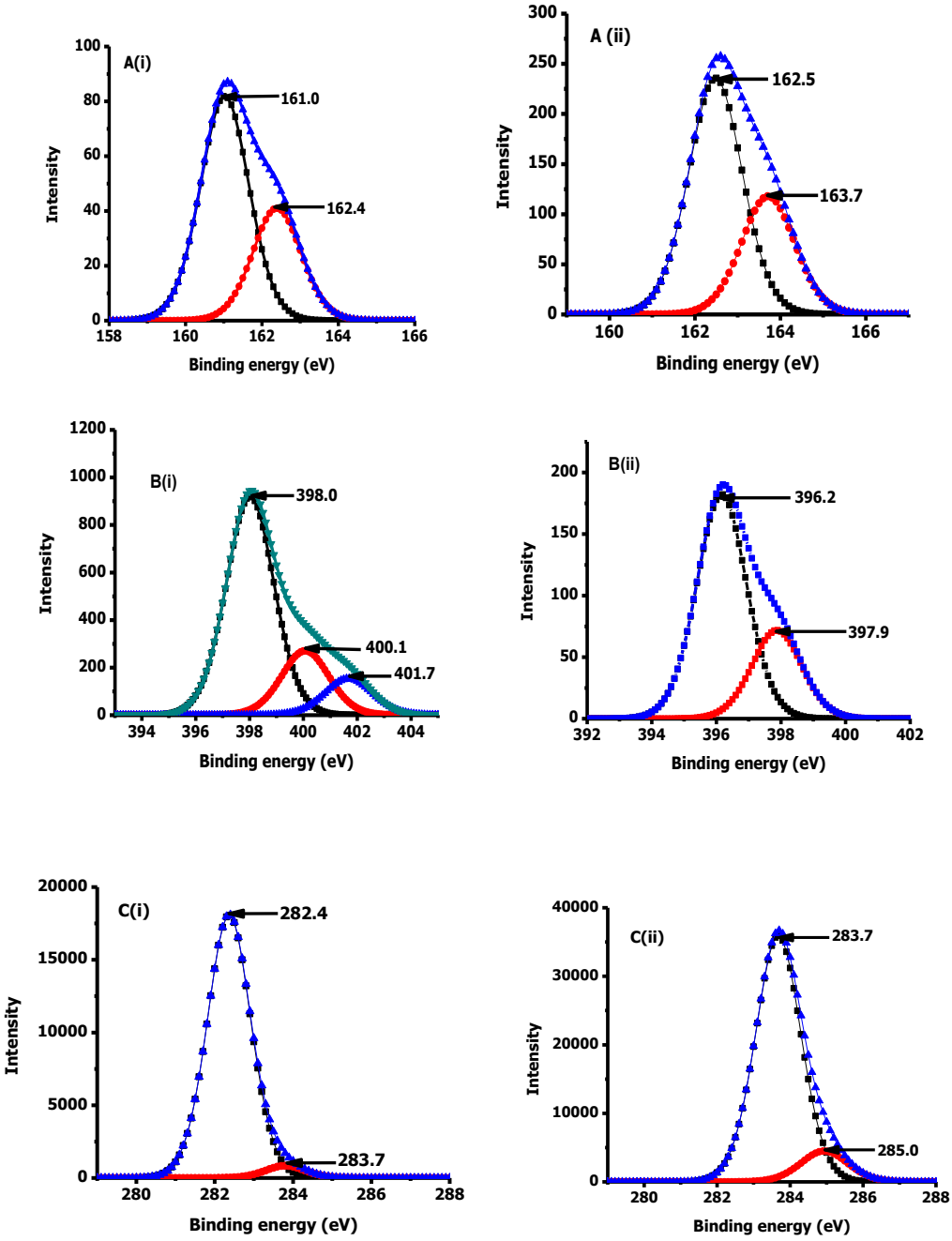

Figure 3.18: High resolution spectra of (A) sulfur 2p, (B) nitrogen 1 s and (C) carbon 1s; (i) **2a** and (ii) **2a**-AuNR(**3.2**).

3.6.2. XPS analysis of ZnTTAPc (4) - AuNR (4.7)

In order to determine if the amine or sulfur groups on the thiamine substituent on the Pc ring are coordinated to AuNPs, high resolution XPS was employed. The high resolution scans of the N (1S) for **ZnTTAPc (4)** **Figure 3.19 A**(i) shows C-NH_2, C=N and metal-N bonds. **4-AuNRs (4.7)** showed disappearance of the C-NH_2 peak, **Figure 3.19A** (ii), which proves the participation of the amine in conjugation with **AuNRs (4.7)**.

The sulfur group of the thiazole ring was also analyzed with XPS to confirm interaction with gold nanoparticles. The deconvoluted spectra for S (2p) show a doublet of ($2p_{3/2}$) and ($2p_{1/2}$) **Figure 3.19 B** (i) which is common for S (2p) [**153**]. Upon binding to gold nanoparticles the first doublet disappeared and the second doublet was observed at higher binding energies, **Figure 3.19 B** (ii). This shows that sulfur are also played a role in the formation of the **4** – AuNRs (**4.7**).

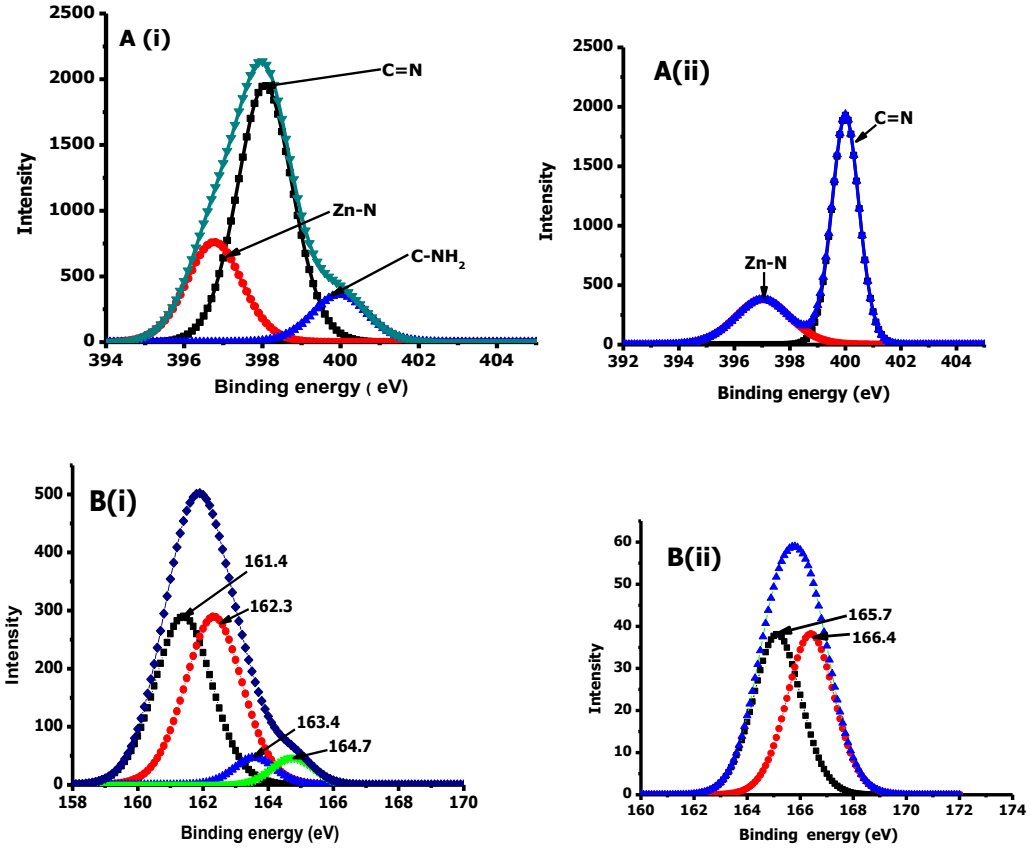

Figure 3.19: XPS deconvoluted spectra of (**A**) N 1s and (**B**) S 2p of (i) **4** and (ii) **4**-AuNR (**4.7**).

3.7. EDX of complex 2a-AuNRs (3.2) conjugates

The EDX spectrum of the CTAB-AuNR (**3.2**) in **Figure 3.20 (A)** shows the gold peaks and confirms the presence of CTAB in the samples. The presence of the carbon, bromine and nitrogen peaks is due to CTAB chains that act as a capping agent on the gold surfaces. The spectrum shows the traces of silver in the gold nanoparticles samples this is due to silver nitrate that was used in the synthesis of the NRs. The presence of **2a** in **2a**-AuNRs (**3.2**) was confirmed by

the presence of the carbon, aluminium, sulfur, iodide and oxygen elements **Figure 3.20 (B)**. A gold peak was also observed in this sample due to the gold nanoparticles. The samples contain chlorine and sodium elements could be due to impurities from the synthesis (PBS containing NaCl was employed in the final purification step). Silver was also detected in the conjugates.

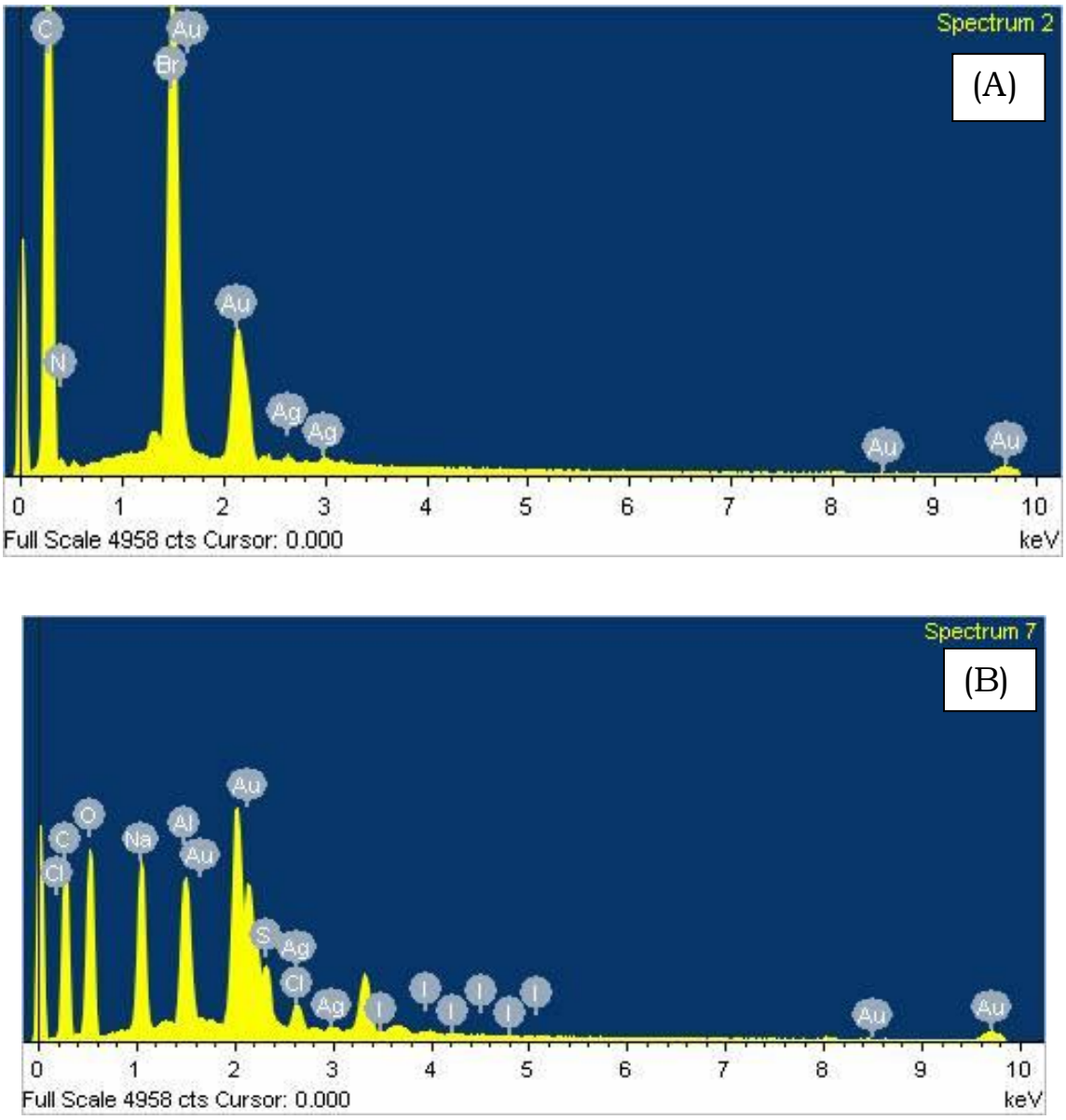

Figure 3.20: EDX spectra of (**A**) AuNRs (**3.2**) and (**B**) **2a**-AuNRs (**3.2**).

3.8. Physical analysis of the gold nanoparticles and conjugates

This analysis will help in determining the loading of Pcs on nanoparticles as well as explaining the photophysical behaviour in the next chapter.

Total number of Au atoms per AuNP, surface area of AuNPs and the number of surface Au atoms per AuNP were calculated using established methods [**131-133**] assuming perfect spherical, rod-like, and bipyramidal shapes. An increase in surface atoms was observed as the surface area increases (**Table 3.5**). The number of Pc molecules on AuNPs was also obtained using the Beer's law and the Q band absorption maximum of the Pc (assuming the extinction coefficient does not change upon conjugation) as explained in the experimental section. The number of phthalocyanine molecules per nanoparticles was found to range from 39 to 112. Adsorption of multiple dyes onto AuNPS has been reported to cause aggregation of the AuNPs, similar to the results observed for **2a**-AuNPs [**164**].

The surface area of the nanorods was found to increase as the aspect ratio increases, **Table 3.6** for **4-**AuNRs. The larger surface area results in an increase in the number of surface atoms that are important for attachment with the phthalocyanine molecules on the surface. The ratio of number of Pc molecules per number of AuNPs for **4-**AuNRs was found to range from 27 to 243, increasing with increase in surface area of the NPs, (**Table 3.6**). The surface coverage by Pcs, **Table 3.6**, was higher for nanorods with larger aspect ratio due to a larger surface area.

Table 3.5: Properties of the gold nanorods as conjugated to complex **2a**.

Sample	**Surface area (nm^2)**	**N**	**N_s**	**Average size (nm) from TEM[a]**	**Pcs/NPs**
AuNS	91	61237	6214	5.4 ±0.2 (11.2)	39
AuNR (3.7)	552	68397	9362	3.2[b] ±0.5 (3.7)	66
AuBP	26231	16430269	444901	2.5[b] ± 0.3 (2.9)	112

[a]sizes from TEM, [b]aspect ratio

Table 3.6: Properties of the gold nanorods as conjugated to **ZnTTAPC** (**4**).

Sample	**λ SPR Band (nm)**	**E ($M^{-1}cm^{-1}$)**	**Surface area (NPs) (nm^2)**	**Total Au atoms**	**Surface Au atoms**	**Pcs/ NPs**
AuNS(**1.0**)	518	1.3×10^8	14	450	235	27
AuNR(**2.0**)	528, 643	2.4×10^8	477	168214	8103	49
AuNR(**4.7**)	518,745	5.6×10^8	733	354660	124396	111
AuNR(**7.1**)	518, 825	6.9×10^8	1271	743236	215671	243

3.9. Summary

*The Pc compounds (**1a**, **2a**, **4**) were aggregated in aqueous solution as noted in their UV-Vis spectra. The addition of Triton X decreased the aggregation of the complexes. The presence of both peaks from the Pc and gold nanoparticles in the XRD patterns confirmed the presence of the Pc molecules on the gold nanoparticles. The SPR band of gold nanoparticles was observed on the absorption spectra of the conjugates. The complexes **1a**, **2a**, **3** and **4** were conjugated with AuNS and they all showed a blue shift in their absorption spectra. The UV-Vis spectra of the conjugates containing shaped AuNPs showed red shifts of Q-band compared to the Pc alone.*

Chapter 4 Photophysical and Photochemical properties

This chapter reports on the photophysical and photochemical properties of phthalocyanines and phthalocyanine-gold nanoparticle conjugates.

- ***1a*** *and* ***2a*** *are water soluble, the photophysical properties of their conjugates were studied in DMSO due to aggregation in aqueous medium, however these complexes were also studied alone in water.*
- ***3*** *is not soluble in aqueous medium, hence it is only studied in DMSO.*
- ***4*** *is soluble in aqueous medium but is aggregated, hence it was studied in pH 9 buffer + Triton X 100 as well as in DMF.*
- ***4****-AuNPs conjugates were studied in aqueous medium (pH 9 buffer) alone since aggregation was reduced in the presence of AuNPS.*

4.1. Fluorescence quantum yields and lifetimes

4.1.1. Pcs and conjugates with spherical gold nanoparticles

Table 4.1 shows that the Φ_F values in DMSO are higher than in water due to aggregation for **1a** and **2a**. Aggregates can convert electronic excitation energy into vibrational energy which therefore decreases the fluorescence quantum yields of the molecules [**165**]. The Φ_F values for **1a** and **2a** in water were improved in the presence of Triton X 100 due to reduction in the number of aggregates. Even though the sizes of Al and Mg are similar, the presence of the hydroxy axial ligand in **1a** and **2a** will encourage intersystem crossing

compared to complexes **1** and **1a**, hence lowers Φ_F values for **2** and **2a** compared to **1** and **1a**. It was not possible to calculate the fluorescence quantum yield (Φ_F) of **ZnTTAPc** (**4**) in aqueous media without Triton X 100 due to very weak fluorescence as a result of the highly aggregated nature of this molecule. The fluorescence quantum yield was measured in pH 9 buffer + Triton X 100 to be Φ_F = 0.01, a value lower than in DMF at Φ_F = 0.09 **Table 4.1**. The value in DMF is still lower than is typical of unaggregated ZnPc derivatives in organic solvents [**90**], due to the known [**166**] quenching of excited states by amino groups which form part of the thiamine substituent on the Pc ring. **1a** and **2a**, show lower Φ_F than **1** and **2** due to quaternization, which is to decrease Φ_F values [**167**].

A decrease in the fluorescence quantum yield of **1**, **2**, **3** and **4** in the presence of AuNPs is a result of the heavy atom effect which encourages ISC to the triplet state lowering Φ_F values [**168**]. This decrease of the fluorescence quantum yield has been observed previously for gold nanoparticles-fluorophore systems [**68, 168, 169**], due to the heavy atom effect of the AuNPs.

Table 4.1: Summary of fluorescence properties of the phthalocyanine complexes and the conjugates with AuNS.

Complex	**Solvent**	Φ_F **± 0.01**	[a]τ_F **(ns)**	τ_0 **(ns)**
1	**DMSO**	**0.21**	**5.22(1)±0.02**	**24.9**
2	**DMSO**	**0.14**	**4.82(1)±0.04**	**34.4**
1	**DMSO**	**0.16**	**4.99(1)±0.02**	**31.2**
1	**H_2O**	**0.008**	**3.66(1)±0.01**	**457.5**
1	**H_2O + Ttiton X 100**	**0.16**	**4.94(1)±0.05**	**30.9**
1a-citrate-AuNS	**DMSO**	**0.10**	**4.75(0.86) ±0.01** **0.37(0.14)**	[b]**41.4**
2	**DMSO**	**0.12**	**4.99(1.0)±0.03**	**41.6**
2	**H_2O**	**0.02**	**4.06(1)±0.02**	**203.0**
2	**H_2O + Ttiton X 100**	**0.09**	**4.56(1)±0.01**	**50.7**
2a- citrate AuNS	**DMSO**	**0.04**	**4.31 (0.93) ±0.01** **0.38 (0.06) ±0.01**	[b]**100.8**

2a-CTAB-AuNS	**DMSO**	**0.07**	**3.71(0.82)±0.02** **0.46(0.18)**	**[b]44.6**
3	**DMSO**	**0.06**	**3.08 ± 0.02**	**51.3**
3-TOABr-AuNS	**DMSO**	**0.04**	**2.38 (0.65) ±0.02** **1.54(0.35) ±0.01**	**[b]78.8**
4	**pH 9 buffer + Triton X 100)**	**0.01**	**2.71(0.94)± 0.02** **0.69 (0.56)± 0.02**	**[b]293.4**
4	**DMF**	**0.09**	**2.43 (1)± 0.01**	**27.0**
4-CTAB AuNS	**pH 9 buffer**	**0.01**	**2.39(0.86)± 0.01** **0.49 (0.13)± 0.01**	**[b]106.0**

([a] Abundance in brackets. [b]average lifetime used).

Figure 4.1 show time-resolved fluorescence decay curves of (A)(i) complex **2a** (as an example), (ii) **2a-**AuNPs and (B) (i) **ZnPcSH (3)** and (ii) **ZnPcSH(3)-**AuNPs, as examples.

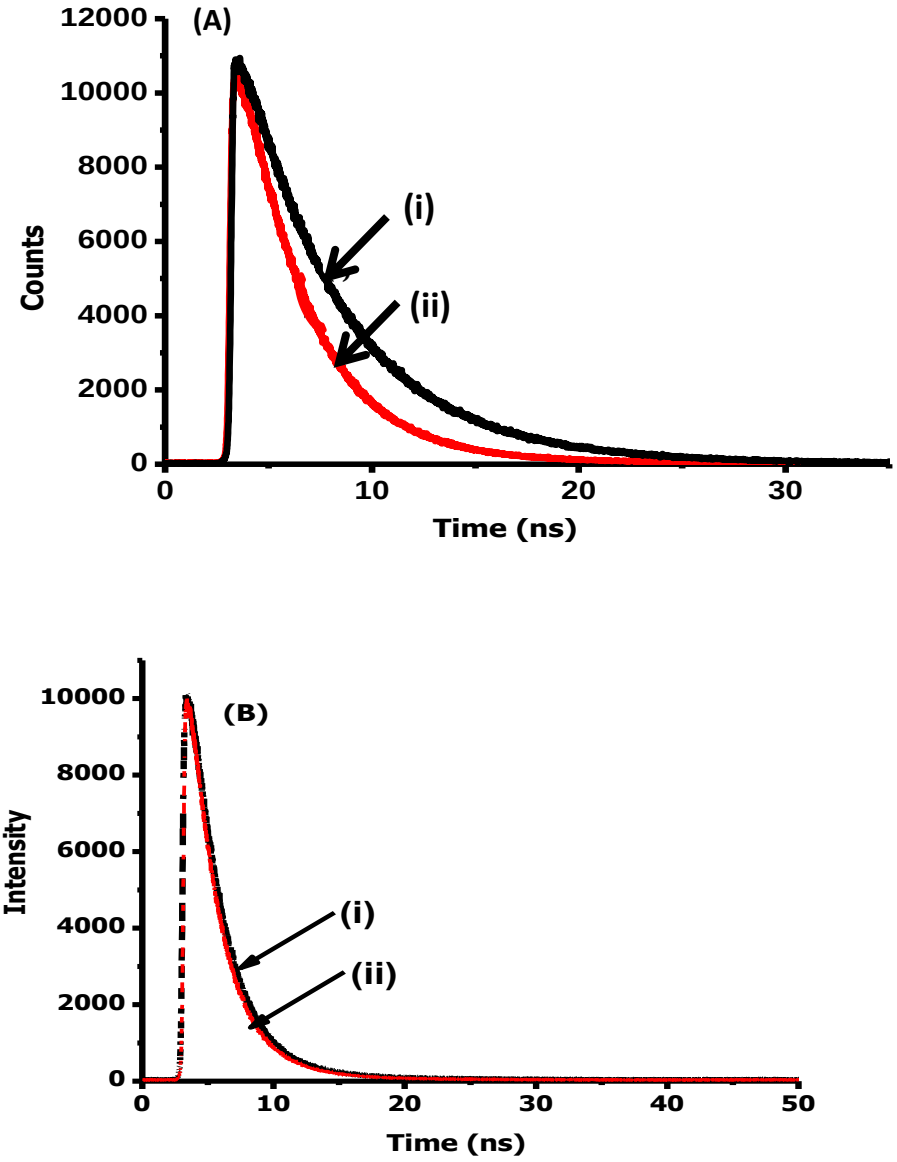

Figure 4.1: Fluorescence decay curves for (A)(i) **2a** and (ii) **2a-**AuNS and (B) (i) **ZnPcSH (3)** and (ii) **ZnPcSH (3) -**AuNS in DMSO.

Fluorescence lifetime is a measure of the average time a molecule can stay in its excited state. The fluorescence decay of all the complexes were measured in DMSO while complex **1a** and **2a** were also measured in water. Complex **4** was measured in DMF and pH 9 buffer, **3** in DMSO. For complexes **1**, **2**, **1a**, **2a**, **3** one lifetime was obtained, for **4** two lifetimes were obtained in aqueous medium but one in DMF, **Table 4.1**.

For the conjugates, two lifetimes were observed. **Table 4.1**. The first component may be due to the presence of free phthalocyanines and the second component is most likely due to the Pc derivatives conjugated to the nanoparticles.

The fluorescence lifetimes of the free Pc is slightly decreased in the conjugates (MPc-AuNPs) due to the presence of aggregates which quench the flurescence resulting in quenched and unquenched fluorescence [**165**]. The quenching of lifetimes may be explained using fluorescence radiative lifetime (τ_0). The τ_0 values were higher than the measured fluorescence lifetimes (τ_F) (**Table 4.1**). The large values of τ_0 (calculated using **equation 1.2**) compared to τ_F are not surprising because non-radiative processes cause faster fluorescence decay. The larger values of τ_0 have also been reported previously for various phthalocyanines and in similar studies [**170**]. When a fluorophore is excited in the presence of a nearby metal it interacts with the free electrons from the metal surface and modifies the fluorescence behaviour by altering the electric

field around the molecule [**171**]. This effect can either increase or decrease the fluorescence lifetimes depending on the geometry or distance between the metal and molecule [**172**]. Therefore the excited molecule can be pictured as an oscillating dipole in which the lifetime will increase when the oscillating dipole is not in line with the reflected field and decreases when they correlate [**173, 174**]. Therefore the observed increase in τ_0 values (**Table 4.1**) when the phthalocyanine was attached on the gold surface could suggest an uncorrelated field.

4.1.2. Non-spherical gold nanoparticles

***ZnTTAPc**) (**4**) was studied in DMF because the triplet and singlet oxygen signals in DMSO were poor compared to DMF.*

The fluorescence behaviour of fluorophore in the presence of nanoparticles is affected by factors such as the size of the nanoparticle [**175**]. Hence, the effect of aspect ratio of the nanorods is investigated. The fluorescence quantum yields of **ZnTTAPc (4)** measured in the presence of gold nanoparticles are all slightly higher (**Table 4.2**) than the phthalocyanine alone in pH 9 buffer + Triton X 100 due to reduced aggregation. The presence of metallic particles can modify the local field around the fluorescing molecule by causing an increase of the rate of excitation at larger distances which would result in an increase in the quantum yield [**174**]. Fluorescence quantum yields were found to marginally increase

with increasing aspect ratio (**Table 4.2**). It has been reported that the fluorescence emission is more polarized along the length of the nanorods and the degree of polarizability by nanorods increases with their aspect ratio [**176,177**]. Hence, the increase in fluorescence quantum yields could also be due to the increasing excitation rate as the aspect ratio increases.

Figure 4.2 shows the time-resolved fluorescence decay curve for complex **2a**-**AuBP** (as an example). A bi-exponential decay was observed **4** in the presence of nanoparticles, **Table 4.2**. It can be observed that the decay time differs with different shapes of the attached gold nanoparticles (**Table 4.2**). For **2a**-AuNR (**3.2**) and **2a**-AuBPs one lifetime was observed.

Fluorescence lifetimes (τ_F) decreased (considering the long lifetime) for the smaller aspect ratio nanorods (**4**-CTAB-AuNRs (**2.0**)) when compared with the **4** alone in pH 9 + Triton X 100. The τ_F value for AuNRs (**4.7**) was the same as for **4** in pH 9 + Triton X 100, with a slight increase for AuNRs (**7.1**). The radiative lifetimes in **Table 4.2** were estimated for different sizes of the gold nanorods. It was observed that when the aspect ratio increases, τ_0 decreases. The τ_0 values can be affected by the distance and orientation between the molecule and metal particles, and can either increase or decrease depending on the molecular dipole and the distance between the fluorophore and the metal.

Both size and shape of nanoparticles can also alter the radiative decay [**178, 179**]. Higher photonic mode density increases in the presence of nanoparticles and causes a decrease in radiative decay [**173**]. The decrease in

radiative lifetime at larger aspect ratio is caused by the increasing photonic mode density. As the aspect ratio increased, the absorption of the nanoparticles also shifts towards higher wavelengths towards the absorption of the Pc hence, increasing the interference between their excited dipoles. The absorption and scattering coefficients of nanorods are also larger than that of spherical nanoparticles [**175**], therefore nanorods are expected to increase the effects felt by the Pc molecules.

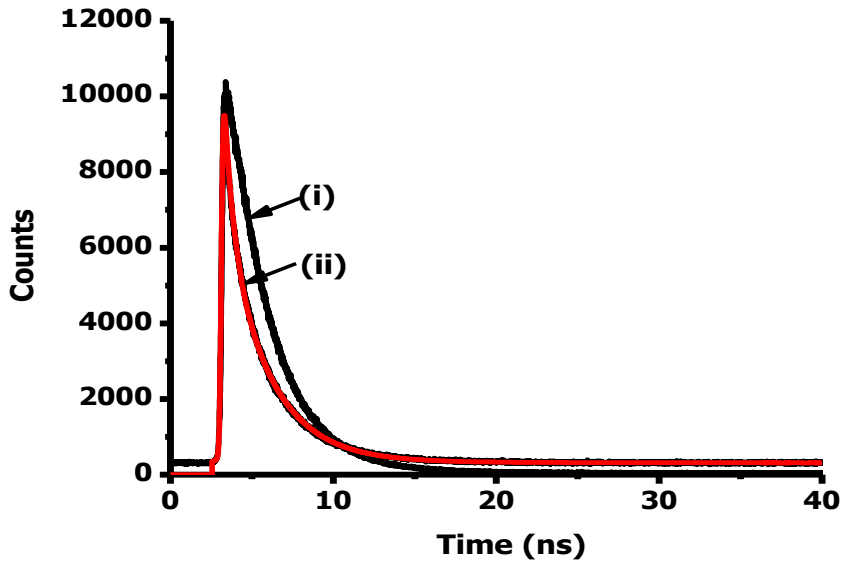

Figure 4.2: Fluorescence decay curves of (i) **2a** and (ii) **2a** –AuBPs.

Table 4.2: Summary of fluorescence properties of the phthalocyanine-non spherical AuNP conjugates.

Sample	Solvent	Φ_F ± 0.01	τ_F (ns)[a] ±0.01	τ_0 (ns)
2a	DMSO	0.12	4.99(1.0)*	41.6
2a-AuNR(3.2)	DMSO	0.07	4.46 (1)	63.7
2a –AuBP	DMSO	0.08	4.39 (1)	54.9
4	pH 9 buffer + Triton X 100)	0.01	2.71(0.94) 0.69 (0.56)	[b]293.4
4-CTAB-AuNR (2.0)	pH 9 buffer	0.03	2.64 (0.85) 0.88(0.15)	[b]79.2
4- CTAB-AuNR (4.7)	pH 9 buffer	0.05	2.71 (0.88) 0.91 (0.11)	[b]49.7
4- CTAB-AuNR (7.1)	pH 9 buffer	0.06	2.73 (0.91) 0.83 (0.09)	[b]42.7
4	DMF	0.09	2.43(1)	27.0

[a]abundances in brackets, [b]average lifetime used,* ±0.03.

4.2. Triplet quantum yields and lifetimes

Triplet decay curves were not observed for the Pc complexes in the presence of anisotropic AuNPs, probably due to the short triplet lifetime as a result of the heavy atom effect. This behaviour has been observed before for other Pc AuNP conjugates [**169**]. *However, in this work it was only observed for non-spherical nanoparticles. This could suggest that anisotropism reduces the triplet lifetime more than spherical nanoparticles.*

The triplet decay curves, **Figure 4.3** obeyed second order kinetics as expected for complexes at the concentrations above $1x10^{-5}$ M due to triplet-triplet recombination [**180**]. The complexes show an increase in the quantum yields upon conjugation showing that the presence of AuNPs favoured intersystem crossing, **Table 4.3**. This enhancement could also be the contribution of the bromide ion present in the nanoparticles from the tetraoctylammonium bromide used in the synthesis [**73**]. Compared to **3** or **3**-AuNS, Φ_T the values for for **1,2, 1a and 2a** are low due to the small size of Al and Mg, which do not encourage ISC to the triplet state as compared to zinc, even the presence of the chloride in **2** and **2a** is not enough. Φ_T for **2** and **2a** is large compared to **1** and **1a** due to the presence of the chloride in the former which encourages ISC to the triplet state. Φ_T for **4** is 0.28 and 0.21 in DMF and aqueous buffer + Triton X-100 respectively, **Table 4.3**. In aqueous the Φ_T value is lower due to aggregation.

The triplet quantum yields of the quaternized complexes (**1a** and **2a**) were almost the same as for the non-quaternized complexes (**1** and **2**) and this was due to the monomeric behaviour of these complexes in DMSO. Triplet lifetime for **4** DMF is 35 μs and 25 μs in pH 9 buffer + Triton X-100. For **3** in DMSO, it is 217 μs. The values for **4** are lower **1**, **2**, **1a**, **2a** and **3**, this could be due to the quenching of the triplet state by amino groups in complex **4** causing a faster decay.

There is a decrease in the triplet lifetime for **1a** and **2a** in the presence of AuNPs due to the presence of Au as a heavy metal, corresponding to an increase Φ_T. For **ZnPcSH (3)**-AuNPs conjugate (455 μs) was larger than that of the **3** (217 μs). The increase in the triplet lifetimes in the presence of Au nanoparticles has been regularly observed [**91**] and it could be a result of the protection of the Pc from the environment by the former.

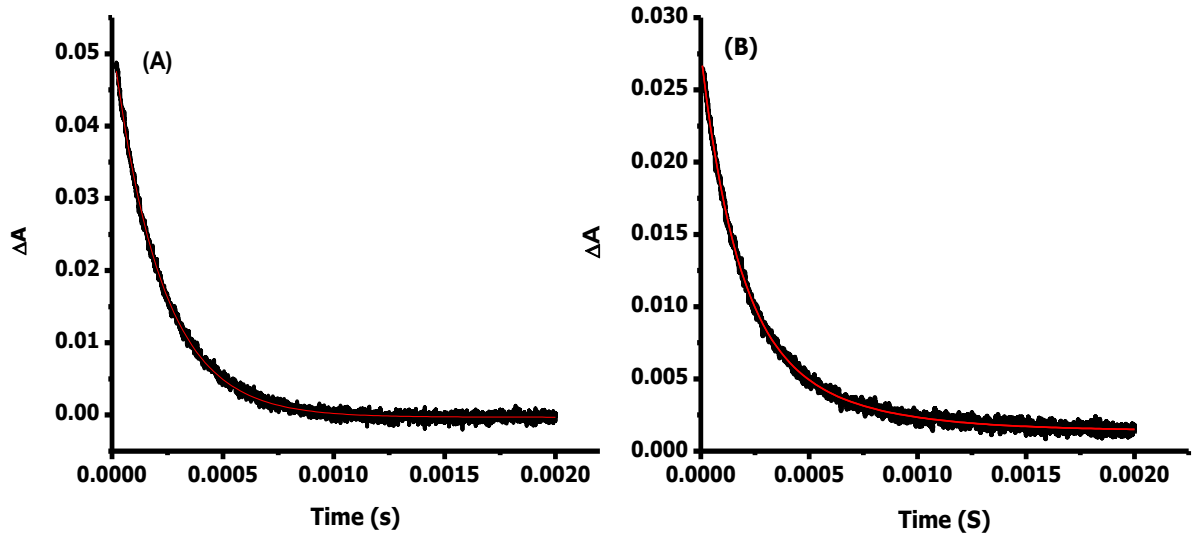

Figure 4.3: Triplet decay curves of (A) **ZnPcSH (3)** and (B) **ZnPcSH (3)**-AuNPs in DMSO.

4.3. Singlet oxygen quantum yields

Singlet oxygen is produced when photosensitizers in the excited triplet state transfer energy to the molecular oxygen. Thus singlet oxygen quantum yield (Φ_{Δ}) is the measure of the efficiency of singlet oxygen production. The photodegradation of the singlet oxygen quencher (DPBF) confirms the ability of the complexes to produce singlet oxygen.The Q-band for all the phthalocyanine complexes remained unchanged in **Figure 4.4** proving the stability of the complexes. Singlet oxygen quantum yields for unquaternized complexes are higher than for the quaternized derivatives (**Table 4.3**). This shows that quaternization caused a decrease in singlet oxygen quantum yields in DMSO.

Complexes **1** and **1a** show low singlet oxygen quantum yields due the small size of Mg. In DMF the singlet oxygen quantum yield of **4** was 0.44 while in pH 9 buffer (when Triton X-100 was added) it was 0.19, **Table 4.3**. The low Φ_{Δ} value for **4** in aqueous is due to aggregation. The singlet oxygen quantum yield for **1**, **2**, **1a** and **2a** are low due to the low triplet quantum yield compared to **3** and **4** (**Table 4.3**). Quantification of singlet oxygen in water for **1a** and **2a** was not done due to aggregation.

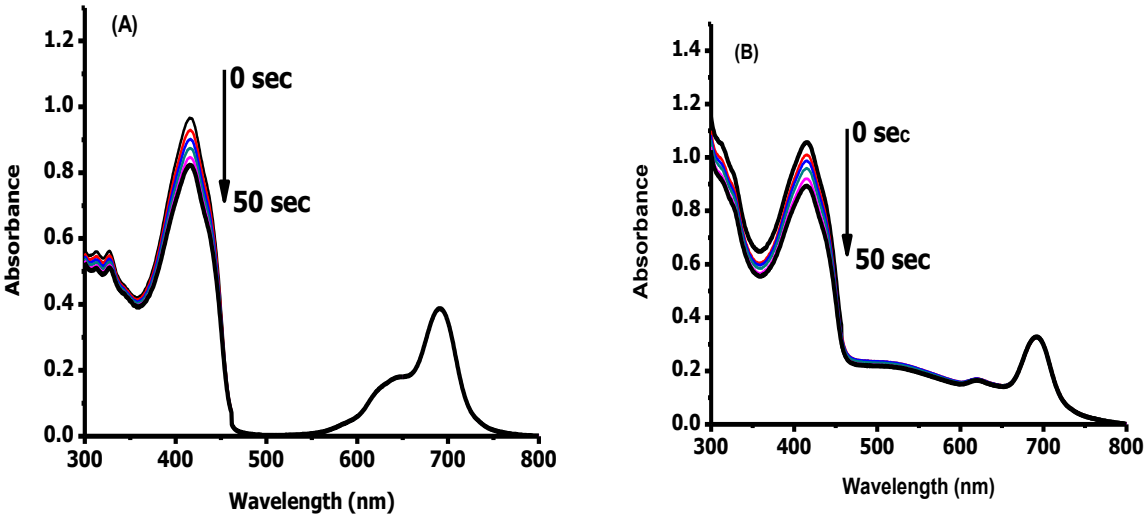

Figure 4.4: Photodegradation of DPBF in the presence of (A) **ZnPcSH** and (B) **ZnPcSH**-AuNPs in DMSO.

There is an increase in the Φ_Δ for all the complexes in the presence of AuNPS, **Table 4.3** due to heavy atom effect of gold. Heavy atoms promote intersystem crossing which result in larger single oxygen quantum yields. We observed an enhancement (compared to spherical nanoparticles, **AuNS**) in singlet oxygen quantum yields for **2a**-**AuNR (3.2)** and **2a**-**AuBP** showing advantage of asymmetry. The increase in singlet oxygen quantum yields shows that the molecule may be used for PDT applications in the presence of variously shaped AuNPs.

4-CTAB-AuNS (**1.0**) and **4**-CTAB-AuNR (**2.0**) produced the equal amounts of singlet oxygen (Φ_Δ = 0.23, **Table 4.3**). The number of Pc molecules per number of AuNP was slightly different for the two at 27 and 49 (**Table 3.5**), respectively. The amount of singlet oxygen produced from AuNR (**4.7**) at Φ_Δ = 0.25 was slightly larger than for AuNR (**2.0**) corresponding to the larger Pc molecules per AuNP at 111 and 49, respectively, (**Table 3.5**). The largest Φ_Δ value at 0.29 was observed for AuNR (**7.1**) with the largest number of Pcs per AuNPs and larger surface coverage.

Table 4.3: Summary of the photophysical and photochemical properties of the phthalocyanine complexes and the conjugates.

Complex	Solvent	Φ_T	τ_T/μs	Φ_Δ
1	DMSO	0.30	582	0.07
2	DMSO	0.46	489	0.16
1a	DMSO	0.29	720	0.06
2a	DMSO	0.46	487	0.12
1a- citrate- AuNS	DMSO	0.35	420	0. 13
2a- citrate- AuNS	DMSO	0.54	380	0.19
2a- CTAB-AuNRs (3.2)	DMSO	-	-	0.23
2a-AuBPs	DMSO	-	-	0.24
2a- CTAB-AuNPs	DMSO	-	-	0.21
3	DMSO	0.63	217	0.45
3- TOABr-AuNS	DMSO	0.84	455	0.68
4	DMF	0.28	35	0.44
4	pH9 buffer + Triton X	0.21	25	0.19

4-CTAB-AuNR (1.0)	**pH 9 buffer**	**-**	**-**	**0.23**
4-CTAB-AuNR (2.0)	**pH 9 buffer**	**-**	**-**	**0.23**
4- CTAB-AuNR(4.7)	**pH 9 buffer**	**-**	**-**	**0.25**
4-CTAB-AuNR (7.1)	**pH9 buffer**	**-**	**-**	**0.29**

4.4. Summary

The fluorescence quantum yields of the Pc complexes decreased in aqueous solutions due to aggregation in such solvents. This also resulted in a decrease in fluorescence lifetimes. The production of singlet oxygen quantum yields was dependent on the shape of the gold nanoparticles. This chapter shows that the photophysical and photochemical properties of the phthalocyanines is also affected by the aspect ratio of the AuNRs. An increase in nanorod aspect ratio resulted in higher singlet oxygen quantum yields.

Chapter 5 Photoinactivation of microorganisms

This chapter reports on the application of phthalocyanine-gold nanoparticles in Photoinactivation of Candida albicans and Escherichia coli.

5.1. Photoinactivation studies

Statistical analysis

All experiments were done separately in triplicates and the results are reported as the mean values ± standard deviation of each group. Statistical significance of more than two mean values was determined using Anova (analysis of varience) using error limits from at least three determinations. The difference between two means was compared using a student's t-test. P values < 0.05 were considered significant.

Complex 2a and its conjugates were used in the photoinactivation studies.

The photoinactivation studies in this work were performed by irradiating the **2a** alone or in the presence of AuNRs (**3.2**) at wavelength where both absorb using the photochemical set-up described in **Chapter 2**. AuBPs were also investigated even though their absorption peak does not match the absorption of **2a**. The presence of AuNRs and AuBPs towards the PACT activity of **2a** will (in addition to the possible photothermal effect of AuNRs at the excitation wavelength) also enhance singlet oxygen through the heavy atom effect, as

observed in **Chapter 4**.

5.1.1. Controls

The two control experiments were performed; (1) For the dark controls, the cells were treated complex **2a**, complex **2a-**AuNPs and AuNPs without illumination. (2) Light controls had no photositizer but illuminated. The controls did not show cytotoxicity on the microorganisms studied.

5.1.2. Photoinactivation of *Candida albicans*

PACT efficiency of complex **2a** and its conjugates with AuBPs and AuNRs (**3.2**) was evaluated by applying a power density of 92 mW/cm^2. **Figure 5.1** shows the survival curves for *C. albicans* (using complex **2a** alone without AuNPs) in which the colony forming units were measured against light fluence. The efficiency of the photosensitizers on *C. albicans* was evaluated by calculating the log reduction. The number of colony forming units (CFU) decreased with increasing light fluence. Complex **2a** alone gave 1.78 CFU log reduction ($p = 0.003$) (**Figure 5.1, Table 5.1**). For the conjugates, 2.08 ($p = 0.002$) and 2.53 logs ($p = 0.001$) reduction were achieved for complex **2a**-AuBPs and complex **2a**-AuNRs, respectively under the same conditions, **Table 5.1**. The statistical analysis showed no significance difference between the two conjugates (complex **2a**-AuBPs and complex **2a**-AuNRs) ($p = 0.33$). For

photoinactivation with AuBPs and AuNRs alone (without complex **1**), an insignificant reduction of 0.26 and 0.47 logs ($p > 0.05$), respectively, was achieved **Table 5.1** (figures not shown). Thus, the photothermal effect (for AuNPs) of the nanoparticles was negligible however, conjugation with a phthalocyanine produced an enhanced photoinactivation which may be associated with heavy atom effect of the gold nanoparticles or increased production of reactive oxygen species (ROS) catalysed by gold nanoparticles.

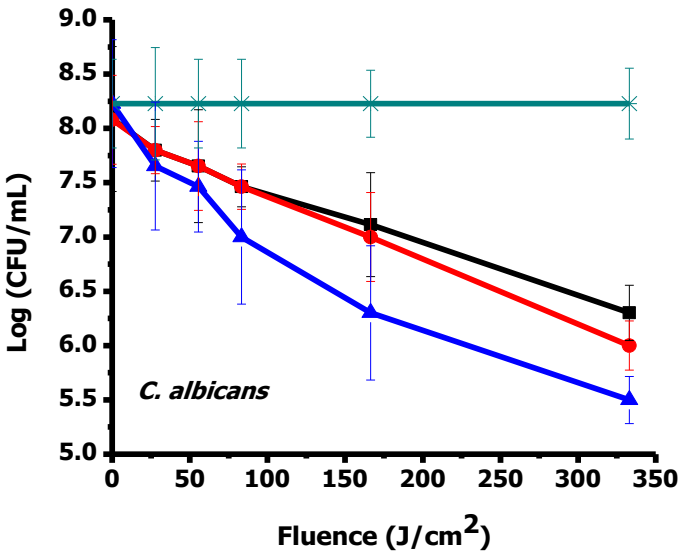

Figure 5.1: Survival curves of (A) *C. albicans;* irradiance **92 mW/cm²** (■)complex **2a** alone, (●)**2a**-AuBPs, (▲)**2a**-AuNRs and (x) Light control (with light in the absence of complex **2a** or its conjugates); Values represented mean ± standard deviation of three independent experiments.

5.1.3. Photoinactivation of *E. coli*

Fig. 5.2 (B) shows survival curve for *E. coli* after photoinactivation with **2a**. Complex **2a** is a cationic molecule and is expected to bind the cell wall of the gram negative *E coli*. A statistically significant 2.51 log reduction ($p = 0.03$) was obtained for **2a** alone, (**Table 5.1**). For **2a**-AuBPs and **2a**-AuNRs (**3.2**) the log reduction increased to 3.34 ($p = 0.004$) and 3.71 ($p = 0.001$) respectively, **Table 5.1** (**Fig. 5.2**). The results showed a significant increase in the reduction of *E. coli* in the conjugates compared to the complex **2a** alone. The p value analysis showed insignificant difference between the two conjugates (complex **2a**-AuBPs and complex **2a**-AuNRs) ($p = 0.25$). Insignificant log reduction 0.68 and 0.77 ($p > 0.05$) were obtained for AuBPs and AuNRs (**3.2**), (gold nanoparticles without complex **2a**), respectively **Table 5.1** (**Figures not shown**).

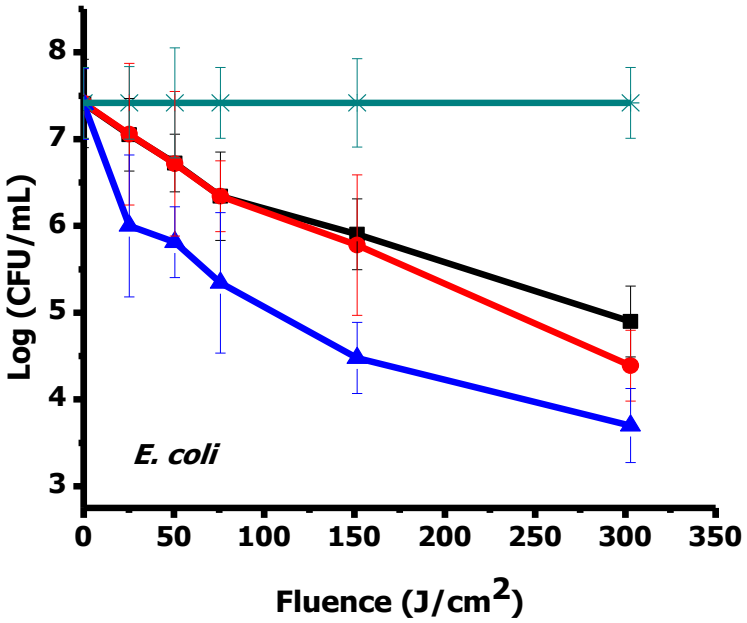

Figure 5.2: Survival curves of (A) *E. Coli;* irradiance = **84mW/cm²** (■)complex **2a** alone, (●)**2a**-AuBPs, (▲)**2a**-AuNRs and (x) Light control (with light in the absence of complex **2a** or its conjugates); Values represented mean ± standard deviation of three independent experiments.

5.2. Discussion

It can be noted that even though AuNRs (**3.2**) absorb within the wavelength used for excitation (670 ± 40 nm) in this work, they did not show any significant results of photoinactivation on their own. However, upon conjugation with complex **2a** there was enhanced photoinactivation of the bacteria. The conjugates gave a significantly higher log reduction ($p < 0.05$)

compared to complex **2a** alone in both bacteria and fungi. This shows that AuNPs enhanced the photoinactivation process. AuNPs used in this study were found to enhance the photoinactivation process in both bacteria and fungi irrespective of their shape. Even though complex **2a**-AuNRs gave slightly larger log reduction compared to complex **2a**-AuBPs the statistical analysis showed no significant difference in the results. In the absence of the phthalocyanine the nanoparticles did not show any photothermal effect. It has been reported that anisotropic NPs possess long circulation time in biological media [**181**], hence these nanoparticles are suitable for PACT studies. *C. albicans* cells contain a rather thick layer of chitin and β–glucan which makes the penetration of the photosensitizers difficult, hence lower log values [**182**].

Table 5.1: Summary of Log CFU values

Photosensitizer	*C. albicans*	*E. coli*
AuBPs	**0.26 (p > 0.05)**	**0.68 (p > 0.05)**
AuNRs(3.7)	**0.47 (p > 0.05)**	**0.77 (p > 0.05)**
complex 2a	**1.78 (p = 0.003)**	**2.51(p = 0.03)**
2a-AuBPs	**2.08 (p = 0.002)**	**3.34 (p = 0.004)**
2a-AuNRs	**2.53 (p = 0.001)**	**3.71 (p = 0.001)**

5.5. Summary

*The conjugates of aluminium phthalocyanine (complex **2a**) with gold nanorods (complex **2a**-AuNRs) and bipyramids (complex **2a**-AuBPs) were used for the photoinactivation of fungi (C. albicans) and bacteria cells (E. coli). The efficiency of these conjugates was evaluated by measuring the log reduction of the microorganisms (C. albicans and E. coli) after irradiation with visible light in the presence of the photosensitizers. The significance of the results was evaluated by p value evaluation. Significant log reductions were achieved with the conjugates demonstrating improved photoinactivation compared to Pc alone. The statistical analysis of the*

results showed that the enhanced photoinactivation observed in both microorganisms was irrespective of the shape of the nanoparticles conjugated. Photoinactivation of C. albicans was less than for E. coli even though a higher concentration of ***2a*** *or its conjugates was used in C. albicans.*

Chapter 6
Iron protophoryrin IX binding to metallothionein

This chapter reports on the attempted work on Iron Protoporphrin IX (PPIX) chloride binding in apo-alpha metallothionein protein by Ion Spray Mass Spectrometry. This work was done in Canada.

6.1. Introduction

Metallothioneins (MTs) (**Figure 6.1**) are cysteine rich proteins with a molecular weight of about 6-7 kDa [**183**]. The ability of the MTs to bind divalent heavy metals has made them a huge subject of investigations over the years [**184-186**]. MTs play a very important role in protecting the cells against toxic heavy metals such as cadmium, mercury and arsenic [**187, 188**]. The MT structure is made of the alpha and the beta domains with each containing 11 and 9 cysteins respectively [**189**]. The amino acid sequence of the alpha domain is GSMGKAAAAC CSCCPMSCAK CAQGCVCKGA SEKCSCCKKA AAA and for the N-terminus S-tag is MKETAAAKFE RQHMDSPDLG TLVPRGS. Metallothioneins exist as either metal free (apo) or metallated forms.

Porphyrins are tetrapyrrolic structures in which the four pyrrole rings are bound together through *meso* carbons. Porphyrins can be characterized by a strong absorption band (Soret band) between 390-425 nm and the Q-bands around 480-700 nm [**190**].Protoporphrin IX (PPIX) is a porphyrin compound that can be found in heamoglobin and myoglobin proteins.

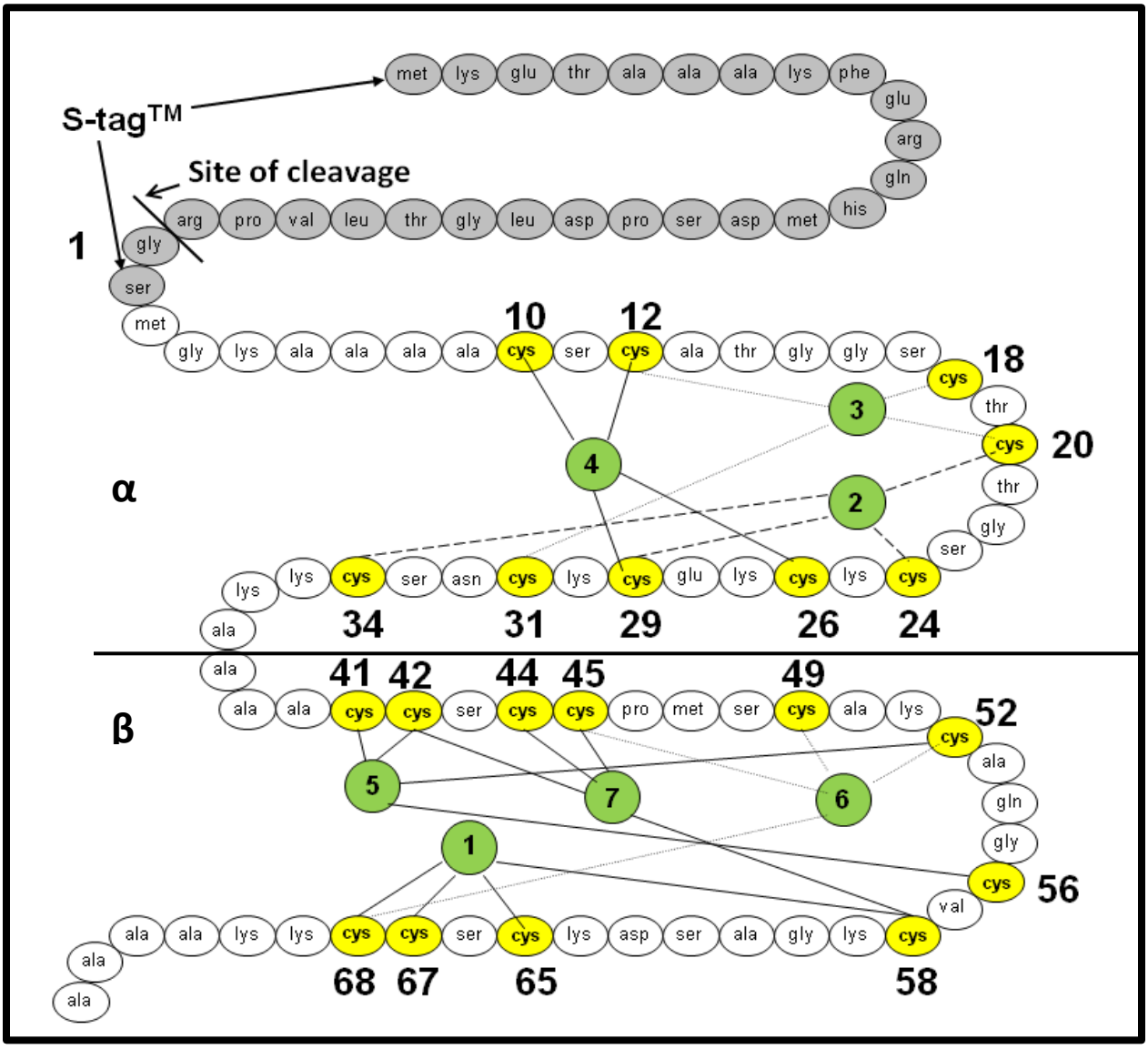

Figure 6.1: Amino acid sequence of Recombinant human-MT αβ domain.

In this study we attempted to bind Iron Protoporphrin IX (PPIX) (**Figure 6.2**) with apo-αMT for the first time. The axial binding is expected between the iron of the heme and thiol groups of the MT. The binding was tracked using ESI-MS spectrometry. Studies of heme binding proteins date back in the 1950s and

myoglobin was the first heme protein to be investigated [**191**]. Myoglobin and hemoglobin are the most popular heme binding proteins to have been studied. This led to intensive investigations on heme protein structural properties and the design of new such structures [**192-194**].

The interaction of proteins with drugs facilitates drug delivery throughout the body. Protoporphrin IX (PPIX) derivatives were the first generation photosensitizers to be studied in photodynamic therapy (PDT) currently in clinical trials [**195**]. The study of **FePPIX**-Metallothionein binding could lead to the formation of a new delivery system. MT has been discovered in various tumour cells [**196**]. Thus, it can be used to deliver **FePPIX** to cancerous cells. The study of heme binding to metallothionein would give an insight of the possible interaction and would help in future studies of heme binding proteins.

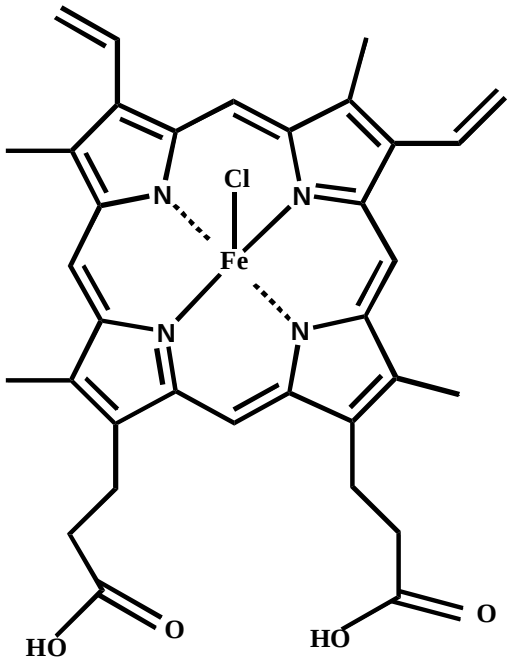

Figure 6.2: Structure of Iron Protoporphrin IX (PPIX).

6.2. Experimental

6.2.1. Materials

Iron Protoporphrin IX (PPIX) was purchased from Frontier Scientific, Sephadex G-25 (Fine Biotech) was purchased from Amersham Biosciences. Fresh solutions of iron protoporphrin IX (PPIX) (1 mM) were used for each experiment and were used shortly after preparation.

6.2.2. Preparation of Apo-αMT

Apo-αMT was synthesized following the methods reported by Duncan and Stillman for metal bound and metal free MT [**197**]. Apo-MT is metal free form of metallothionein protein and can be obtained from demetallation of Cd bound MT. Briefly metal-free apo-αMT was prepared by eluting the thrombin-cleaved Cd-bound protein from a G-25 column equilibrated with a low-pH eluent (formate buffer). Apo-αMT was eluted with deionized water adjusted with formic acid (HCOOH) to pH 2.8. Elution of the protein with a low-pH eluent effectively removes the metal ions from the protein. It separates from the protein band through the size-exclusion processes on the column. Preparation of apo-αMT by this method simultaneously desalts the solution by the same size-exclusion process. As MT is devoid of aromatic amino acids, the metal-free protein fractions were detected by UV absorption at 220 nm, which corresponds to the electronic transitions generated by the polypeptide backbone. The final samples were thoroughly evacuated and Ar-saturated to remove the bulk of the oxygen from the solutions, in order to prevent oxidation of the metal-free protein.

Titration of FePPIX into Apo-αMT: A buffered solution of metallothionein was put under argon for 3 min to remove oxygen. **FePPIX** was titrated into a solution of apo-αMT in a tightly closed vial.

6.2.3. Equipment

(i) ESI-MS data: A Bruker microTOF II ESI-TOF mass spectrometer (Bruker, Canada) operated in the positive mode was used for all ESI-MS measurements. Samples were infused into the spectrometer at a rate of 300 μLh^{-1} using a microliter infusion pump. The instrument was calibrated with an external NaI/CsI standard solution. Data were processed using the Bruker Data Analysis 4.0 software and deconvoluted using Maximum Entropy deconvolution procedure. **Parameters**: nebulizer = 2.0 bar, dry gas temp = 473 K, rolling average = 2 × 0.5 Hz, end plate offset = -500 V, capillary voltage = 4500 V, flow rate = 6.0 L/min, capillary exit = 225 V, hexapole = 23.0V, hexapole rf = 425 Vpp and skimmer 1= 42 V.

(ii) Spectrophotometric studies: Absorption data was obtained from a dual beam UV-visible absorption spectrometer. (Cary 500, Varian Canada).

(iii) MCD data was measured was recorded at 5.15 Tesla using the Oxford Instruments SM2 superconducting magnet and a CD spectrometer based on a JASCO J810 spectrometer. All samples were dissolved in DMF and the MCD spectrum was measured in a 1 cm cell.

6.3. Results and discussion

6.3.1. Spectral characterization of FePPIX

Figure 6.3 (A) shows the UV-Visible absorption spectrum of the **FePPIX** in DMF. The spectrum of **FePPIX** shows a B or Soret band maximum at 404 nm and other four bands in the visible region. The observed bands in the visible region (501 nm, 538 nm, 574 nm and 624 nm) are due to the Q and charge transfer bands. The spectrum is typical of a monomeric species and does not show any aggregation.

The MCD spectroscopy was used to support the data obtained from the UV-Vis absorption. The MCD spectrum **Figure 6.3 (B)** shows a pseudo-*A* term between 402 to 421 nm. There are about five other bands in the visible region, this behaviour is known for ferric heme compounds, and it is due to the charge transfer bands that overlap with the Q bands [**198**].

Figure 6.4 show that **FePPIX** exists as three different species in solution. The most intense signal observed is the monomer (**FePPIX**) followed by a dimer $(\mathbf{FePPIX})_2$ then the smallest being a trimer $(\mathbf{FePPIX})_3$.

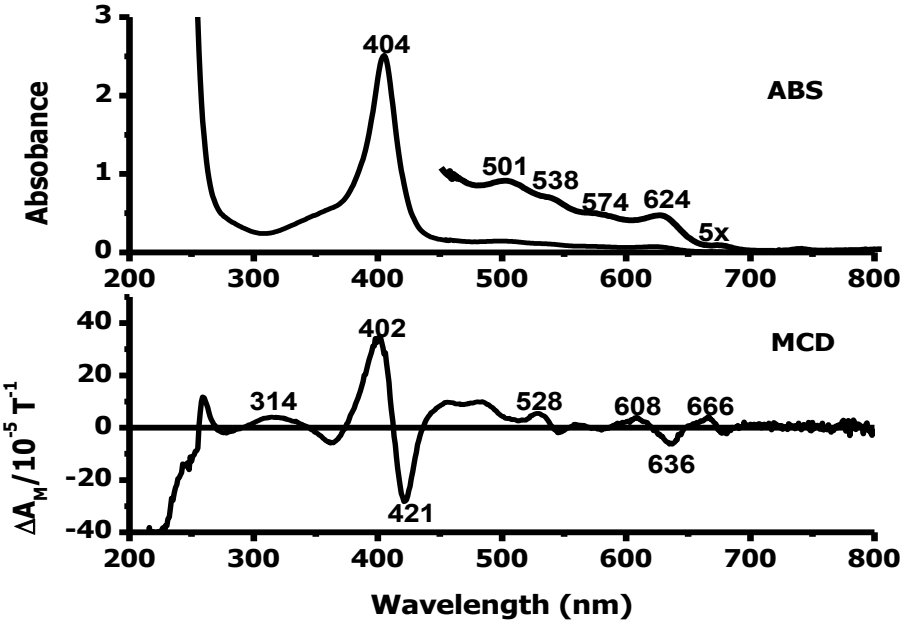

Figure 6.3: UV-Visible absorption and MCD spectra of Ferriprotoporphyrin (ix) chloride.

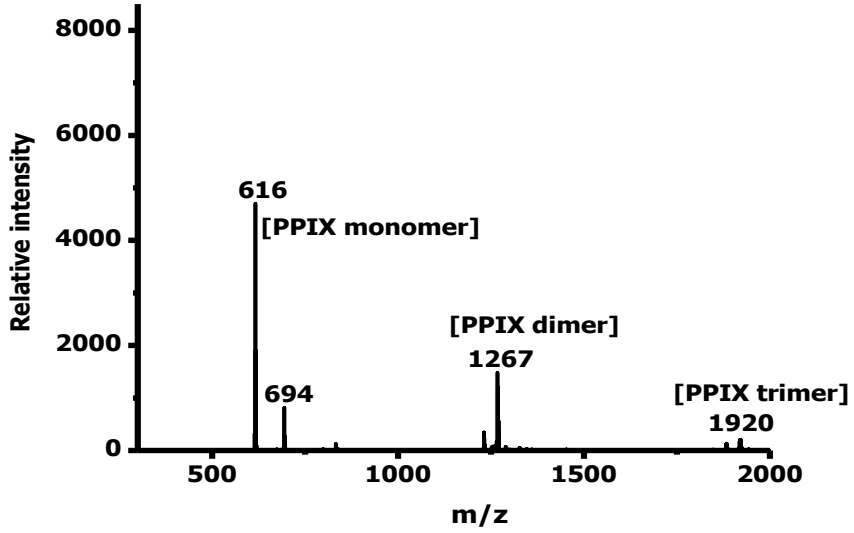

Figure 6.4: High resolution ESI mass spectral data of **FePPIX** in MeOH.

6.3.2. Characterization Apo-α MT

Mass spectrometry can provide both qualitative and quantitative information about the analytes. ESI-MS is a very important technique in clinical laboratories that is used to study biological samples. Samples can be analyzed in various solvents, temperatures and pH [**199**].

Analysis of molecules using the mass spectrometer involves a number of stages (**Figure 6.5**); (i) the conversion of analytes into gas phase (ii) the separation of the molecular ions based on their mass to charge ratio (*m/z*), (iii) detection of the ions and (iv) the mass spectrum computer display [**200, 201**]. Mass spectrometry has been used to study metallothionein binding [**202-204**]. Charge states show distribution of monoisotopes in large molecules whereas the average mass of the molecules can be shown on the deconvoluted spectrum.

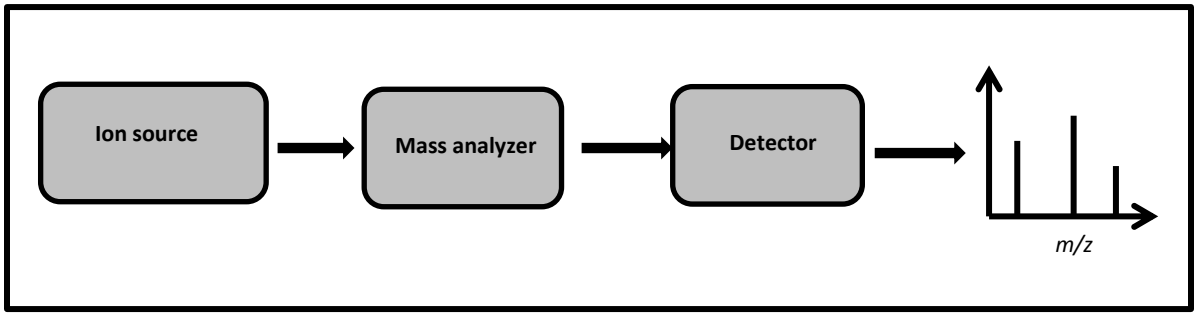

Figure 6.5: Schematic representation of a mass spectrometer.

The ESI-mass spectrometer was used as the main technique to study the protein and the protein binding with the iron protoporphyrin IX (**FePPIX**) chloride complex. **Figure 6.6 (A)** shows the mass spectrometer of the apo -αMT which showed two characteristic peaks, at 3749 and 6892 Da, **Figure 6.6 A** corresponding to the mass of apo-αMT without and with the tag respectively.

Benzoquinone (BQ) binds easily to thiol groups and thus, it was used to bind to bind apo-αMT in formate buffer (**pH 7.4**) as test to count the thiol groups on the protein. ESI mass spectroscopy was used to track the binding of BQ to apo-αMT. The observed charge states match the mass of the apo-αMT in the deconvoluted spectrum. The deconvoluted spectrum in **Figure 6.6** shows a mass of 4921 Da corresponding to the binding of 9 BQs. This shows the availability of 9 thiol groups on apo- MT.

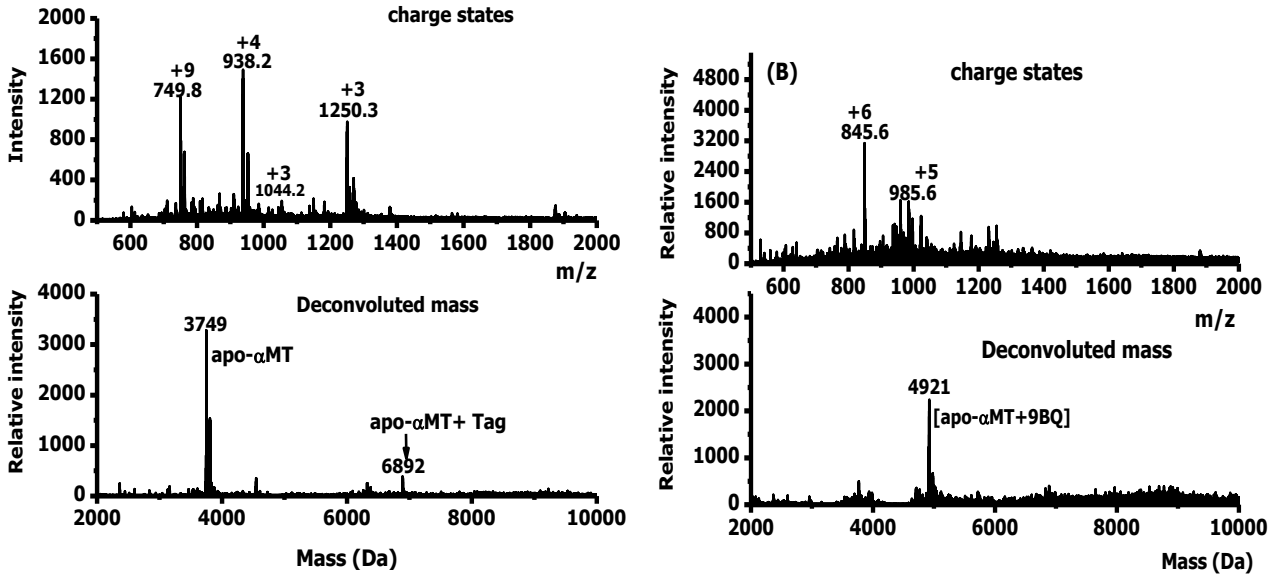

Figure 6.6: High resolution ESI mass spectral data of alpha apo-αMT protein at pH 7.4, (A) apo-αMT and (B) apo-αMT + BQ.

6.3.3. The pH dependent Protoporphyrin IX binding

FePPIX was titrated into a solution of apo-αMT at pH 2, pH 5, pH 8 and pH 9 (**Figure 6.7**). There was no binding observed at pH 2 and pH 5. At pH 8 and pH 9 the deconvoluted spectra show *m/z* signals corresponding to Apo-αMT- $(FePPIX)_6$ (7608 Da) rings at both pH values. The results show that the binding of FePPIX was pH dependent and FePPIX only binds apo-αMT at high pH. The major charge states in Apo-αMT spectra correspond to the mass of Apo-αMT. This shows that most of the Apo-αMT was not bound to the heme rings.

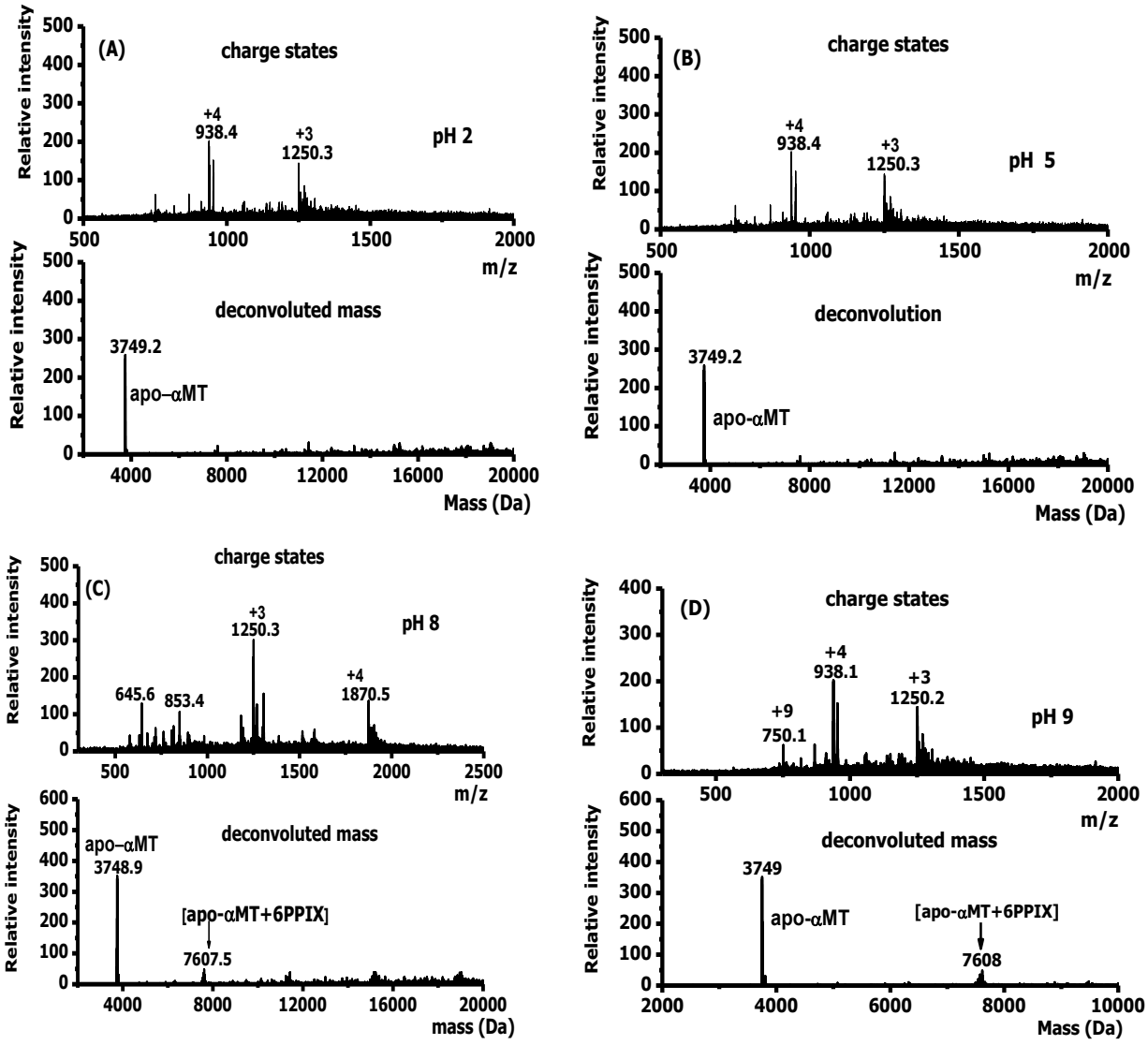

Figure 6.7: FePPIX binding to apo-αMT at (A) pH 2, (B) pH 5, (C) pH 8 and (D) pH 9 (deconvoluted spectra included).

6.3.4. Concentration dependent Protoporphyrin IX binding

Different amounts (50 µL, 100 µL, 200 µL and 400 µL) of FePPIX were titrated in the solution of apo-αMT at high pH (**pH 8**). **Figure 6.8** shows that there was no binding of the FePPIX when titrating with 50 µL and 100. At 200 µL, the *m/z* signal corresponding to 6 FePPIX rings was observed. At 400 µL there was excess of free FePPIX as evidenced by the *m/z* signal at 616.2 in the charge state spectrum. The *m/z* signal 616.2 is the mass of the FePPIX and the appearance of this signal shows that the apo-αMT was saturated and could not bind more FePPIX rings thus were in excess. However, heme bound apo- αMT signals are very small and the free apo-αMT is observed as a major species in all the studied conditions.

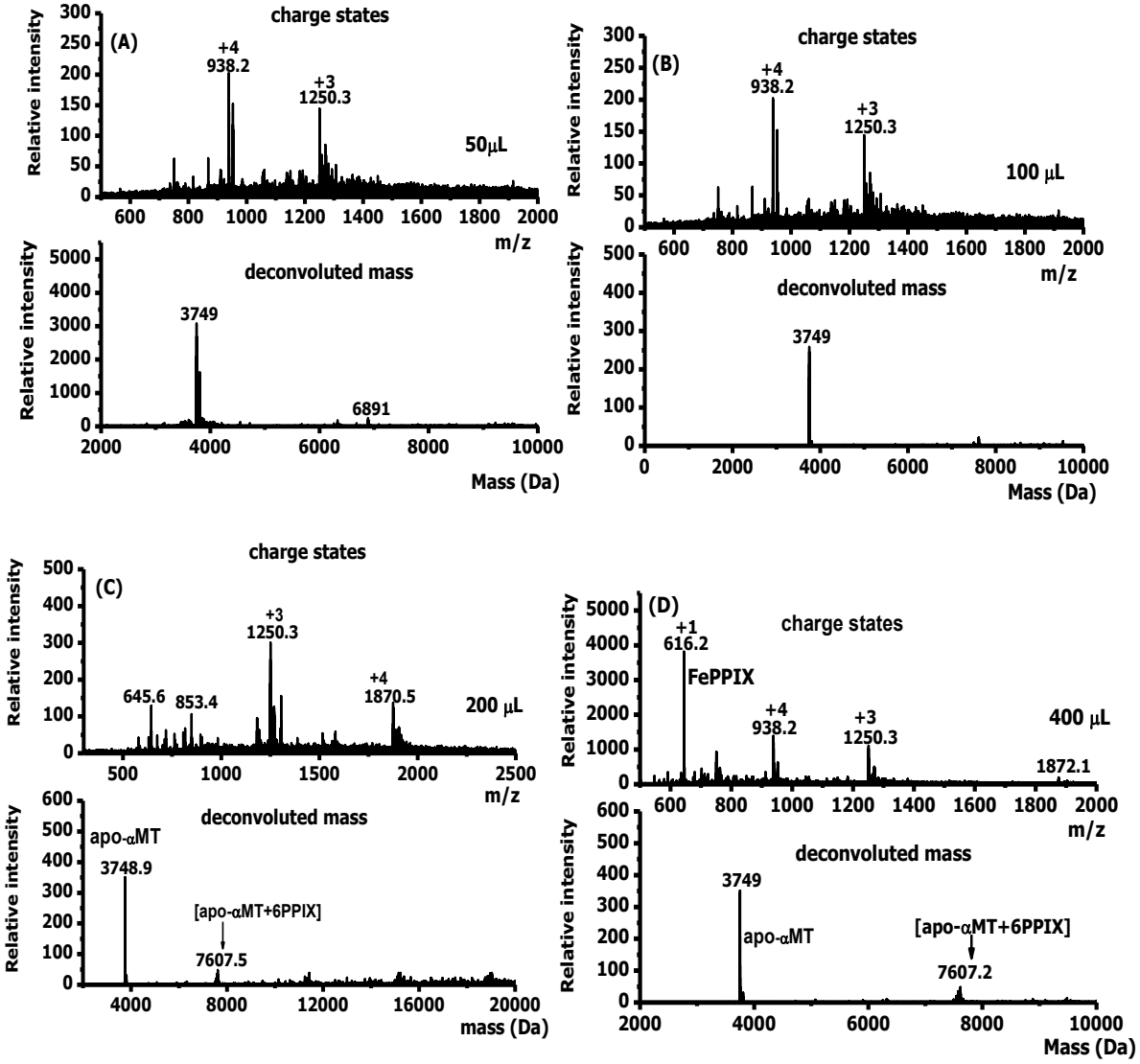

Figure 6.8: FePPIX binding to MT at pH8 (a) 50 μL, (b) 100 μL, (c) 200 μL and (d) 400 μL.

6.5. Summary

Metallothionein (apo - αMT) was successfully synthesized and the structure was confirmed using the ESI mass spectrometry. Benzoquinone was successfully used to confirm the 9 thiol groups present in the protein. The study shows that the binding of ***FePPIX*** *took place only at higher pH. It was also shown that apo - αMT can bind only 6* ***FePPIX*** *rings at the given conditions.* Apo-αMT *was observed in all binding spectra as the major species as compared to the heme bound* apo-αMT.

Chapter 7
General conclusions and Recommendations

7.1. General conclusions

Gold binding MPcs were successfully synthesized and characterized. The absorption, excitation and fluorescence properties of these compounds were studied. The complexes conjugated with AuNS showed a blue shift in their absorption spectra. The UV-Vis spectra of the conjugates containing shaped AuNPs showed red shifts of Q-band compared to the Pc alone. Aggregation of the synthesized complexes caused their fluorescence quantum yields to decrease in aqueous solvents. AuNPs were successfully conjugated to phthalocyanines via the ligand exchange method. The conjugates were characterized by the sudden appearance of the SPR band on the absorption spectra of the conjugates.

The presence of gold nanoparticles caused a decrease in the fluorescence quantum yields and lifetimes and higher singlet oxygen quantum yields. The production of singlet oxygen quantum yields was dependent on the shape of the gold nanoparticles as shown by different results obtained from different shapes. AuNRs gave larger values of singlet oxygen quantum yields as compared to other shapes studied in this work. This work also showed that the aspect ratio of the AuNRs affects the photophysical and photochemical properties of the phthalocyanines. Singlet oxygen quantum yields increased as the aspect ratio of the nanorods increased.

The study shows the potential of Pcs-AuNPs conjugates in photodynamic inactivation of micoorganisms such as bacteria and fungi. There was an

improved photoinactivation by increasing the log reduction of both bacteria and fungi in the presence of gold nanoparticles. AuNPs alone did not show photothermal effects. The study shows that photoinactivation of *E. coli* was less difficult as compared to *C. albicans*. However, the study does not show any difference between AuBPs and AuNRs on the photoinactivation of micoorganisms. The study shows that AuNPs can be used to enhance photoinactivation of microorganisms even in aggregated phthalocyanines.

7.2. Recommendations

The use of AuNPs in combination therapy is a promising fast growing field hence, the development of MPcs-nanopartices is crucial. AuNPs have captured a lot of attention due to their biocompatibility. Literature shows that most of the studies have been based on simple spherical AuNPs however, there are few on anisotropic gold. The optical properties of AuNPs are greatly affected by their shape, hence the design of conjugates with anisotropic AuNPs needs to be given attention. A large number of shapes such as stars, cubes, nanoshells and many others can be conjugated to MPcs. These NPs can be functionalized with biocompatible binding ligands that will facilitate their binding to MPcs.

These conjugates have shown a potential in photodynamic antimicrobial chemotherapy. A lot of studies can be done to improve the effectiveness of this therapy using phthalocyanine-anisotropic gold nanoparticles.

References

1. J. Park, J. Joo, S. G. Kwon, Y. Jang and T. Hyeon, *Angew. Chem. Int. Ed.*, 46 (2007) 4630.

2. A. L. Rogach, D. V. Talapin, E. V. Schevichenko, A. Kornowski, M. Haase and H. Weller, *Adv. Funct. Mater.*, 12 (2002) 653.

3. A.P. Pollard, C. Heron, in *Archaeological Chemistry RSC*, 1996, Chapter 5.

4. M. Faraday, *Philos. Trans.*, 147 (1857)145.

5. J. Turkevich, P. C. Stevenson and J. Hillier*, Discuss. Fara. Soc.*, 11 (1951) 55.

6. R. Narayanan and M. A. EI-Sayed, *J. Phys. Chem. B*, 109 (2005) 12663.

7. K. Kneipp, H. Kneipp, I.Itzkan, R. R. Dasari and M. S. Feld, *Chem. Rev.*, 99 (1999) 2957.

8. A. K. R. Lytton-Jean, H. S. Han and C. A. Mirkin, *Anal. Chem.*, 79 (2007)6037.

9. E. Boisselier and D. Astruc, *Chem. Soc. Rev.*, 38 (2009) 1759.

10. S. Encina and M. A. EI-Sayed, *Int. Rev. Phys. Chem. C*, 111 (2007) 16796.

11. H. Zhang, H. Cui, S. Yao, K. Zhang, H. Tao and H. Meng, *Nanoscale Res.Lett.*, 7 (2012) 853.

12. V. F. Puntes, D. Zanchet, C. K. Erdomez and A. P. Alivisatos, *J. Am. Chem. Soc.*, 124 (2002) 12874.

13. J. E. Millstone, G. S. Metraux and C. A. Mirkin, *Adv. Mater.*, 16 (2006) 1209.

14. J. E. Millstone, S. Park, K. L. Shuford, L.Qin, G. C. Schatz, C. A. and Mirkin, *J. Am. Chem. Soc.*,127 (2005) 5312.

15. C. S. Ah, Y. J. Yun, H. J. Park, W. J. Kim, D. H. Ha and W. S. Yun, *Chem. Mater.*, 17 (2005) 5558.

16. Y. N. Xia, W. Y. Li, C. M. Cobley, J. Y. Chen, X. H. Xia, Q. Zhang, M. X. Yang, E. C. Cho and P. K. Brown, *Acc. Chem. Res.*,44 (2011) 914.

17. C. L. Nehl, H. Liao and J. H. Hafner, *Nano. Lett.*, 6 (2006) 683.

18. T. K. Sau and C. J. Murphy, *J. Am. Chem. Soc.*, 126 (2004) 8648.

19. M. Brust. M. Walker, D. Bethell, D. J. Schiffirin and R. Whyman, *J. Chem. Soc. Chem. Commun.*, (1994) 801.

20. G. Frens, *Nature*, 241 (1973) 20.

21. J. Wiesner and A. Wokaun, *Chem. Phys. Lett.*, 157 (1989) 569.

22. B. Nikoobaht and M. A. EI-Sayed *Chem. Mater.*, 15 (2003)1957.

23. N. R. Jana, L. Gearheart and C. J. Murphy, *J. Phys.Chem. B*, 105 (2001) 4065.

24. Y. Jun, J. Choi and J. Cheon, *Angew. Chem. Int. Ed.*, 45 (2002) 3414.

25. L. Manna, E.C. Scher and A. P. Alivisatos, *J. Am. Chem. Soc.*, 122 (2000) 12700.

26. A. Gole and C. J. Murphy, *Chem. Mater.*, 16 (2004) 3633.

27. C. J. Orendorff and C. J. Murphy, J. *Phys. Chem.*, B, 110 (2006) 3990.

28. B. Nokoobakht and M. A. E I-Sayed, *Langmuir*, 17 (2001) 6368.

29. C. J. Johnson, E. Dujardin, S. A. Davis, C. J. Murphy and S. Mann, *J. Mater. Chem.*, 12 (2002) 1765.

30. S. Link, and M.A. EI-Sayed, *J. Phys. Chem. B*, 103 (1999) 8410.

31. M. Z. Liu, and P. Guyot-Sionnest, *J. Phys. Chem. B*, 109 (2005) 22192.

32. L. Ruan, C. Chiu, Y. Li and Y. Huang, *Nano Lett.*, 11 (2011) 3040.

33. H. M. Cheng, R. Liu and D. P. Tsai, *Cryt. Growth Des.*, 9 (2009) 2079.

34. A. von Braun and J. Tcherniac, *Ber. Deut. Chem. Ges.*, 40 (1907) 2709.

35. R. P. Linstead. *J. Chem. Soc.*, 6 (1934) 1016.

36. C. E. Dent and R. P. Linstead, *J. Chem. Soc.*, 215 (1934) 1027.

37. A. R. Lowe and R. P. Linstead, *J. Chem. Soc.*, 214 (1934) 1022.

38. J. M .Robertson, *J. Chem. Soc.*, (1936) 1736.

39. J. M .Robertson, *J. Chem. Soc.*, 615 (1935) 1195.

40. M. Durmus, H. Yaman, C. Gol, V. Ahsen and T. Nyokong, *Dyes Pigm.*, 91 (2011) 153.

41. V. H. C. Silva, L. T. F. M. Camargo, H. B. Napolitano, C. N. Perez and A. J. Camargo, *J. Mol. Graphics Model*. 29 (2010) 206.

42. G. Guillard, J. Simon and J. P. Germain, *Coord. Chem. Rev*. 180 (1998) 1433.

43. M. Hanack, T. Schneider, M. Barthel, J. S. Shirk, S. R. Flom and R. G. S. Pong, *Coord. Chem. Rev*. 235 (2001) 219.

44. I. Okura in: *Photosensitization of Porphyrins and Phthalocyanines*, *Gordon and Breach publishers, Germany* (2001).

45. Y. Rio, M. S. Rodriguez-Morgade and T. Torres, *Org. Biomol.*, 6 (2008) 1877.

46. P. C. Minor, M. Gouterman and A.B.P. Lever, *Inorg. Chem.*, 24 (1985) 1894.

47. T. Nyokong, Z. Gasyna and M.J. Stillman, *Inorg. Chem.*, 26 (1987)1087.

48. M. G. Cory, H. Hirose and M. C. Zerner, *Inorg. Chem.*, 34 (1995) 2969.

49. B. R. Hollebone and M. J. Stillman, *J. Chem. Soc., Faraday Trans*. II,74 (1978) 2107.

50. A. Henniksson, B. Roos and M. Sundbom, *Theoret. Chim. Acta*, 27 (1972) 303.

51. A. B. Lever, *Adv. Inorg. Radiochem.*, 7 (1965) 27.

52. C. C. Leznoff and A. B. P. Lever (Eds), *Phthalocyanines: Properties and Applications*, vol 1-4 (1991).

53. M. K. Engel and Kawamura, *Rikagaku Kenkyusho Hokoku*, 1996 (1997) 11.

54. J.M. Kroon, R. B.M. Koehorst, M. van Dijk, G. M. Sanders and E.J. R. Sudholter, *J. Mater. Chem*. 7 (1997) 615.

55. A. Eisfeld and J. S. Briggs, *Chem. Phys*., 324 (2006) 376.

56. H. Engelkamp and R. J. M. Nolte, *J. Porphyrins Phthalocyanines*, 4 (2000) 454.

57. M.S. Rodríguez-Morgade, G. de la Torre and T. Torres, in The Porphyrin Handbook, K.M. Kadish, R. Guillard and K.M. Smith *(Eds.), Academic Press, Elsevier Science*, Vol. 15 (2003) Chapter 99.

58. A. Louati, M.E.I. Meray, J.J. Andre, J. Simon, K.M. Kadish, M. Gross and A. Giraurdeau,, *Inorg. Chem.*, 24 (1985)1175.

59. P. Erk and H. Hengelsberg, *The Porphyrin Handbook:* Phthalocyanine *synthesis*, (*Eds. K.M. Kadish, K.M. Smith. R. Guilard), Academic Press, New York*, 19 (2003).

60. K. M., Smith and K. M., Guilard, R., *Eds.; Academic Press: New York*, 16 (2003) 1.

61. T. M. Keller, T. R. Price and J. R. Griffith, *Synthesis*, 8 (1980) 613.

62. C. C. Leznoff, C. R. MacArthur and Y. Qin, *Can. J. Chem*, 71 (1995) 1319.

63. S. V. Kudrevich, H. Ali and J. E. van Lier, J. Chem. Soc., *Perkin Trans.*, 1 (1994) 2767.

64. H. Ali and J.E. van Lier, *Chem. Rev*. 99 (1999) 2379.

65. N. Sekkat, H. van den Bergh, T. Nyokong and N. Lange, *Molecules* 17 (2012) 98.

66. K. I. Ozoemena and T. Nyokong, *Inorg. Chem., Comm.*, 6 (2003) 1192.

67. M. C. G. Vior, L. E. Dicellio and J. Awruch, *Dyes Pigm.,* 83 (2009) 375.

68. B. Ogunsipe, M. Durmus, D. Atilla, A. G. Gurek, V. Ahsen and T. Nyokong, *Synth. Met.*, 158 (2008) 839.

69. Z. Li and Lieberman, *Langmuir*, 17 (2001) 4887.

70. M. Idowu and T. Nyokong, *Polyhedron,* 28 (2009) 416.

71. M. Idowu and T. Nyokong, *Spectrochim. Acta.*, A, 75 (2010) 411.

72. I. A. Akinbulu and T. Nyokong, *Polyhedron*, 28 (2009) 2831.

73. D.C. Hone, P.I. Walker, R. Evans-Gowing, S. FitzGerald, A. Beeby, I. Chambrier, M. J. Cook and D. A. Russell, *Langmuir,* 18 (2002) 2985.

74. M. Camerin, M. Magaraggia, M. Soncin, G. Jori, G, M. Moreno, I. Chambier, M.J. Cook and D.A. Russell, *Eur. J. Cancer,* 46 (2010) 1910.

75. N. Nombona, E. Antunes, C. Litwinski and T. Nyokong, *Dalton Trans.*, 40 (2011) 11876.

76. M. Göksel, M. Durmuş and D. Atilla, *J. Porphyrins Phthalocyanines*, 16(2012) 895.

77. C. Liang, *Biochem. J.*, 82 (1962) 429.

78. D. R. Arnold, N. C. Baird, J. R. Bolton, J. C. D. Brand, P. W. M. Jacobs, P. de Mayo and W. R. Ware, *Photochemistry: An Introduction, Academic Press, New York*, (1974).

79. Y. Shimizu and T. Azumi, J. Phys. Chem., 86 (1982) 22.

80. S. Frey-Forgues and D. Lavabre, J. *Chem. Educ*. 76 (1999) 1260.

81. A. Ogunsipe, J. Y. Chen and T. Nyokong, *New J. Chem*. 28 (2004) 822.

82. R. O. Ogbodu, E. Antunes and T. Nyokong*, Dalton Trans.*, 42 (2013), 10769.

83. C.D Geddes and J.R. Lakowicz, in *Topics in Fluorescence Spectroscopy, Springer*, New York, (2005).

84. T.H. Tran-Thi, C. Desforge and C.C. Thiec, *J. Phys. Chem.*, 93 (1989)1226.

85. I. J. MacDonald and T. J. Dougherty, *J Porphyrins Phthalocyanines*, 5 (2001) 105.

86. F. Wilkinson and W. P. Helman, *J. Phys. Chem.*, 22 (1993) 113.

87. N. Kuznetsova, E. A. Makarova, S.N. Dashkevich N.S. Gretsova, E.A. Kalmykova, V. M. Negrimovsky, O.L. Kaliya and E.A. Lukyanets, *Russ. J. Gen. Chem.* 70 (2000)140.

88. M. Niedre, M. S. Patterson and B. C. Wilson, *Photochem. Photobiol.*, 75 (2003) 382.

89. M. S. Patterson, S. J. Madsen and R. Wilson, *J. Photochem. Photbiol.* B: 5 (1990) 69.

90. S. Tombe, E. Antunes and T. Nyokong, *New J Chem.* 37 (2013) 679.

91. N. Masilela and T. Nyokong, *J. Photochem. Photobiol. A: Chem.* 223 (2011) 124.

92. X. Huang and M. A. El-Sayed, *Journal of Advanced Research*, 1 (2010) 13.

93. T. Stuchinskaya, M. Moreno, M. J. Cook, D. R. Edwards and D. A. Rusell, *Photochem. Photobiol. Sci.*, 10 (2011) 822.

94. S. Moeno, E. Antunes and T. Nyokong, J. *Photochem. Photobiol. A: Chem.*, 222 (2011) 342.

95. J. Wang, H. Y. Tang, W. L. Yang and J. Y. Chen, *J. Porphyrins Phthalocyanines*, 16 (2012)802.

96. A. Kotiaho, R. Lahtinen, A. Efimov, H. Metsberg, E. Sariola, H. Lehtivuori, N. V. Tkachenko and H. Lemmetyinen, *J. Phys. Chem. C.*, 114 (2010) 162.

97. S. Forteath, E. Antunes, W. Chidawanyika and T. Nyokong, *Polyhedron*, 34, (2012), 114.

98. S. D'Souza, S. Moeno, E. Antunes and T. Nyokong, *New J. Chem.*, 37 (2013) 1950.

99. Y. Nitzan, M. Gutterman, Z. Malik and B. Ehrenberg, *Photochem. Photobiol.*, 55 (1992) 89.

100. Z. Malik, J. Hanania and Y. Nitzan, *J. Photochem. Photobiol. B Biol.*, 5 (1990) 281.

101. Y. Nitzan. R. Dror, H. Ladan, Z. Malik, S. Kimel and V. Gottfried, *Photochem. Photobiol*. 61 (1995) 342.

102. M. R. Hamblin and T Hasan, *Photochem. Photobiol. Sci.*, 5 (2004) 403.

103. C.C. Kibbler, S. Seoton, R. A. Barnes, W. r. Gransden, R. E. Hollimann, E. M. Johnson, J. D. Perry, D. J. Sullivan and J.A. Wilson, *J. Hosp. Infect*. 54 (2003) 18.

104. P. Calzavara-Pinton, M. Rossi, R. Sala and M. Venturini, *Photochem. Phtobiol*. 88 (2012) 512.

105. A. Rai, A. Prabhune and C. C. Perry, *J. Mater. Chem.*, 20 (2010) 6789.

106. V. P. Zharov, K. E. Mercer, E. N. Galitovskaya and S. M. S. Smeltzer, *Biophysical Journal*, 90 (2006)619.

107. E. S. Tuchina, V. V. Tuchin, B. N. Khlebtsov and N. G. Khlebtsov, *Quantum Electronics*, 4 (2011) 354.

108. S. Perni, C. Piccirillo, A. Kafizas, M. Uppal, J. Pratten, M. Wilson and I. P. Parkin, *J. Clust. Sc*i. 21 (2010) 427.

109. I. Maliszewska, A. Lesniewska, J. Olesiak-Banska, K. Matczyszyn and M. Samoc, *J. Nanopart Res.* 16 (2014) 2457.

110. N. Narband, S. Tubby, I. P. Parkin, J. Gil-Tomás1, D. Ready, S. P. Nair and M. Wilson, *Current Nanoscience*, 4 (2008) 409.

111. M. A. Di Palma, M. G. alvarez, A. L. Ochoa, M. E. Milanesio and E. N. Durantini, *Fungul Biol.*, 117 (2013) 744.

112. I. Scalise and E. N. Durantini, Biorg. *Med. Chem.*, 13 (2005) 3037.

113. A. Segalla, C. D. Borsarelli, S. E. Braslavsky, J. D. Spikes, G. Roncucci, D. dei, G. Chiti, G. Jori and E. Reddi, *Photochem. Photobiol. Sci.*, 1 (2002) 641.

114. A. Minnock, D. I. Vernon, J. Schofield, J .Griffiths, J. H. Parish and S. B. Brown, *Antimicrob. Agents Chemther.*, 44 (2000) 522.

115. O. L. Osifeko and T. Nyokong, *Dyes Pigm.*, 11 (2014) 8.

116. A. Minnock, D. Vernon, J. Schofield, J. Griffiths, J. H. Parish and S. B. Brown, *J. Photochem., Photobiol. B: Biology*, 32 (1996) 159.

117. M. Ke, J. M. Eastel, K. L. K. Ngai, Y. Cheung, P. K. S. Chan, M. Hui, D. K. P. Ng and P. Lo, *Eur. J. of Med. Chem.*, 84 (2014) 278.

118. V. Mantareva, v. Kussovski, I. Angelov, E. Borisova, L. Avramov, G. Schnurpfeil and D. Wöhrle, *Bioorg. Med. Chem.*, 15 (2007) 4829.

119. N. Nombona, E. Antunes, W. Chidawanyika, P. Kleyi, Z. Tshentu and T. Nyokong, *J. Photochem. Photobiol. A: Chem.*, 233 (2012) 24.

120. N Masilela, E. Antunes and T. Nyokong, *J. Porphyrins Phthalocyanines*, 17 (2013) 417.

121. D.D. Perrin, W.L.F. Armarego, *Purification of laboratory chemicals. 2nd ed., Pergamon, Oxford*, (1980).

122. P.C. Lee and D. Meisel, *J. Phys. Chem.*, 86 (1982) 3391.

123. J. Weber and D. H. Busch, *Inorg. Chem.,* 4 (1965) 469.

124. M. Ambroz, A. Beeby, A.J. McRobert, M.S.C. Simpson, R.K. Svensen and D. Phillips, *J. Photochem, Photobiol. B: Biol.*, 9 (1991) 87.

125. D. Wöhrle, M. Eskes, K. Shigehara and A. Yamada, *Synthesis*, 2 (1993) 194.

126. A. Yahyazade and V. Azimi, *Appl Chem.*, 49 (2012) 9991.

127. M. Karabork and S. Serin, Synth. *React. Inorg., Met.-Org., Nano-Met. Chem.*, 32 (2002) 1635.

128. U. Kumru, M. A. Ermeydan, F. Dumoulin and V. Ahsen, *J. Porphyrins Phthalocyanines*, 12 (2008) 1090.

129. S. Tuncel, F. Dumoulin, J. Gailer, M. Sooriyaarachchi, D. Atilla, M. Durmuş, D. Bouchu, H. Savoie, R.W. Boyle and V. Ahsen, *Dalton Trans.*, 40 (2011) 4067.

130. N. Sehlotho, M. Durmuş, V. Ahsen and T. Nyokong, *Inorg. Chem. Commun.*, 11 (2008) 479.

131. D. J. Lewis, T. M. Day, J. V. MacPherson and Z. Pikramenou, *Chem. Commun.*, (2006) 1433.

132. T. Hauck in: *A Statistical Model for the Estimation of Gold Nanorod Extinction Coefficients*, Term report, University of Toronto, (2005).

133. H. D. Hill, J. E. Millstone, M. J. Banholzer and C. A. Mirkin, *ACS Nano.*, 3 (2009) 418.

134. C. J. Orendoff and C. J. Murphy, *J. Phys. Chem.* B, 110 (2006) 3990. 135. M. R. K. Ali, B. Snyder and M. A. EI-Sayed, *Langmuir,* 28 (2012) 9807.

136. T. Shen, Z-I Yuan and H-J Xu, *Dyes Pigm.*, 11 (1989) 77.

137. T. Nyokong and E. Antunes, in *The Handbook of Porphyrin Science. Eds. Kadish, K. M. Smith, K. M. Gualard, R. Academic Press: New York World Scientific, Singapore*, Vol. 7 (2010).

138. W. Spiller, H. Kliesch, D. Wöhrle, S. Hackbarth, B. Röder and G. Schnurpfeil, *J. Porphyrins Phthalocyanines*, 2 (1998) 145.

139. N. Kuznetsova, N. Gretsova, E. Kalmkova, E. Makarova, S. Dashkevich, V. Negrimovskii, O. Kaliya and E. Luk'yanets, *Russ. J. Gen. Chem.*, 70 (2000) 133.

140. A. Ogunsipe and T. Nyokong, Photochem. Photobiol. Sci., 4 (2005) 510.

141. W. Spiller, H. Kliesch, D. Worle, S. Hackbarth, B. Roder and G. Schnurpfeil, *J. Porphyrins Phthalocyanines*, 2 (1998) 145.

142. E. A. Dupoy, D. Lazzeri and E. N. Durantini, *Photochem. Photobio. Sci.*, 3 (2004) 992.

143. V. Mantareva, V. Kussovski, I. Angelov and S. Dimitrov, *Science against microbial pathogens: Communicating Current Reasearch and Technological Advances*, (2011) 650.

144. L. Ryskova, V. Buchta, M. Karaskova, J. Rakusan, J. Cerny and Siezak R., *Cent. Eur. J. Biol.*, 8 (2013)168.

145. S. Sapra, D. Sarma and D. Pramana, *J. Phys.*, 65 (2005) 565.

146. Z.-L Yang, H.- Chen, L. Cao, H.-Y Li and M. Wang, *Mater. Scie. Eng. B* 106 (2004) 73.

147. P. K. Jain, I. H. El-Sayed and M. A. El-Sayed, *Nanotoday* 2 (2007)18.

148. F. Mafune, *Chem Phys Let.*, 397 (2004) 133.

149. S. Vukovic, S. Corni and B. Mennucci, *J. Phys. Chem. C.* 113 (2009) 121.

150. R. Schmidt, E. McNellis, W. Freyer, D. Brete, T. Grebel, C. Gahl, K. Reuter and M. Weinelt, *Appl. Phys. A.*, 93 (2008) 267.

151. K. Heiter, M. Zharnikov, M. Grunze and L. S. O. Johansson, *J. Phys. Chem. B*, 105 (2001), 4058.

152. M. Zharnikov, S. Frey, K. Heister and M. Grunze, *Langmuir*, 16 (2000) 2697.

153. D. G. Castner, *Langmuir*, 12 (1996), 5083.

154. D. Nilsson, S. Watcharinyanon, M. Eng, L. Li, E. Moons, L. S. O. Johansson, M. Zharnikov, A. Shaporenko, B. Albinson and J. Martensson, *Langmuir*, 23 (2007) 6170.

155. K. Artyushlcova, B. Kiefer, B. Halevl, A. Knop-Gericke, R. Schlogl and P. Atanassov, *Chem. Commun.*, 49 (2013) 2539.

156. Y. Zhong, M. Jaidann, Y. Zhang, G. Zhang, H. Liu, M. I. Ionescu, R. Li, X. Sun, H. Abou-Rachid and L. Lussier, *J. Phys. Chem. Solids*, 71 (2010) 134.

157. L. Chen, P. Peng, L. Lin, T. C. K. Yang and C. Huang, *Aerol and Air Quality Research*, 14 (2014) 916.

158. Z. Zhou and Y. Huang, *J. Phys. Conf. Ser.*, 188 (2009) 022033.

159. Y. Luo, *Indian J. Chem.*, 46A (2007)1266.

160. D. Dorjnamjin, M. Ariunaa and Y. K. Shim, *Int. J. Mol. Sci.*, 9 (2008) 807.

161. W. Huang, S. Chen, Y. Liu, H. Fu and G. Wu, *Nanotechnology*, 22 (2011) 025602.

162. K. Heister, M. Zharnikov and M.Grunze, *Langmuir*, 17 (2001) 8.

163. Y. W. Yang and L. J. Fan, *Langmuir*, 18 (2002)1157.

164. R. T. Tom and T. Pradeep, Langmuir 21 (2005) 11896.

165. J. A. Lacey and D. Phillips, *Photochem. Photobiol. Sci.* 1 (2002) 378.

166. X.-F. Zhang, X. Li, L. Niu, L. Sun and L. Liu, *J. Fluoresc.,* 19 (2009) 947.

167. Z. Bıyıklıŏglu, M. Durmuş and H. Kantekin, *J. Photochem. Photobiol. A: Chem.* 211 (2010) 32.

168. E. A. Gastilovich, N. V. Korol'kova, V. G. Klimenko and R. N.Nurmukhametov, *Optics Spectr.*, 104 (2008) 491.

169. S. Tombe, W. Chidawanyika, E. Antunes, G. Priniotakis, P. Westbroek and T. Nyokong, *J. Photochem. Photobiol. A: Chem.* 240 (2012) 50.

170. Y. Kaneko, Y. Nishimura, N. Takane, T. Arai, H. Sakuragi, N. Kobayashi, D. Matsunaga, C. Pac and K. Tokumaru, *J. Photochem. Photobiol. A*: 106 (1997) 177.

171. C. D. Geddes and J. R. Lakowicz, *J. fluoresc*, 12 (2002) 122.

172. J. R. Lakowicz, y. Shen, S. D'Auria, J. Malicka, J. Fang, Z. Gryczynski and I Gryczynski, *Ana. Biochem.*, 301 (2002) 261.

173. J. R Lakowicz, *Ana. Biochem.*, 298 (2001) 1.

174. J. R. Lakowicz, *Anal. Biochem.*, 337 (2005) 171.

175. M. Swierczewska, S. Lee and X. Chen, *Phys. Chem. Chem. Phys.,* 13 (2011) 9929.

176. T. Ming, L. Zhao, H. Chen, K. C. Woo, J. Wang and H. Lin, *Nanolett.*, 11 (2011) 2296.

177. K.E. Achuyuthan, A.M. Achyuthan, S.M. Brozik, S.M. Dirk, T.R. Lujan. J.M. Romero and J.C. Harper, *Analyt. Sci.*, 28 (2012) 433.

178. E. Dulkeith, A.C. Mortean, T. Niedereicholz, T. A. Klar, J. Feldman, S.A. Levi, F. C. J. M. van Veggel, D. N. Reinhouldt, M. Möller and D. I. Gittis, *Phys., Rev. Lett.*, 89 (2002) 203002-1.

179. Y. Fu, J. Zhang and J. R. Lakowicz, *J. Am. Chem. Soc.,* 132 (2010) 5540.

180. M.G. Debacker, O. Deleplanque, B. Van Vlierberge and F. X. Sauvage, *Laser Chem.* 8 (1988) 1.

181. G. van Maltzahn, J. Park, A. Agrawal, N. K. Bandaru, S. K. Das, M. J. Sailor and S.N. Bhatia, *Cancer. Res.,* 69 (2009) 3892.

182. M. A. Di Palma, M. G. Alvarez, A. L. Ochoa, M. E. Milanesio and E. N. Durantini, *Fungal Biol.*, 117 (2013) 744.

183. P. Dziegiel, *Pol. J. Pathol.*, 55 (2004) 3.

184. M. J. Stillman, *Coord. Chem. Rev.*, 144 (1995) 461.

185. T. T. Ng and M. J. Stillman, *J. Am. Chem. Soc.*, 128 (2006) 12473.

186. J. Zaia, D. Fabris, D. Wei, R. L. Karpel and C. Fenselau, *Prot. Sci.*, 7 (1998) 2398.

187. M.J. Stillman, D. Thomas, C. Trevithick, X. Guo, M. Siu, *Inorg. Biochem.*, 79 (2000) 11.

188. M. Sato and M. Kondoh, Tohoku *J. Exp. Med.* 196 (2002) 9.

189. J. Chen, Z. Huang, I. Watt, R. Kille and M. J. Stillman, *Can. J. Chem.*, 85 (2007) 898.

190. Y. Rio, M. S. Rodriguez-Morgade and T. Torres, *Org. Biomol. Chem.*, 6 (2008) 1877.

191. J. C. Kendrew, G. Bodo, H. M. Dintzis, R. G. Parrish, H. Wyckoff and D. C. Phillips, *Nature*, 181 (1958) 662.

192. S. Sil and A. S. Chakraborti, *Ind. J. Biochem. Biophys.*, 33 (1996) 285.

193. J. Bhattacharyya, M. Bhattacharyya, A. S. Chakraborti and U. Chaudhuri, *Biochem. Pharmacol.*, 47 (1994) 2049.

194. P. Ascenzi, M. Colasanti, M. Fasano and A. Bertollini, Biochem., *Mol. Biol. Int.*, 47 (1999) 991.

195. G. I. Stables and D. V. Ash, *Cancer. Treat. Rev.*, 21 (1995) 311.

196. P. Dziegiel, *Pol. J. Pathol.* 55 (2004) 3.

197. K. E. R. Duncan and M. J. Stillman, *Ferederation of Biochemical Societies*, 274 (2007) 2253.

198. M. T. Tiedemann, T. B. J. Pinter and M. J. Stillman, *Metallomics*, 4 (2012) 751.

199. C. S. Ho, C.W.K. Lam, M. H. M. Chan, R. C. K. Cheung, L. K. Law, L. C. W. Lit, K. F. Ng, M. W. M. Seun and H. L. Tai, *Clin. Biochem. Rev.*, 23 (2003) 3.

200. C. Dass, *Principles and Practice of Biological Mass Spectrometry,* Wiley Interscience: New York, (2001).

201. A. El-Aneed, A. Cohen and J. Banoub, *Applied Spectroscopy Reviews*, 44 (2009) 210.

202. J. Chen, Z. Huang, I. Watt, P. Kille and M. J.Stillman, *Can. J. Chem.*, 85 (2007) 898.

203. D. E. K. Sutherland and M. J. Stillman, *Biochem. Biophys. Res.*, 371 (2008) 840.

204. P. M. Gehrig, C. You, R. Dallinger, C. Gruber, M. Brouwer, J. H. R. Kagi, P. E. Hunziker, *Protein. Sci.*, 9 (2000) 2395.